Additive Manufacturing of Bovine Serum Albumin-based and Pluronic F127 Hydrogels and Bioplastics

Patrick T Smith

A dissertation

submitted in partial fulfillment of the

requirements for the degree of

Doctor of Philosophy

University of Washington

2021

Reading Committee:

Alshakim Nelson, Chair

Forrest Michael

Matthew Golder

Program Authorized to Offer Degree:

Chemistry

University of Washington

Abstract

Additive Manufacturing of Bovine Serum Albumin-based and Pluronic F127 Hydrogels and Bioplastics

Patrick Smith

Chair of the Supervisory Committee:
Professor Alshakim Nelson
Department of Chemistry

Additive manufacturing (AM) has claimed its place as one of the key elements in the fourth industrial revolution, the automation and digitization of industry. By enabling one to rapidly fabricate and test any 3D structure over a range of length scales with limited expertise, AM is challenging the status quo of how things are invented and manufactured. However, the severe lack of materials that are compatible with AM limits its ability to disrupt the traditional manufacturing industry. To push the boundaries and drive forward innovation in manufacturing, new materials must be designed specifically for AM.

This thesis explores the investigation of the printability of a library of synthetic inks for direct-ink write 3D printing and the development of globular protein-based resins for stereolithography. The inks for DIW are based on Pluronic F127, a triblock copolymer that forms temperature responsive,

shear thinning hydrogels. Several rheological parameters that define a successful ink for DIW 3D printing are identified. Additionally, the development of a protein-based resin is reported, wherein the globular protein, bovine serum albumin, is modified and formulated into a photocurable resin for stereolithography. Several post-print treatments such as 120 °C thermal denaturation or tannic acid incubation were employed to tune the mechanical properties of the printed structures. This work demonstrates a set of resins and post-print treatments that can be used for a range of applications from biomedical devices to bioplastics.

TABLE OF CONTENTS

LIST OF FIGURES

LIST OF TABLES

ACKNOWLEDGEMENTS

I am incredibly grateful for all the friends, family, and mentors that have supported me throughout my education. I could not have done it without you.

Specifically, I would like to thank my graduate advisor, Dr. Alshakim Nelson, for his exemplary leadership and support throughout my time at UW. All of the time and opportunities that you gave me has helped me grow as a scientist. When the time comes, I hope to be as exceptional of a role model to others as you have been to me.

I would also like to thank the members of the Nelson lab. Dylan, Trevor, Amrita, Ryan, and Abhi, I appreciate all your guidance as I got started in the Nelson lab. Fang and Eva, your abundant knowledge and mentorship was incredibly helpful over the past few years. Cem, Gokce, and Jenn, I will greatly miss brainstorming new ideas in the lab and going out for lunch on the Ave. Chris, it was great living together and figuring out our way through grad school together.

I would like to thank my doctoral committee members Dr. Forrest Michael, Dr. Matt Golder, and Dr. Lucas Meza for challenging me to continue to learn more.

I would like to thank my family for their unwavering support. Thank you, mom and dad, for all of the sacrifices you have made to allow me to pursue my passions. Thank you to my brothers, Chris, Alex, and Gregg, for always being there for me. I would not be where I am today without you. Thank you to Clarissa and her family for all your love and support.

Finally, I would like to thank God for His countless blessings.

DEDICATION

To my parents Michael Smith and Cynthia Smith

To my Ate Weng

The beautiful thing about learning is that no one can take it away from you

- B.B. King

Chapter 1. INTRODUCTION

1.1 INTRODUCTION TO ADDITIVE MANUFACTURING OF HYDROGELS

Additive manufacturing (AM) has claimed its place as one of the key elements in the fourth industrial revolution, the automation and digitization of industry. By enabling one to rapidly fabricate and test any 3D structure over a range of length scales, AM is challenging the status quo of how things are invented and manufactured. Traditional manufacturing of parts typically requires several steps, each using different processes such as molding, turning, or milling. However, in AM the process is simplified and goes directly from a computer aided design (CAD) model to a fabricated part using a single device, cutting the iterative prototyping process to a span of days compared to months while also significantly cutting the costs. While this will certainly disrupt the way traditional parts are manufactured today, recent material advancements have expanded the scope of AM into new fields such as medicine, tissue engineering, and cell culture. The advent of 3D printed hydrogels has opened the door for the development of new bio-interfacing applications. To continue to push the boundaries and drive forward innovation, new materials with a wide range of mechanical and functional properties must be designed specifically for AM.

Hydrogels are crosslinked, hydrophilic polymer networks that may absorb large amounts of water or aqueous solutions.[1] The high water content in hydrogels enable the ability to mimic native extracellular matrix (ECM) and transport hydrophilic agents, making them ideal for bio-interfacing applications. Many researchers have employed AM techniques to pattern hydrogels into complex structures for such applications. Two common AM techniques that are compatible with hydrogels are direct-ink-write (DIW) 3D printing and vat photopolymerization (VP).

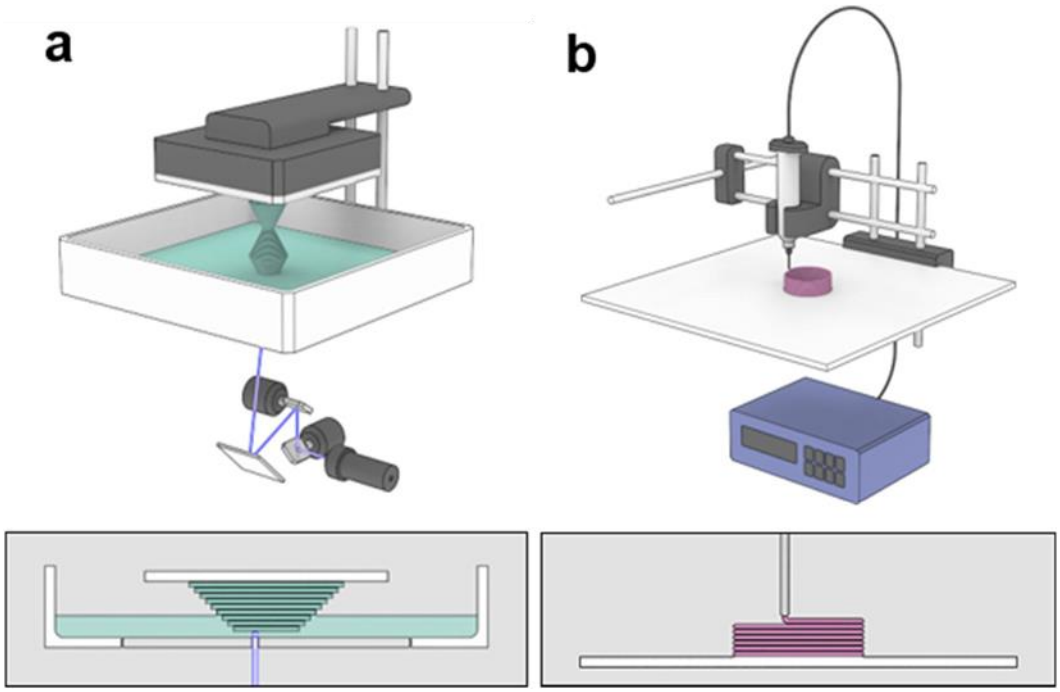

Figure 1. 1 Schematic of a) SLA and b) DIW printing processes.

In DIW 3D printing, hydrogel materials are extruded through a nozzle and deposited as filaments layer-by-layer into a 3D structure. There are two strategies to pattern hydrogels via DIW 3D printing. In the first method, low viscosity inks are extruded into a support bath or build plate followed by a curing step during or immediately after each layer.[2] In the second method, shear-thinning hydrogels, like Pluronic F127, are used because they can flow under applied load and rapidly re-form a self-supporting gel upon deposition. Pluronic F127 is a triblock copolymer consisting of poly(ethylene oxide)-*b*-poly(propylene oxide)-*b*-poly(ethylene oxide) (PEO-*b*-PPO-*b*-PEO). At the critical micelle concentration (CMC), the F127 chains aggregate into micelles with an inner core of hydrophobic PPO units and an outer shell of hydrophilic PEO units. At concentrations well above the CMC (~20 wt%), the micelles pack together forming a 3D hydrogel network. These F127 hydrogels have a temperature responsive sol-gel transition, wherein at low temperature, the polymer chains are all individually solvated as unimers forming a low viscosity

solution. Upon increasing to room temperature, the unimers form micelles and the micelles pack to form a free-standing gel. The reversible sol-gel transition enables easy incorporation of additives such as colloidal particles or living cells into solution at low temperatures and upon increasing to room temperature, the gel network recovers. The gel network is held together by reversible, physical bonds that reversibly break down and re-form in response to shear force, making F127 an excellent polymer for DIW 3D printing. To "turn off" the shear thinning response, the chain ends may be functionalized with polymerizable groups, like acrylates or methacrylates, which are polymerized to form covalent crosslinks after 3D printing.

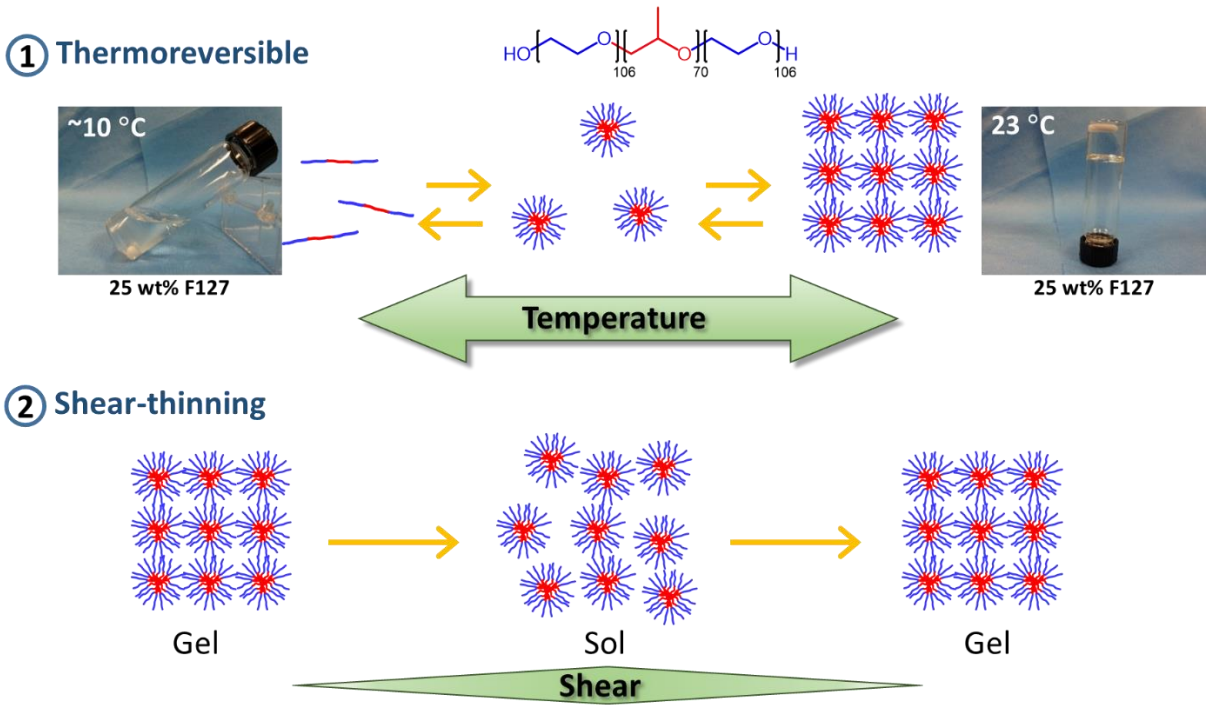

Figure 1. 2 Schematic of temperature and shear responses of Pluronic F127

A second AM technique used to fabricate hydrogels is vat photopolymerization which uses patterned light to photopolymerize a liquid resin. This technique typically has higher resolution than DIW 3D printing, enabling the fabrication of much more complex structures. UV or visible

light is used to activate a catalyst or reactive species to initiate curing using reactions such as radical polymerization of acrylates and methacrylates, cationic ring opening polymerization of epoxides, thiol-ene click chemistry, or reversible Diels-Alder reactions. Two commonly used VP techniques are stereolithography (SLA) and digital light processing (DLP). In SLA printing, a build plate is submerged into a resin tank filled with a photopolymerizable liquid resin. A single wavelength laser is then rastered through an optical window to selectively polymerize the liquid resin to the build plate. The build plate moves up a previously defined step size, liquid resin flows to cover the optical window, and the next layer is irradiated and covalently bound to the previous layer. Two key parameters for successful SLA resins are low viscosity and fast cure rate upon irradiation. The viscosity should be minimized to allow the resin to flow between layers, and each layer must cure rapidly, as irradiation times longer than a few seconds can lead to exceedingly long print times. Similarly, DLP uses light to initiate photopolymerization of a liquid resin. However, in DLP, an image is projected into the resin, polymerizing the entire layer at the same time. While this enables faster print times, SLA typically has higher resolution.

Many synthetic polymers have been used to create hydrogels for DIW and VP, as starting from synthetic polymers offers great tunability and batch to batch consistency. While there are many applications for 3D printed synthetic hydrogels, it is also desirable to develop methods to print with natural polymers. Natural polymers, such as proteins and carbohydrates, offer several advantages over synthetic polymers such as biodegradability, native sites for cell interactions, and sustainable sourcing.

1.2 INTRODUCTION TO NATURAL POLYMERS FOR ADDITIVE MANUFACTURING

Nature's biopolymers, including polysaccharides, proteins, and DNA/RNA, are perfectly integrated into closed-loop systems wherein they can be degraded, recycled, and reused in a manner that is unmatched by synthetic polymers. Bio-sourced materials that can replace existing petroleum-based materials are an integral component of sustainability.[3] Moreover, renewable materials with greater complexity and functionality that can supplant petroleum-derived materials will be required to meet the demands for the full spectrum of applications from aerospace to medicine. Protein-based materials[4–8] utilize natural and unnatural amino acid repeat units to create well-defined macromolecules that can be precisely folded and assembled. Biologically derived proteins, engineered proteins, and polymer-protein conjugates have been developed to create materials that emulate biological and nonbiological function, as well as other physical characteristics (i.e., mechanical properties).[9–15] While there are significant efforts to develop protein-based materials for commercial use, their application is restricted by generally poor processability and limitations in mechanical performance. Protein-based materials can be processed via solvent casting, melt extrusion, and injection molding,[16–19] but the fabrication of objects with complex 3D form factors is limited. Thus, in order to create the next generation of sustainable materials, there is a need for manufacturing of proteins and other natural polymers into highly resolved, complex structures with mechanical properties comparable or superior to those of petroleum-based polymers.

Additive manufacturing (AM) of natural polymers has tremendous potential for the future production of parts and supplies.[20,21] Many groups have investigated DIW 3D printing of natural polymers, such as alginate or gelatin methacrylate. However, DIW 3D printing of these materials typically results in poorly resolved structures. Vat photopolymerization[22,23] techniques such as

SLA and DLP have emerged as promising techniques that can offer high quality parts at increasingly faster rates of production.[24] While a growing list of elastomers, plastics, and composites have been reported, most of these resins are based on petrochemical feedstocks that can only be regenerated on geologic timescales. There are relatively few examples of resins that are bio-sourced and bio-degradable, [25–29] yet these features are critical for creating a sustainable future materials economy that includes AM for production.[30] Thus, the lifecycle of parts[31–34] made by AM will need to involve recycling of the printed object back into feedstock resin, or its degradation into non-toxic products.

Generally, designing new oligomers and polymers for vat photopolymerization is challenged[35–37] by the increase in viscosity of the resin with polymer concentration and molecular weight as predicted by Mark-Houwink equation.[38] An alternative design strategy is to employ synthetic polymers architectures such as cyclic, branched, dendritic, or cross-linked unimolecular particles architecture that have a lower intrinsic viscosity relative to a linear polymer of comparable molecular weight.[39–42] Interestingly, the photocurable protein derivatives that have been reported (gelatin and silk fibroin) are structural proteins that are designed to form fibrous assemblies. This formation is counterproductive, as it increases the viscosity of the resin, which limits its processability via vat photopolymerization. In chapters 3 and 4 of this thesis, a globular protein, bovine serum albumin (BSA), is formulated into low viscosity photopolymerizable resins for SLA. The development of a series of inks and resins for DIW and SLA is discussed in the following chapters. Chapter 2 investigates the printability of synthetic polymer inks for DIW 3D printing of hydrogels. Chapter 3 introduces an easily processible protein-based resin for SLA that is biocompatible and biodegradable. Chapter 4 covers additional formulations and post-processing

conditions of our protein-based resin that enable us to tune the mechanical properties over a wide range, enabling future applications.

1.3 REFERENCES

1. Hoffman, A. S. Hydrogels for biomedical applications. *Adv. Drug Deliv. Rev.* **64**, 18–23 (2012).
2. He, Y. *et al.* Research on the printability of hydrogels in 3D bioprinting. *Sci. Rep.* **6**, 29977 (2016).
3. O'dea, R. M., Willie, J. A. & Epps, T. H. 100th Anniversary of Macromolecular Science Viewpoint: Polymers from Lignocellulosic Biomass. Current Challenges and Future Opportunities. *ACS Macro Lett.* **9**, 476–493 (2020).
4. Mekonnen, T., Mussone, P. & Bressler, D. Valorization of rendering industry wastes and co-products for industrial chemicals, materials and energy: Review. *Crit. Rev. Biotechnol.* **36**, 120–131 (2016).
5. Cuq, B., Gontard, N. & Guilbert, S. Proteins as agricultural polymers for packaging production. *Cereal Chem.* **75**, 1–9 (1998).
6. Johnson, J. A., Lu, Y. Y., Van Deventer, J. A. & Tirrell, D. A. Residue-specific incorporation of non-canonical amino acids into proteins: Recent developments and applications. *Curr. Opin. Chem. Biol.* **14**, 774–780 (2010).
7. Li, Y., Xue, B. & Cao, Y. 100th Anniversary of Macromolecular Science Viewpoint: Synthetic Protein Hydrogels. *ACS Macro Lett.* **9**, 512–524 (2020).
8. Cummings, C. S. & Obermeyer, A. C. Phase Separation Behavior of Supercharged Proteins and Polyelectrolytes. *Biochemistry* **57**, 314–323 (2018).
9. Chan, W. Y., Bochenski, T., Schmidt, J. E. & Olsen, B. D. Peptide Domains as Reinforcement in Protein-Based Elastomers. *ACS Sustain. Chem. Eng.* **5**, 8568–8578 (2017).
10. Thomas, C. S., Glassman, M. J. & Olsen, B. D. Solid-state nanostructured materials from self-assembly of a globular protein-polymer diblock copolymer. *ACS Nano* **5**, 5697–5707 (2011).
11. Wong Po Foo, C., Lee, J. S., Mulyasasmita, W., Parisi-Amon, A. & Heilshorn, S. Two-component protein-engineered physical hydrogels for cell encapsulation. *Proc. Natl. Acad. Sci.* **106**, 22067–22072 (2009).
12. Deming, T. J. Facile synthesis of block copolypeptides of defined architecture. *Nature* **390**, 386–389 (1997).
13. Duarte Campos, D. F. *et al.* Bioprinting Cell- and Spheroid-Laden Protein-Engineered Hydrogels as Tissue-on-Chip Platforms. *Front. Bioeng. Biotechnol.* **8**, (2020).
14. Camacho, P. *et al.* 3D printing with peptide-polymer conjugates for single-step fabrication

of spatially functionalized scaffolds. *Biomater. Sci.* **7**, 4237–4247 (2019).

15. Camacho, P., Busari, H., Seims, K., Tolbert, J. & Chow, L. *3D Bioprinting in Medicine*. (Springer, 2019).

16. Hernandez-Izquierdo, V. M. & Krochta, J. M. Thermoplastic processing of proteins for film formation - A review. *J. Food Sci.* **73**, R30–R39 (2008).

17. Bier, J. M., Verbeek, C. J. R. & Lay, M. C. Thermal transitions and structural relaxations in protein-based thermoplastics. *Macromol. Mater. Eng.* **299**, 524–539 (2014).

18. Sothornvit, R., Olsen, C. W., McHugh, T. H. & Krochta, J. M. Tensile properties of compression-molded whey protein sheets: Determination of molding condition and glycerol-content effects and comparison with solution-cast films. *J. Food Eng.* **78**, 855–860 (2007).

19. Galietta, G., Di Gioia, L., Guilbert, S. & Cuq, B. Mechanical and Thermomechanical Properties of Films Based on Whey Proteins as Affected by Plasticizer and Crosslinking Agents. *J. Dairy Sci.* **81**, 3123–3130 (1998).

20. Narupai, B. & Nelson, A. 100th Anniversary of Macromolecular Science Viewpoint: Macromolecular Materials for Additive Manufacturing. *ACS Macro Lett.* **9**, 627–638 (2020).

21. Maeng, J. *et al.* Liquid crystal elastomers as substrates for 3D, robust, implantable electronics. *J. Mater. Chem. B* **8**, 6286–6295 (2020).

22. Bagheri, A. & Jin, J. Photopolymerization in 3D Printing. *ACS Appl. Polym. Mater.* **1**, 593–611 (2019).

23. Appuhamillage, G. A. *et al.* 110th Anniversary: Vat Photopolymerization-Based Additive Manufacturing: Current Trends and Future Directions in Materials Design. *Ind. Eng. Chem. Res.* **58**, 15109–15118 (2019).

24. Zuev, D. M., Nguyen, A. K., Putlyaev, V. I. & Narayan, R. J. 3D printing and bioprinting using multiphoton lithography. *Bioprinting* **20**, e00090 (2020).

25. Poldervaart, M. T. *et al.* 3D bioprinting of methacrylated hyaluronic acid (MeHA) hydrogel with intrinsic osteogenicity. *PLoS One* **12**, 1–15 (2017).

26. Lim, K. S. *et al.* New Visible-Light Photoinitiating System for Improved Print Fidelity in Gelatin-Based Bioinks. *ACS Biomater. Sci. Eng.* **2**, 1752–1762 (2016).

27. Ding, R., Du, Y., Goncalves, R. B., Francis, L. F. & Reineke, T. M. Sustainable near UV-curable acrylates based on natural phenolics for stereolithography 3D printing. *Polym. Chem.* **10**, 1067–1077 (2019).

28. Kim, S. H. *et al.* Precisely printable and biocompatible silk fibroin bioink for digital light processing 3D printing. *Nat. Commun.* **9**, 1620 (2018).

29. Lim, K. S. *et al.* Bio-resin for high resolution lithography-based biofabrication of complex cell-laden constructs. *Biofabrication* **10**, 034101 (2018).

30. Sanchez-Rexach, E., Johnston, T. G., Jehanno, C., Sardon, H. & Nelson, A. Sustainable Materials and Chemical Processes for Additive Manufacturing. *Chem. Mater.* **32**, 7105–7119 (2020).

31. Geyer, R., Jambeck, J. R. & Law, K. L. Production, use, and fate of all plastics ever made. *Sci. Adv.* **3**, 25–29 (2017).

32. Lange, J. P. Sustainable development: Efficiency and recycling in chemicals manufacturing. *Green Chem.* **4**, 546–550 (2002).

33. Schneiderman, D. K. & Hillmyer, M. A. 50th Anniversary Perspective: There Is a Great Future in Sustainable Polymers. *Macromolecules* **50**, 3733–3749 (2017).

34. Fortman, D. J. *et al.* Approaches to Sustainable and Continually Recyclable Cross-Linked Polymers. *ACS Sustain. Chem. Eng.* **6**, 11145–11159 (2018).

35. Hinczewski, C., Corbel, S. & Chartier, T. Ceramic suspensions suitable for stereolithography. *J. Eur. Ceram. Soc.* **18**, 583–590 (1998).

36. Sutton, J. T., Rajan, K., Harper, D. P. & Chmely, S. C. Lignin-Containing Photoactive Resins for 3D Printing by Stereolithography. *ACS Appl. Mater. Interfaces* **10**, 36456–36463 (2018).

37. Luo, Y., Le Fer, G., Dean, D. & Becker, M. L. 3D Printing of Poly(propylene fumarate) Oligomers: Evaluation of Resin Viscosity, Printing Characteristics and Mechanical Properties. *Biomacromolecules* **20**, 1699–1708 (2019).

38. Hiemenz, P. C. & Lodge, T. *Polymer Chemistry*. (CRC Press, 2007).

39. Seiler, M. Hyperbranched polymers: Phase behavior and new applications in the field of chemical engineering. *Fluid Phase Equilib.* **241**, 155–174 (2006).

40. Voit, B. I. & Lederer, A. Hyperbranched and highly branched polymer architectures-synthetic strategies and major characterization aspects. *Chem. Rev.* **109**, 5924–5973 (2009).

41. Le Fer, G., Luo, Y. & Becker, M. L. Poly(propylene fumarate) stars, using architecture to reduce the viscosity of 3D printable resins. *Polym. Chem.* **10**, 4655–4664 (2019).

42. Mondschein, R. J., Kanitkar, A., Williams, C. B., Verbridge, S. S. & Long, T. E. Polymer structure-property requirements for stereolithographic 3D printing of soft tissue engineering scaffolds. *Biomaterials* **140**, 170–188 (2017).

Chapter 2. CHEMICAL MODIFICATION AND PRINTABILITY OF SHEAR-THINNING HYDROGEL INKS FOR DIRECT-WRITE 3D PRINTING

2.1 ABSTRACT

Shear-thinning hydrogels are often employed in direct-write 3D printing, however, the viscoelastic behaviors that define a printable hydrogel have not been fully established. Herein, we demonstrate a library of hydrogel inks based on the incorporation of water-soluble reactive meth(acrylate) monomers into F127-dimethacrylate hydrogels. This strategy afforded printed hydrogels with a broad range of chemical functionalities and mechanical properties. A systematic investigation was also performed to correlate the printability and mechanical properties to the viscoelastic properties of the hydrogel ink formulations. The materials with a high dynamic yield stress afforded extruded filaments that correlated well with the inner diameter of the printing nozzle. The static yield stress of the material was correlated to the extrusion pressure and print speed required for optimal printing. Thus, this study provides a guide for the future development of hydrogel inks for direct-write 3D printing along with a new set of functional hydrogel inks.

2.2 INTRODUCTION

Additive manufacturing (also referred to as 3D printing) represents a versatile technology which enables the customized fabrication of three-dimensional objects for applications ranging from soft robotics[1,2] to tissue engineering.[3-5] Direct-write 3D printing is a type of additive manufacturing wherein a nozzle is rastered across a surface in a pattern-wise manner while an ink is deposited. An advantageous feature of this method of 3D printing is the easy access to the fabrication of functional materials, as well as multi-material printing.[6] A broad spectrum of inks has been

developed that include polymeric materials,[7-9] polyelectrolyte complexes,[10,11] and colloids.[12] As a result, direct-write 3D printing has become an attractive tool in the additive manufacturing of 3D objects.[13,14]

Polymer hydrogels have gained prominence as candidates for 3D printing and bioprinting of tissue constructs[15,16] and implants.[17,18] These soft materials are largely comprised of water, and serve as natural mimics of extracellular matrices. Synthetic hydrogels have tunable chemical features, and are also suitable for flexible electronics,[19,20] supercapacitors,[21] controlled drug release[22] and sensor[23,24] applications. Direct-write 3D printing is a facile method to pattern functional hydrogels to afford unique geometries and functionalities that are difficult or impossible to produce by conventional methods.[25] There are two strategies to print hydrogels via direct-write printing. The first strategy utilizes a low viscosity ink that is extruded from a nozzle, which then undergoes gelation induced by a chemical, photo-chemical,[26,27]or noncovalent process.[28] For example, calcium alginate gels have been printed in this manner using divalent calcium ions to cross-link the polyanionic polysaccharide.[29] Alternatively, a shear-thinning hydrogel ink—which exhibits a viscoelastic response to applied pressure—can be extruded from a nozzle to directly deposit the gel into a 3D object. Our group has focused[30] on this latter approach to develop synthetic hydrogels for direct-write 3D printing. Despite the importance of understanding the viscoelastic behavior of hydrogel inks for direct-write 3D printing, a clear quantitative understanding of the viscoelastic requirements has yet to emerge. The palette of new hydrogel ink compositions for direct-write 3D printing can be more rapidly improved with a fundamental understanding of the viscoelastic parameters necessary to fabricate 3D objects consistently and accurately. For example, the optimization of the printed resolution should be dictated by inks that minimize die-swelling behavior and affords extruded filament diameters commensurate with the

inner diameter (I.D.) of the nozzle. Additionally, the ink should demonstrate rapid shear recovery and robust mechanical properties post-extrusion to maintain the printed form over time and allow easy manipulation and handling.

Pluronic F127 is a commercially available triblock copolymer with the composition, poly(ethylene oxide)-*block*-poly(propylene oxide)-*block*-poly(ethylene oxide) (PEO-*b*-PPO-*b*-PEO), which has been used as a biocompatible polymer for wound dressings and drug delivery.[31-33] When dissolved in aqueous media, F127 forms dual stimuli-responsive hydrogels (at 20-40 wt % concentrations in water) that responds to temperature and pressure (shear-thinning) stimuli.[30,34] This polymer hydrogel is suitable for direct-write 3D printing, and is most commonly utilized as a fugitive ink, wherein the hydrogel is printed as part of a 3D sacrificial template that is removed afterward.[6,33] Zenobi-Wong and co-workers have also demonstrated that F127 can be functionalized at the chain-ends with methacrylate groups (F127-DMA) to afford a cross-linkable hydrogel that can be photo-polymerized after 3D printing.[26] While F127 and F127-DMA are useful inks for direct-write 3D printing, the field presently lacks approaches to modify the hydrogel ink in order to afford printed structures with greater control over chemical functionality and mechanical properties of the printed hydrogel.

Herein, we demonstrate a library of hydrogel inks for direct-write 3D printing formulated with F127-DMA and water-soluble reactive monomer additives. Furthermore, we utilize rheometry to correlate the viscoelastic properties of these hydrogel inks to its printability. The addition of any number of such monomers can add new functionality to the native F127-DMA hydrogels, to increase its versatility as a biomaterial, pH/ temperature responsive smart material, or handle for peptide and fluorophore conjugation.[35,36] Previous reports for direct-write 3D printing hydrogel demonstrated that the quality of the printed object can be optimized by tuning

parameters such as extrusion pressure and printing speed.[37] Mathematical models that predict filament resolution for shear-thinning hydrogels have also been developed.[38] M'Barki et al. recently investigated shear-thinning ceramic inks and demonstrated that the yield stress is a critical parameter in defining a suitable ink for extrusion-based printing.[39] There are two different types of yield stresses: the static yield stress (σ_{stat}) is the stress required to make a fluid (or gel) flow from rest, and the dynamic yield stress (σ_{dyn}) is the minimum stress required for a fluid (or gel) in motion to sustain its flow. Thus, in order for a shear-thinning hydrogel to be employed as a 3D printable ink, the material must not only overcome the static yield stress to initiate extrusion from a nozzle, but also exceed the dynamic yield stress to sustain the extrusion of a filament from that nozzle to form a continuous filament with minimum deformation. The dynamic yield stress also determines the extent to which a hydrogel filament continues to flow after it has exited the nozzle. The minimization of this flow will lead to filament diameters that are commensurate with the nozzle diameter. In this report, we will correlate the rheometrical analysis of these hydrogel inks to the printing parameters required for direct-write 3D printing. As a demonstration of the versatility that these inks provide,[40-41] we also demonstrate the changes to the mechanical properties of the printed hydrogels with the inclusion of these additives.

2.3 Results and Discussion

2.3.1 *Flow behavior and rheological characterization of the polymer compositions*

Figure 2.1 shows the general scheme to formulate and direct-write 3D print with the hydrogel inks. The reversible temperature response of the hydrogel allows facile incorporation of additives to the solution-phase of the aqueous mixture at temperatures below its gelation temperature (T_{gel}) where the aqueous mixtures of F127-DMA behave as a solution. The shear-

thinning property of the inks enable their extrusion through the nozzle with applied pressure. Irradiation with 365 nm light initiates photo-polymerization of the reactive monomers to cross-link the hydrogel, and effectively turn off the shear-thinning response. We chose water-soluble, photo-polymerizable monomers as additives, such as acrylic acid (AA), 2-hydroxyethyl acrylate (HEA), 2-(dimethylamino)ethyl methacrylate (DMAEMA) and poly(ethylene glycol) diacrylate (PEG-DA), which can undergo *in situ* photo-copolymerization of the methacrylate end-groups of F127-DMA with the reactive monomer additives. The additives were included as either 4 or 10 wt% of the total hydrogel composition.

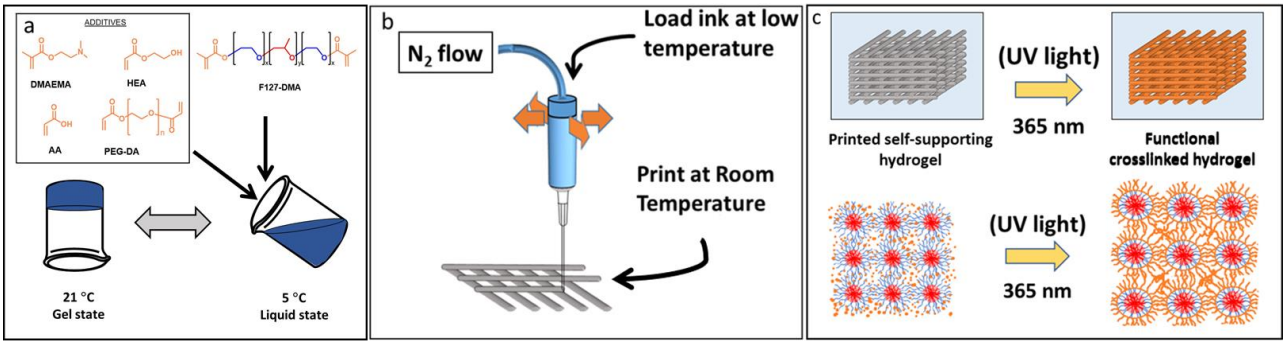

Figure 2. 1 Overview of extrusion printing process.
(a) Additives are incorporated into F127-DMA in its sol state, and then transferred into a syringe where it becomes a gel at 21 °C. (b) Nitrogen gas is used to pressurize the syringe to dispense the shear-thinning hydrogel ink from a nozzle at 21 °C. (c) The printed structure is irradiated with 365 nm light to induce *in-situ* co-polymerization of F127-DMA and the additives.

A temperature ramp experiment was performed for each of the samples to characterize the thermo-responsive behavior of the materials (Supporting Information). The T_{gel} is represented by the cross-over point between the storage (G') and loss moduli (G"). All the formulations exhibited a temperature-dependent sol-gel transition, although the value for the T_{gel} changed with the quantity and the composition of the additive (Table 2.1). The values for the T_{gel} ranged from 7.5 to 17.5 °C.

Table 2. 1 Rheological properties and filament diameters of each hydrogel ink
Printed at 20 psi and 5 mm/s at 21 ° C, σ_{dyn} is the dynamic yield stress of the material and ε is the error in printability from the nozzle size.

POLYMER 1 (wt %)	ADDITIVE (wt%)	FILAMENT DIAMETER (μm)	σ_{DYN} (Pa)	ε (%)	T_{Gel} (°C)
F127DMA (30)	-	430 ± 15	322.70	4.87	13.9
F127DMA (25)	-	1176 ± 20	224.64	186.83	16.2
F127DMA (25)	PEG-DA(10)	410 ± 10	417.02	2.44	15.2
F127DMA (25)	DMAEMA (10)	415 ± 10	365.90	3.65	7.5
F127DMA (25)	DMAEMA(4)	450 ± 10	313.66	9.75	14.2
F127DMA (25)	AA(10)	735 ± 15	260.54	79.26	12.2
F127DMA (25)	AA(4)	909 ± 5	236.74	121.70	14.2
F127DMA (25)	HEA(10)	1150 ± 30	251.04	180.49	15.9
F127DMA (25)	PEG-DA(4)	N/A[a]	179.39	N/A	14.6
F127DMA (25)	HEA(4)	N/A[a]	8.187	N/A	15.1

[a] A filament could not be extruded with this formulation at the given temperature.

Rheological experiments such as viscosity versus shear rate and cyclic shear strain (Supporting Information) were used to probe the differences in the viscoelastic responses of the inks under conditions representative of 3D printing. For extrusion-based 3D printing of hydrogel inks, shear-thinning materials are often favored since they undergo a substantial reduction in viscosity under shear stress. All formulations showed similar shear-thinning behavior, wherein the viscosity decreased by almost three orders of magnitude as the shear rates increased from 0.01 s^{-1} to 100 s^{-1} (Supporting information). This feature is important to ensure the smooth flow of hydrogels from a nozzle during direct-write 3D printing. In the cyclic shear strain experiment, periods of high strain emulated the shear forces the inks experienced as they were extruded through a nozzle and the subsequent period of low strain represented the ink after it exited the nozzle. Alternating periods of low amplitude strain of ~ 1% and high amplitude strain of ~ 100% were applied on each sample for 5 mins and 3 mins, respectively for five cycles (Figure 2.2). All the samples showed a sharp decrease in moduli under high strain and recovered within 4 s upon relief

from that strain. The hydrogel displayed minimal hysteresis between strain cycles, which suggests that the hydrogel inks can rapidly reform the physical cross-links between the polymer chains that provide the mechanical stability of the hydrogel. Even after several cycles, the yielding and recovery behavior of the materials did not appreciably change, which suggested that the hydrogel inks were suitable for direct-write printing processes wherein the flow of the ink is turned 'on' and 'off'.

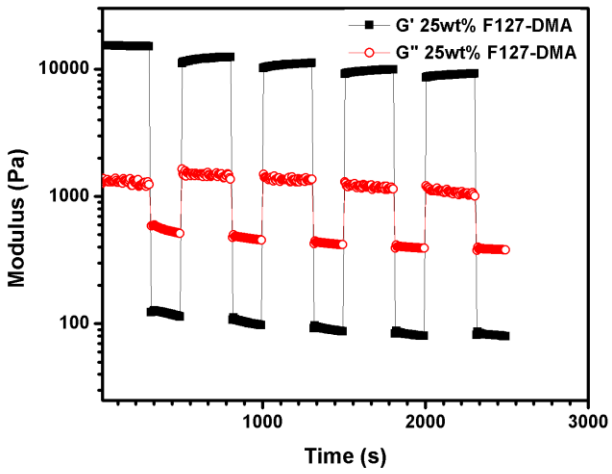

Figure 2. 2 Cyclic shear strain experiment for 25 wt % F127-DMA hydrogel.
Alternates between 5 min periods of low strain (1 %) and 3 min periods of high strain (100 %) performed at 21 ° C.

2.3.2 *Evaluation of ink printability*

Given that all the hydrogel ink formulations were temperature responsive and shear-thinning, we next sought to correlate the printability of the hydrogel inks to rheometrical differences. The critical printing parameters, which included the pressure exerted onto the gel in the syringe, the printing speed (the rate at which the nozzle moves across the surface), and the temperature of the printing environment, were kept constant at 20 psi, 5 mm/s and 21 °C, respectively. Each of the

inks was tested for printability by extruding the ink through a 410 μm I.D. nozzle. If there was a significantly large deviation from this value, then the hydrogel ink is not ideal for direct-write 3D printing. Filaments were extruded and analyzed with an optical microscope for differences in shape or diameter. "Printable" filaments were defined as those that produced continuous, tubular filaments with diameters close to the actual nozzle diameter. To define the error in printability, a term ε was defined using the equation:

$$\varepsilon = \frac{D_{filament} - D_{nozzle}}{D_{nozzle}} \times 100 \qquad (3)$$

where D_{filament} and D_{nozzle} are the measured diameter of the printed filament and diameter of the nozzle, respectively (Table 2.1).

Since that the hydrogel formulations in this study were shear-thinning, their flow behavior was approximated by the Hershel-Bulkley equation given by:

$$\sigma = \sigma_{dyn} + \mathrm{K}\dot{\gamma}^{\mathrm{n}} \qquad (4)$$

Where $\dot{\gamma}$ is the shear rate, K is the consistency index and n is the flow index. A plot of stress vs. shear rate shows a good fit to the model (R^2 = 0.99467, Supporting Information). As shown in Figure 2.3, the yield stresses were determined from the plot of shear stress versus shear rate, wherein the shear history of a hydrogel ink undergoing extrusion is simulated in the rheometer. An increasing shear stress was applied until the material yielded, after which the shear rate was reduced allowing the material to relax until it stopped flowing. The σ_{stat} was measured from the

change in the slope of the stress from the first part of the loop (increasing shear rate) while the σ_{dyn} was measured from the y-intercept ($\dot{\gamma} = 0\ s^{-1}$) of the same plot under decreasing shear rate.

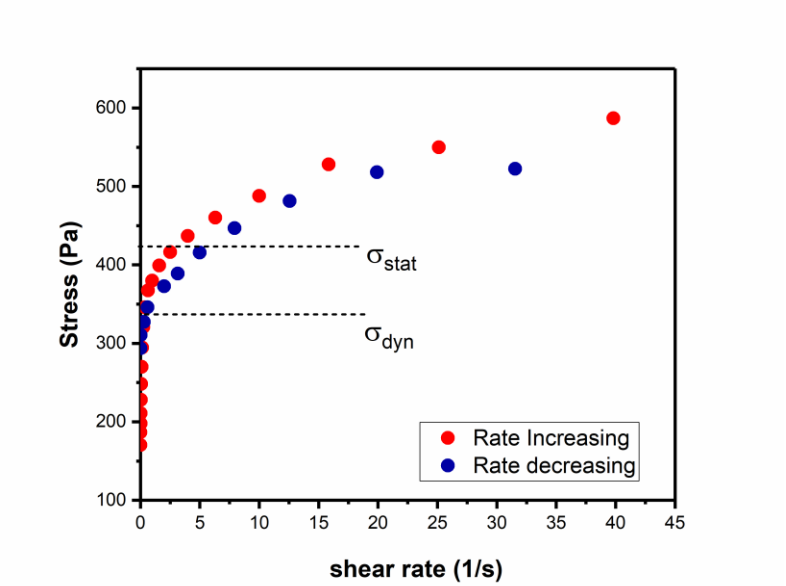

Figure 2. 3 A stress vs shear rate plot of a 30 wt % F127-DMA hydrogel.
The shear rate was increased until the material yielded (σ_{stat}), after which the shear rate was decreased to zero (σ_{dyn}). The static yield stress was obtained from the onset of the slope change while the shear rate was increased, while the dynamic yield stress was obtained from the y-intercept of the plot when shear rate was decreased.

We observed that some materials produced filaments which were much larger in size than the nozzle diameter while others showed minimal deviation. The σ_{dyn} values of the material closely matched their trend in printability. This indicated that of the materials investigated, the ones with a higher dynamic shear stress retained the filament shape and diameter more uniformly after extrusion. The native ink F127-DMA had better filament resolution at higher concentrations (30 wt %, ε= 7.3 %) in contrast to the filament diameter of the 25 wt % hydrogel. (ε= 186.6 %). Upon

addition of the functional monomers, the printability of the Pluronic hydrogel changed significantly (Figure 2.4).

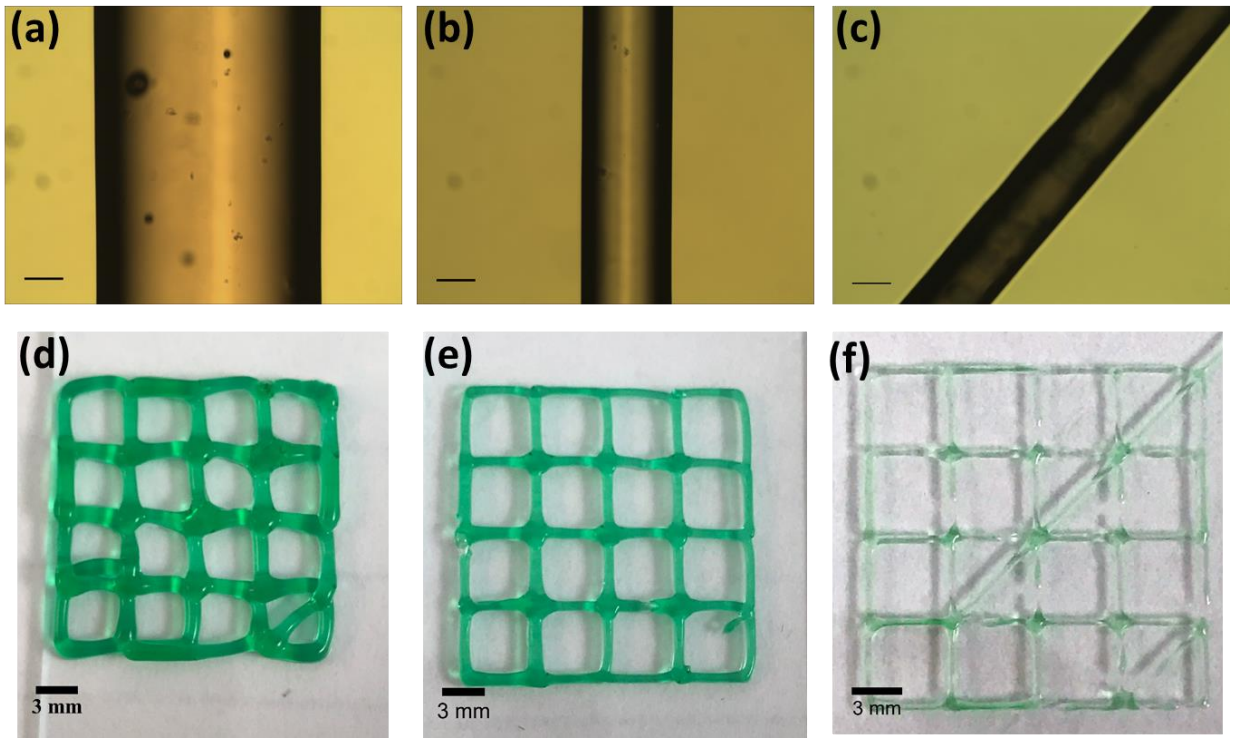

Figure 2. 4 Filaments and grids printed at 20 psi and 5mm/s.
(a) AA (10), (b) 30% F127-DMA, and (c) DMAEMA (10) under an optical microscope (scalebar represents 200 μm). Optical photographs of printed grid structures for (d) AA (10), (e) 30% F127-DMA, and (f) DMAEMA (10).

For example, a grid structure printed with 30 wt % F127-DMA showed good printability (~ 446 ± 10 μm) with good resolution in contrast to the hydrogel formulation with the AA additive (10 wt %), which had very broad extruded filaments (~ 750 ± 15 μm). The DMAEMA (10 wt %) containing hydrogel formulation had smaller diameter filaments (~ 270 ± 10 μm) under the same printing conditions. In addition to viscosity, the monomers also exhibited considerable influence upon the yield stresses of the material. The addition of DMAEMA in different proportions increased the σ_{dyn} of the ink. The protic AA monomer also showed similar trends, but to a much

lesser degree than the aprotic DMAEMA. On the other hand, HEA (10 wt %) behaved very similarly to the native 25 wt % F127-DMA, whereas HEA (4 wt %) caused the σ_{dyn} to decrease significantly. The addition of PEGDA monomers afforded an unexpected behavior. The formulation with lower PEGDA content (4 wt %) exhibited a reduction in σ_{dyn} while PEG-DA (10 wt %) was much stiffer with very high σ_{dyn} and showed high fidelity to the nozzle diameter (ε= 1.7 %). The cumulative set of results with the addition of these additives suggested that a σ_{dyn} value of ca. 300 Pa affords hydrogel filaments that correspond well to the I.D. of the nozzle.

Table 2. 2 Static yield stress values and optimized printing conditions for each hydrogel ink formulation.

POLYMER 1 (wt %)	ADDITIVE (wt %)	σ_{STAT} (Pa)	PRESSURE (psi)	PRINT SPEED (mm/s)	DIAMETER (μm)
F127-DMA (30)	-	394.14	20	5	440±5
F127-DMA (25)	-	224.64	15	20	770±25
F127-DMA (25)	PEG-DA (10)	454.18	20	3	410±20
F127-DMA (25)	DMAEMA (10)	414.01	20	3	415±10
F127-DMA (25)	DMAEMA (4)	356.98	20	5	468±20
F127-DMA (25)	HEA (10)	270.60	12	20	471±15
F127-DMA (25)	AA (10)	260.55	15	10	510±20
F127-DMA (25)	AA (4)	286.82	15	5	530±30
F127-DMA (25)	PEG-DA (4)	194.13	12	20	N/A
F127-DMA (25)	HEA (4)	17.30	12	20	N/A

It is, however, important to distinguish between the two parameters (σ_{stat} and σ_{dyn}) and their relationship to the hydrogel ink printability. Although the values of σ_{stat} and σ_{dyn} can be similar (Table 2.1 and Table 2.2) for our shear-thinning hydrogels, the static yield stress should dictate the extrusion pressure, while the σ_{dyn} should determine the quality of the filament shape. For example,

HEA (10 wt %) exhibited a lower yield stress (270 Pa) relative to the other formulations, and therefore, required less pressure (12 psi) to extrude the filament. At the same time, this HEA formulation also retained filament fidelity (relative to the nozzle I.D.) (ε = 12.15 %) as a consequence of its moderately good dynamic stress 250 Pa. The quality of the extruded filament decreased as the extrusion pressure was increased, which further demonstrates that extrusion pressure is an important parameter in direct-write 3D printing.

The reason behind the differences of the printability and the yield stresses due to the addition of monomers has yet to be fully elucidated. We hypothesize that the polarity and hydrogen bonding capability may be important parameters. Alexandridis *et. al.*[42,43] has also shown that the addition of co-solvents can alter the micelle formation of Pluronics in water by partitioning into different blocks of the macromolecule.[44] The co-solvents may cause local dehydration effects and changes in micelle packing that are comparable to those induced by changes in temperature. The extent and direction in which the co-solvents change the self-assembly behavior depends on the polarity of the added solvents. The differences in polarity of the additives used in this study may be causing the differences in material properties, and further investigations are underway to delineate the origins of these affects.

The optimized filament resolution for each of the formulations are listed in Table 2.2. These results were obtained by controlling print speed and extrusion pressure during the printing of a hydrogel ink (at 21 °C). The extrusion pressure is defined as the minimum pressure to extrude a smooth and continuous filament from a nozzle and was varied from 0 to 20 psi. For hydrogel materials, a minimal printing time is desired to minimize dehydration of the printed filaments over time. The printing speed in this study was varied between 2 to 25 mm/s. Table 2.2 also shows the static yield stresses along with the filament diameter produced by the different hydrogel inks.

Extrusion pressure and print speed are not mutually independent, and a higher extrusion pressure can be offset by a faster print speed. However, a closer examination of the extruded filaments under an optical microscope (Figure 2.5), showed that a higher extrusion pressure and print speed yielded filaments with non-uniform diameters due to uneven extrusion or jetting. For example, when 30% F127-DMA is printed at a lower print speed (5 mm/s), the filament obtained is smoother and more uniform than printing at 10 mm/s which afforded filaments with a variable width (~270 μm). A static yield stress greater than 450 Pa could not be extruded at 20 psi, which was the maximum pressure available for the direct-write 3D printer.

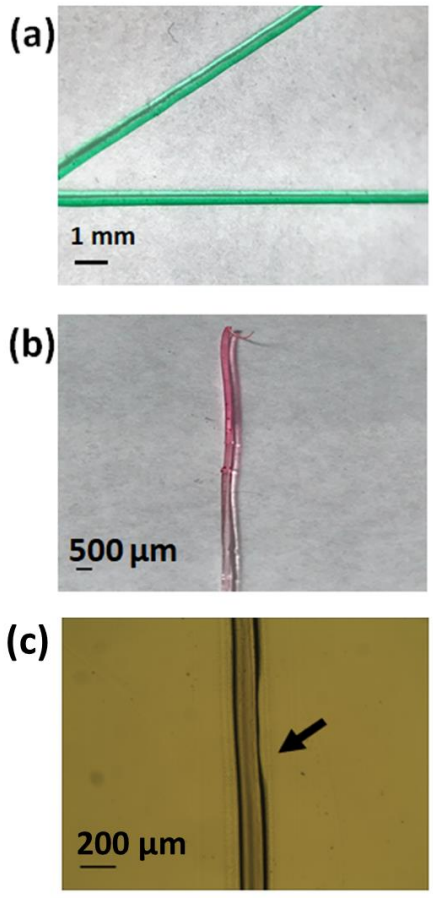

Figure 2. 5 30% F127-DMA extruded at different print speeds, (a) 5mm/s and (b, c) 10 mm/s.

2.3.3 *Rheometrical and tensile characterization of crosslinked hydrogel ink formulations*

The mechanical properties of the hydrogel formulations after the photo-initiated cross-linking was investigated by performing *in situ* UV curing rheometrical experiments. The storage modulus was recorded prior to, during, and after UV irradiation (Figure 2.6). The 25 wt % F127-DMA had a storage modulus of 143 kPa after curing. The storage modulus of the various PEG-DA formulations increased with increasing concentration of PEG-DA, ranging from 134 kPa to 429 kPa for 6 wt % to 20wt% PEG-DA, respectively. This drastic increase in storage moduli suggests that bis-functionalized PEG-DA increased the crosslinking density of the hydrogel.[45] Conversely, the storage modulus of each of the DMAEMA formulations decreases with increasing additive concentration, 100 kPa and 73 kPa for 4 wt % and 10 wt %, respectively. For the HEA and AA formulations, the storage modulus does not depend on the additive concentration and the equilibrium storage modulus after crosslinking is about 140 kPa and 130 kPa, respectively.

Figure 2.6 shows the change in storage modulus of the various hydrogel ink formulations as they undergo UV irradiation (N=3)

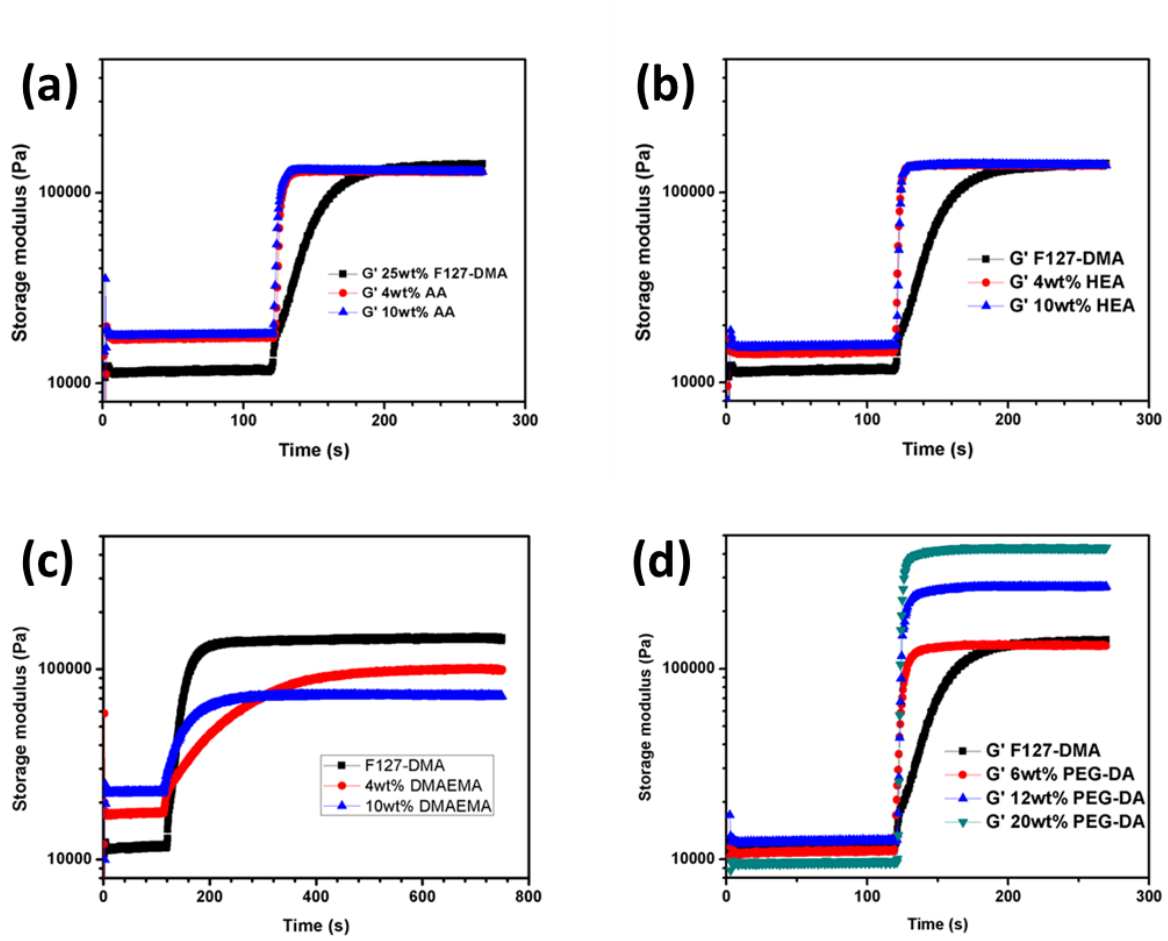

Figure 2. 6 Dynamic oscillatory UV cure experiments performed at 21 ° C.
There is an increase in storage modulus when the lamp is turned on 120 s after the start of the experiment for a total irradiation time of 600 s. (a) 25 wt % F127-DMA, AA (4), and AA (10) (b) 25 wt % F127-DMA, HEA (4), and HEA (10) (c) 25 wt % F127-DMA, DMAEMA (4), and DMAEMA (10) and (d) 25 wt % F127-DMA, PEG-DA (6), PEG-DA (12), and PEG-DA (20). Note that the x-axis for (c) ranges from 0-800 s.

The chemical structure of the different additives also influences the rate of polymerization. The monomers with acrylate groups (HEA, AA, and PEG-DA) all reach maximum storage modulus during UV irradiation faster than monomers with methacrylate groups (DMAEMA) and F127-DMA alone. Upon 290 s of UV irradiation, F127-DMA reached its maximum storage

modulus, while HEA and AA formulations reach equilibrium storage moduli within 15 s, and PEG-DA formulations within 35 s. DMAEMA formulations required a longer time period (394 s or 410 s for 4 wt % or 10 wt %, respectively) to reach their maximum storage moduli, likely a consequence of the slower reactivity of methacrylates.[46]

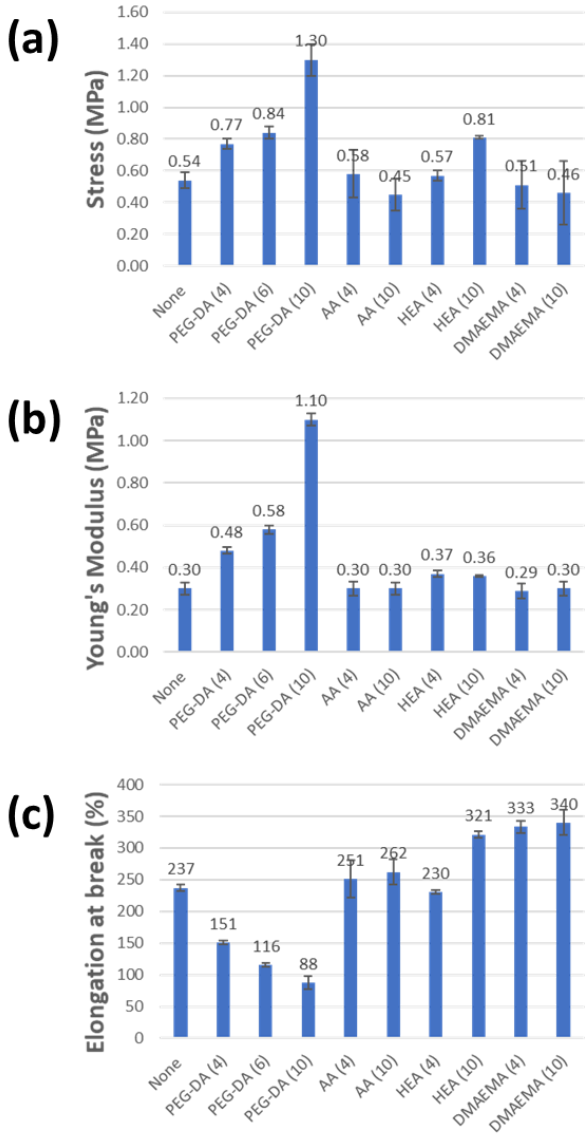

Figure 2. 7 Plots of the (a) tensile strength, (b) Young's modulus, and (c) elongation at break for each hydrogel ink formulation.

The elongation at break, ultimate tensile strength, and Young's modulus of the hydrogel ink formulations are summarized in Figure 2.7. The addition of PEG-DA increased the tensile strength and Young's modulus of F127-DMA. These two parameters increased with increasing amount of PEG-DA, with the maximum change in strength and Young's modulus coming from the 10 wt % PEG-DA formulation (240 % and 366 %, respectively) compared to native 25 wt % F127-DMA. However, as the concentration of PEG-DA was increased, the elongation at break decreased significantly (88 % for 10 wt % PEG-DA versus 237 % for native 25 wt % F127-DMA). The Young's moduli and ultimate tensile strength for AA and DMAEMA formulations remained unchanged in comparison to native 25 wt % F127-DMA. For HEA formulations, the stiffness and tensile strength increased with increasing concentration of monomer. The elongation at break was improved by 35 %, 41 %, and 43 % for 10 wt % HEA, AA, and DMAEMA, respectively. Thus, these results reveal that the additives can serve an important role in modifying the mechanical properties of the cross-linked hydrogels.

2.4 CONCLUSIONS

In this report, several hydrogel inks were formulated by the addition of reactive monomers, which included acrylic acid, 2-*N*,*N*-dimethylaminoethyl methacrylate, 2-hydroxyethyl acrylate, and poly(ethylene glycol) diacrylate to F127-DMA hydrogels. The printability of the resulting hydrogel inks prior to photo-polymerization, and the mechanical properties of the ink after photo-polymerization, were investigated. Prior to UV irradiation, the two critical rheological parameters that correlate to printability were the dynamic and the static yield stress. Materials with low dynamic yield stress, below 200 Pa, are not promising candidates for direct-write printing, as they do not retain their shape well enough to form a filament upon extrusion. On the other hand, we

observed that there was a correlation between the static yield stress and the pressure required to extrude the hydrogel ink from a 410 μm I.D. nozzle. At a printing pressure of 20 psi, the maximum value for the static yield stress that still afforded a smooth and continuous hydrogel filament was 450 Pa. Finally, we demonstrated that the monomer additives were covalently incorporated into the cross-linked hydrogels and had a significant affect upon the mechanical properties of the resulting hydrogels. The results of these findings can serve as a guide to the development of new functional shear-thinning hydrogel inks for direct-write 3D printing.

2.5 EXPERIMENTAL

2.5.1 *Materials*

Pluronic F-127 (BioReagent, powder, suitable for cell culture) was purchased from Sigma Life Science. Triethylamine (≥ 99.5%), 2-hydroxy-2-methylpropiophenone (97%), 2-hydroxyethyl acrylate (96%), acrylic acid (99%), 2-(dimethylamino)ethyl methacrylate (98%), methacryloyl chloride (97%; 200 ppm monomethyl ether hydroquinone as stabilizer), and poly(ethylene glycol) diacrylate (M_n 700 Da) were purchased from Sigma-Aldrich. Toluene (HPLC Grade, 99.9%) and diethyl ether (anhydrous) were purchased from Fisher Chemical.

2.5.2 *Functionalization of F127*

Pluronic F-127 (30 g, 2.4 mmol, 1.0 eq) was dried under vacuum for 24 hours, then dissolved in 275 mL of anhydrous toluene (dried using activated molecular sieves, Grade 514, 4Å) under N_2 atmosphere at 40 °C. Triethylamine (3.4 mL, 24 mmol, 10 eq) was added to the solution via syringe. The reaction mixture was cooled to 0 °C, then a solution of methacryloyl chloride (2.4 mL, 24 mmol, 10 eq) in 25 mL toluene was added dropwise over 30 minutes with constant stirring.

Following complete addition of methacryloyl chloride, the reaction mixture was stirred at 0 °C for 1 h, then warmed to room temperature and stirred for 24 h under N_2 atmosphere. The following day, the reaction mixture was warmed to 40 °C and vacuum-filtered through a fritted glass funnel with filter paper. The slightly turbid filtrate was concentrated under reduced pressure, then reconstituted in 300 mL fresh toluene and warmed to 40 °C. This process was repeated for a total of 3 filtrations. The transparent filtrate was concentrated under reduced pressure, then dissolved in 100 mL of toluene and precipitated with a large excess (800 mL) of anhydrous diethyl ether (dried over magnesium sulfate). The slurry was centrifuged at 4400 rpm for 15 min, and the supernatant was discarded. The solid residue was rinsed twice with fresh diethyl ether, and then centrifuged. F127-DMA was recovered as a fluffy, white powder and was dried under ambient conditions for 12 h. Finally, powder was dried under reduced pressure at 40 °C for 24 h. Dry F127-DMA (29 g) was transferred to amber glass containers and stored at 5 °C. ^{1}H NMR spectroscopy indicated 94-96% functionalization of chain ends. ^{1}H NMR sample was prepared in deuterochloroform at concentrations of 20 mg / mL (Supporting information) and ^{1}H NMR spectra was collected on a Brüker Avance 500 MHz spectrometer. Pluronic F127 has average poly (propylene oxide) block lengths of DP = 69 and poly(ethylene oxide) block lengths of DP = 97 (total M_n = 12,500 g / mol). In all F127-DMA spectra, the methyl groups of the poly (propylene oxide) block were calibrated to (69 x 3) = 207. The degree of DMA functionalization (f_n) was estimated by dividing the integrated methacrylate vinyl and methyl protons, as well as the PEO chain-end methylene protons, by their theoretical values. For example, 1.90 (vinyl, actual) / 2 (vinyl, theoretical) x 100 ≈ 95% functionalization of chain ends. The degree of DMA-functionalization is reported as a range of estimates, from lowest to highest. ^{1}H NMR (500 MHz, $CDCl_3$, 298 K): δ = 6.12 (m, 2H, H-CH=C) 5.56 (m, 2H, H-CH=C) 4.29 (t, 3J = 4.9 Hz; 4H, $CH_2OC(O)$) 3.79-3.40 (m, 1001H, CH_2O,

CH_3CHO) 1.93 (dd, 4J = 1.7 Hz, 4J = 0.9 Hz; 6H, $CH_3C(CO_2)=CH_2$) 1.12 (dd, 3J = 6.1 Hz, 4J = 4.4 Hz; 207H, CH_3CO).

2.5.3 *Preparation of hydrogel ink formulations*

The weight percentages provided (supporting information) are based on the total composition of the hydrogel including the aqueous solvent. F127-DMA (1.25 g) was dissolved in 3.75 g of deionized (DI) water and cooled at 4 °C overnight to prepare 25 wt % F127-DMA hydrogel. Photo radical generator, 2-hydroxy-2-methylpropiophenone (5 μL), was added to the hydrogel and vortexed, creating a homogenous solution. Then, the solution was allowed to equilibrate at 4 °C until bubbles were removed. Finally, the solution was warmed to room temperature to undergo a sol to gel transition, resulting in a shear-responsive gel. The same process was used to prepare the various 4 wt % and 10 wt % hydrogel ink formulations, with the additional step of replacing 0.2 g or 0.5 g of water with 0.2 g or 0.5 g of the additives, respectively. For example, 1.25 g F127-DMA and 0.5 g HEA were dissolved in 3.25 g DI water and cooled at 4 °C overnight to prepare the 10 wt % HEA formulation.

2.5.4 *Rheological characterization*

For rheological characterization of the materials, dynamic oscillatory experiments were performed on a TA Instruments Discovery Hybrid Rheometer-2 (DHR-2) equipped with a peltier. The instrument operates by applying a known displacement (strain) and measuring the material's resistance (stress) to the force. Rheological tests were conducted by depositing hydrogel between the rheometer base plate and 20 mm parallel plate geometry at a gap of 1 mm unless otherwise mentioned. Samples were equilibrated in an ice bath for at least 30 min and then were carefully loaded onto the Peltier plate at 5 °C and a preshear experiment was applied to eliminate the bubbles

from the sample. The sample was equilibrated at 21 °C for 8 min before each run. Viscosity versus shear rate experiments were performed under a shear rate increasing from 0.0001 to 50 s^{-1} then decreasing back to 0.0001 s^{-1} using a 40 mm cone and plate geometry with a cone angle of 1.019° using a solvent trap. Cyclic shear strain tests (frequency 1 Hz) were performed at 21 °C using alternating strains of 1% for 5 min and 100% for 3 min per cycle, to investigate the yielding and recovery behavior of the hydrogels. Temperature ramp experiments were performed at 1 Hz from 5−50 °C at 2 °C/min. Photo-curing was performed using a fully integrated smart swap LED photo curing accessory. A 600 s irradiation with 365 nm light at 5 mW/cm^2 intensity was triggered into the experiment, and the sample was monitored for a total of 1020 s at 1% strain and at 1 Hz (n=3).

2.5.5 *Preparation of tensile specimens*

All hydrogel formulations were brought below their T_{gel} and poured into ASTM D638 type V specimen molds. Each specimen was then brought back to 21 ^{o}C to induce gelation. Upon complete gelation, the specimens were cured for 30 minutes in a custom-fabricated curing chamber with sunlite 365 nm A19 UV Lamps. To prevent evaporation, tensile specimens were stored alongside moist Kim wipes in centrifuge tubes until the mechanical tests were conducted.

2.5.6 *Mechanical tests*

Tensile mechanical measurements were performed on as-prepared tensile specimens using an Instron 5585H load frame with a 50 N load cell and flat pneumatic grips. All tests were conducted using a crosshead rate of 10mm/min, until specimen failure. The dimensions of each specimen were measured with calipers prior to testing to ensure accurate calculation of stress and strain. At least five specimens of each formulation were tested. The Young's moduli were calculated from the linear region of stress vs strain curve.

2.5.7 *Printing of hydrogel inks*

All the polymer formulations were loaded into 10 ml syringes fitted with a barrel-shaped size 22 Metcal extrusion nozzle (410 µm I.D.) and allowed to equilibrate to the surrounding temperature of 21 °C before printing. The printing was performed on a Prusa I3 RepRap printer, where each ink printed single layered filament (n=3). This was photo-polymerized by UV irradiation for 60 s and then imaged with Nikon Eclipse E600 Pol fitted with a Optix Cam camera**.** The filament diameter analysis was done using ImageJ software. All CAD models were designed in Solidworks 2016. All printing was done using with printing parameters as mentioned later. The tip of the needle was positioned at a designated point on the support gel holder that served as the XYZ origin for all prints. Printing was controlled through standard 3DP software to generate G-code commands (Slic3r) from CAD-generated (Solidworks).

2.6 ACKNOWLEDGEMENTS

This chapter has been adapted from the following manuscript:

> Smith, P; Basu, A; Saha, A; Nelson, A. "Chemical Modification and Printability of Shear-thinning Hydrogel Inks for Direct-write 3D Printing" Polym. 2018, 152, 42-50. https://doi.org/10.1016/j.polymer.2018.01.070.

We acknowledge support from University of Washington, Seattle for start-up funding.

2.7 REFERENCES

1. Naficy, S.; Gately, R.; Gorkin, R.; Xin, H.; Spinks, G. M. 4D Printing of Reversible Shape Morphing Hydrogel Structures. *Macromol. Mater. Eng.* **2017**, 302, 413-419.
2. Bakarich, S. E.; Gorkin, R.; Panhuis, M. in het; Spinks, G. M. 4D Printing with Mechanically Robust, Thermally Actuating Hydrogels. *Macromol. Rapid Commun.* **2015**, *36*, 1211–1217.
3. Murphy, S. V.; Atala, A. 3D Bioprinting of Tissues and Organs. *Nat. Biotech.* **2014**, 32, 773–785
4. Martin, I.; Simmons, P. J.; Williams, D. F. Manufacturing Challenges in Regenerative Medicine. *Sci. Trans. Med.* **2014**, *6*, 232.
5. Guvendiren, M.; Lu, H. D.; Burdick, J. A. Shear-Thinning Hydrogels for Biomedical Applications. *Soft Matter* **2012**, *8*, 260–272.
6. (a) Sun, K.; Wei, T.-S.; Ahn, B. Y.; Seo, J. Y.; Dillon, S. J.; Lewis, J. A. 3D Printing of Interdigitated Li-Ion Microbattery Architectures. *Adv. Mater*. **2013**, 25, 4539–4543. (b) Wu, W.; DeConinck, A.; Lewis, J. A. Omnidirectional Printing of 3D Microvascular Networks. *Adv. Mater*. **2011**, 23, H178–H183.
7. Maiti, A.; Small, W.; Lewicki, J. P.; Weisgraber, T. H.; Duoss, E. B.; Chinn, S. C.; Pearson, M. A.; Spadaccini, C. M.; Maxwell, R. S.; Wilson, T. S. *Sci. Rep*. **2016**, 6 (1), 24871.
8. Lee, K. Y.; Mooney, D. J. Alginate: Properties and Biomedical Applications. *Prog. Polym. Sci.* **2012**, *37*, 106–126.
9. Wu, Z.; Su, X.; Xu, Y.; Kong, B.; Sun, W.; Mi, S. Bioprinting Three-Dimensional Cell-Laden Tissue Constructs with Controllable Degradation. *Sci. Rep.* **2016**, *6*, 24474.
10. Su, B.; Zhang, D.; Button, T. W. Micropatterning of Fine Scale Ceramic Structures. *J. Mater. Sci.* **2002**, *37*, 3123–3126.
11. Gratson, G. M.; Xu, M.; Lewis, J. A. Microperiodic Structures: Direct Writing of Three-Dimensional Webs. *Nature* **2004**, *428*, 386–386.
12. Smay, J. E.; Cesarano, J.; Tuttle, B. A.; Lewis, J. A. Directed Colloidal Assembly of Linear and Annular Lead Zirconate Titanate Arrays. *J. Am. Ceram. Soc.* **2004**, *87*, 293–295.
13. Billiet, T.; Vandenhaute, M.; Schelfhout, J.; Van Vlierberghe, S.; Dubruel, P. A Review of Trends and Limitations in Hydrogel-Rapid Prototyping for Tissue Engineering. *Biomaterials* **2012**, *33*, 6020–6041.
14. Truby, R. L.; Lewis, J. A. Printing Soft Matter in Three Dimensions. *Nature* **2016**, *540*, 371–378.
15. Sinha, G. Cell Presses. *Nat. Biotech.* **2014**, *32*, 716–719.
16. Derby, B. Printing and Prototyping of Tissues and Scaffolds. *Science* **2012**, *338*, 921–926.
17. Kang, H.-W.; Lee, S. J.; Ko, I. K.; Kengla, C.; Yoo, J. J.; Atala, A. A 3D Bioprinting System to Produce Human-Scale Tissue Constructs with Structural Integrity. *Nat. Biotech.* **2016**, *34*, 312–319.
18. Duan, B.; Hockaday, L. A.; Kang, K. H.; Butcher, J. T. 3D Bioprinting of Heterogeneous Aortic Valve Conduits with Alginate/Gelatin Hydrogels. *J. Biomed. Mater. Res. A* **2013**, *101*, 1255–1264.
19. Sundaram, S.; Kim, D. S.; Baldo, M. A.; Hayward, R. C.; Matusik, W. 3D-Printed Self-Folding Electronics. *ACS Appl. Mater. Interfaces* **2017**, 32290–32298.
20. Russo, A.; Ahn, B. Y.; Adams, J. J.; Duoss, E. B.; Bernhard, J. T.; Lewis, J. A. Pen-on-Paper Flexible Electronics. *Adv. Mater.* **2011**, *23*, 3426–3430.

21. Shi, Y.; Pan, L.; Liu, B.; Wang, Y.; Cui, Y.; Bao, Z.; Yu, G. Nanostructured Conductive Polypyrrole Hydrogels as High-Performance, Flexible Supercapacitor Electrodes. *J. Mater. Chem. A* **2014**, *2*, 6086–6091.
22. Biondi, M.; Ungaro, F.; Quaglia, F.; Netti, P. A. Controlled Drug Delivery in Tissue Engineering. *Adv. Drug Deliv. Rev.* **2008**, *60*, 229–242.
23. Lee, Y.-J.; Braun, P. v. Tunable Inverse Opal Hydrogel pH Sensors. *Adv. Mater.* **2003**, *15* (7–8), 563–566.
24. Holtz, J. H.; Asher, S. A. Polymerized Colloidal Crystal Hydrogel Films as Intelligent Chemical Sensing Materials. *Nature* **1997**, *389*, 829–832.
25. Hinton, T. J.; Jallerat, Q.; Palchesko, R. N.; Park, J. H.; Grodzicki, M. S.; Shue, H.-J.; Ramadan, M. H.; Hudson, A. R.; Feinberg, A. W. Three-Dimensional Printing of Complex Biological Structures by Freeform Reversible Embedding of Suspended Hydrogels. *Sci. Adv.* **2015**, *1*, e1500758
26. Müller, M.; Becher, J.; Schnabelrauch, M.; Zenobi-Wong, M. Nanostructured Pluronic Hydrogels as Bioinks for 3D Bioprinting. *Biofabrication* **2015**, *7*, 035006.
27. Custódio, C. A.; Reis, R. L.; Mano, J. F. Photo-Cross-Linked Laminarin-Based Hydrogels for Biomedical Applications. *Biomacromolecules* **2016**, *17*, 1602–1609.
28. Highley, C. B.; Rodell, C. B.; Burdick, J. A. Direct 3D Printing of Shear-Thinning Hydrogels into Self-Healing Hydrogels. *Adv. Mater.* **2015**, *27*, 5075–5079.
29. Lee, K. Y.; Mooney, D. J. Alginate: Properties and Biomedical Applications. *Prog. Polym. Sci.* **2012**, *37*, 106–126.
30. (a)Zhang, M., Vora, A., Han, W., Wojtecki, R.J., Maune, H., Le, A.B.A., Thompson, L.E., McClelland, G.M., Ribet, F., Engler, A.C., Nelson, A. Dual-Responsive Hydrogels for Direct-Write 3D Printing. *Macromolecules* **2015**, *48*, 6482–6488. (b) Karis, D. G.; Ono, R. J.; Zhang, M.; Vora, A.; Storti, D.; Ganter, M. A.; Nelson, A. Cross-Linkable Multi-Stimuli Responsive Hydrogel Inks for Direct-Write 3D Printing. *Polym. Chem.* **2017**, *8* (29), 4199–4206.
31. Schmolka, I. R. Artificial Skin I. Preparation and Properties of Pluronic F-127 Gels for Treatment of Burns. *J. Biomed. Mater. Res.* **1972**, *6* (6), 571–582.
32. Kabanov, A. V.; Batrakova, E. V.; Alakhov, V. Y. Pluronic® Block Copolymers as Novel Polymer Therapeutics for Drug and Gene Delivery. *J. Control. Release* **2002**, *82*, 189–212.
33. Müller, M.; Becher, J.; Schnabelrauch, M.; Zenobi-Wong, M. Printing Thermoresponsive Reverse Molds for the Creation of Patterned Two-Component Hydrogels for 3D Cell Culture. *J. Vis. Exp.* **2013**, *77*, e50632.
34. Mortensen, K.; Talmon, Y. Cryo-TEM and SANS Microstructural Study of Pluronic Polymer Solutions. *Macromolecules* **1995**, *28*, 8829–8834.
35. París, R.; Quijada-Garrido, I. Temperature- and pH-Responsive Behaviour of poly(2-(2-Methoxyethoxy) ethyl Methacrylate-Co-N,N-Dimethylaminoethyl Methacrylate Hydrogels. *Eur. Polym. J.* **2010**, *46*, 2156–2163.
36. Fussell, G. W.; Cooper, S. L. Endothelial Cell Adhesion on RGD-Containing Methacrylate Terpolymers. *J. Biomed. Mater. Res.* **2004**, *70A*, 265–273.
37. He, Y.; Yang, F.; Zhao, H.; Gao, Q.; Xia, B.; Fu, J. Research on the Printability of Hydrogels in 3D Bioprinting. *Sci. Rep.* **2016**, *6*, 29977.
38. Suntornnond, R.; Tan, E. Y. S.; An, J.; Chua, C. K. A Mathematical Model on the Resolution of Extrusion Bioprinting for the Development of New Bioinks. *Materials* **2016**, *9*,756.
39. M'Barki, A.; Bocquet, L.; Stevenson, A. Linking Rheology and Printability for Dense and Strong Ceramics by Direct Ink Writing. *Sci. Rep.* **2017**, *7*, 6017.

40. Deepa, G.; Thulasidasan, A. K. T.; Anto, R. J.; Pillai, J. J.; Kumar, G. V. Cross-Linked Acrylic Hydrogel for the Controlled Delivery of Hydrophobic Drugs in Cancer Therapy. *Int. J. Nanomed.* **2012**, *7*, 4077–4088.
41. Xu, F.-J.; Kang, E.-T.; Neoh, K.-G. pH- and Temperature-Responsive Hydrogels from Crosslinked Triblock Copolymers Prepared via Consecutive Atom Transfer Radical Polymerizations. *Biomaterials* **2006**, *27*, 2787–2797.
42. Alexandridis, P.; Ivanova, R.; Lindman, B. Effect of Glycols on the Self-Assembly of Amphiphilic Block Copolymers in Water. 1. Phase Diagrams and Structure Identification. *Langmuir* **2000**, *16*, 3676–3689.
43. Kaizu, K.; Alexandridis, P. Glucose-Induced Sphere to Ellipsoid Transition of Polyoxyethylene–polyoxypropylene Block Copolymer Micelles in Aqueous Solutions. *Colloids Surf. A* **2015**, *480*, 203–213.
44. Alexandridis, P.; Yang, L. SANS Investigation of Polyether Block Copolymer Micelle Structure in Mixed Solvents of Water and Formamide, Ethanol, or Glycerol. *Macromolecules* **2000**, *33*, 5574–5587.
45. Son, K.H.; Lee, J.W. Synthesis and Characterization of Poly(Ethylene Glycol) Based Thermo-Responsive Hydrogels for Cell Sheet Engineering. *Materials* **2016**, *9*, 854.
46. Odian, G. G. *Principles of polymerization*; Wiley-Interscience: Hoboken, NJ, 2004.

Chapter 3. ADDITIVE MANUFACTURING OF BOVINE SERUM ALBUMIN-BASED HYDROGELS AND BIOPLASTICS

3.1 ABSTRACT

Bio-sourced and biodegradable polymers for additive manufacturing could enable the rapid fabrication of parts for a broad spectrum of applications ranging from healthcare to aerospace. However, a limited number of these materials are suitable for vat photopolymerization processes. Herein, we report a two-step additive manufacturing process to fabricate robust protein-based constructs using a commercially available laser-based SLA printer. Methacrylated bovine serum albumin (MA-BSA) was synthesized and formulated into aqueous resins that were used to print complex 3D objects with a resolution comparable to a commercially available resin. The MA-BSA resins were characterized by rheometry to determine the viscosity and the cure rate, as both parameters can ultimately be used to predict the printability of the resin. In the first step of patterning these materials, the MA-BSA resin was 3D printed, and in the second step, the printed construct was thermally cured to denature the globular protein and increase the intermolecular noncovalent interactions. Thus, the final 3D printed part was comprised of both chemical and physical cross-links. Compression studies of hydrated and dehydrated constructs demonstrated a broad range of compressive strengths and Young's moduli that could be further modulated by adjusting the type and amount of co-monomer. The printed hydrogel constructs demonstrated good cell viability (> 95%) after a 21-day culture period. These MA-BSA resins are expected to be

compatible with other vat photopolymerization techniques including digital light projection (DLP) and continuous liquid interface production (CLIP).

3.2 INTRODUCTION

Bio-sourced materials that can replace existing petroleum-based materials are essential for sustainability. Moreover, bio-sourced materials with greater functionality will be required to meet the demands for the full spectrum of applications from aerospace to medicine. Additive manufacturing (AM) is an advanced fabrication method for creating complex 3D geometries and shows great promise for the future of manufacturing.[1,2] While many forms of AM exist, vat photopolymerization methods are advantageous for the speed at which high-resolution objects can be produced.[3,4] Laser-based stereolithography (SLA) 3D printing is a form of vat photopolymerization wherein a laser is scanned through photocurable resin to selectively cure the growing feature. This method of 3D printing provides micron-scale features with good accuracy and reproducibility.[5] Despite these advantages, SLA 3D printing is greatly limited by the availability of resins designed for additive processes.[6,7]

There have been few examples of bio-sourced materials that were designed for AM via a vat photopolymerization process.[8–12] Ideally, these materials should also be biodegradable to create a closed loop cycle. Other biodegradable resins have been reported, such as poly(alkyl fumarate) derivatives[13–15] and poly(lactide).[16] One of the main challenges in designing new oligomeric and polymeric resins for SLA is the increased viscosity of the resin based on concentration and molecular weight, as predicted by the Mark-Houwink equation.[17] According to literature reports, resins with a viscosity greater than 10 Pa·s result in long print times or unsuccessful prints because they do not adequately self-level and recoat the surface of the resin tray between layers.[18–20] The resin viscosity can be reduced by printing at elevated temperatures or incorporating reactive

diluents.[20] An alternative design strategy is to employ cyclic, branched, or dendritic polymer architectures, or cross-linked unimolecular particles, that have a lower intrinsic viscosity relative to a linear polymer of comparable molecular weight.[21,22]

In this report, we demonstrate a low viscosity, protein-based resin for vat photopolymerization using bovine serum albumin (BSA). BSA is a water-soluble, globular protein that is relatively abundant and low-cost. A critical aspect of this protein is that it is a single polypeptide chain that is folded into a globular particle. BSA is comprised of 68% α-helical structure and contains 17 disulfide bonds, with a net negatively charged surface that helps the protein resist aggregation.[23,24] Despite the high molecular weight of BSA, ~66.5 kDa, the protein's globular shape and negatively charged surface enables an extremely high solubility in water (up to ~40 % w/v) and low intrinsic viscosity relative to other linear polymers of similar molecular weight. BSA is particularly advantageous as a protein scaffold because it does not self-assemble or aggregate as its concentration in aqueous solution is increased. For example, at room temperature, gelatin methacrylate, a commonly used protein for 3D printing, forms a gel at concentrations above ~2 wt%, which limits its printability in a vat photopolymerization process.[25]

We developed a two-step process for 3D printing methacrylated BSA (MA-BSA). In the first step, the protein is photo-patterned three-dimensionally, and in a subsequent step, the protein is denatured during a thermal curing step to improve the mechanical properties of the printed construct (**Figure 3.1**). The resolution capabilities of the MA-BSA resin, using a commercially available Form 2 printer, were comparable to a commercially available resin (~200 μm), and 3D objects with complex lattice geometries were fabricated. The dual cross-linked network, comprised of chemical cross-links from the printing step and physical cross-links from the thermal curing step, afforded printed hydrogels and bioplastics with excellent mechanical properties. The

resulting hydrogels and bioplastics are suitable for stiff structural elements and were biocompatible and biodegradable.

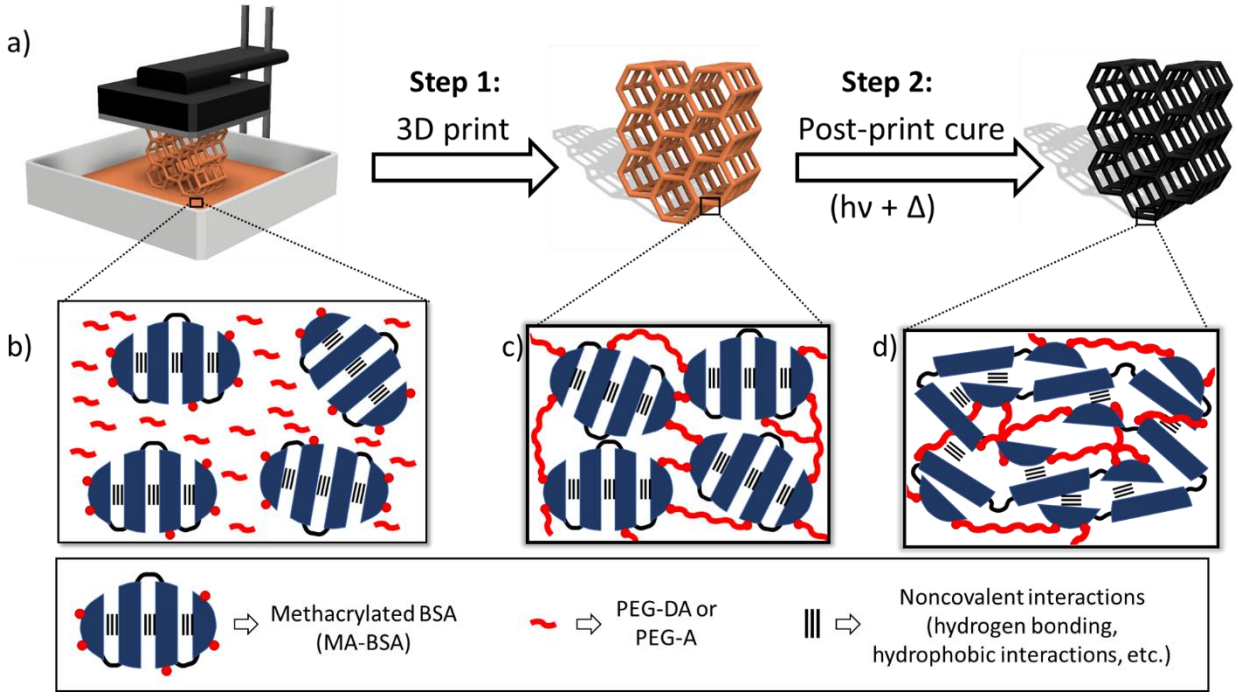

Figure 3. 1 Overview of fabrication of protein-based structures via SLA.

(a) idealized general scheme as shown involved a resin comprising (b) a solution of highly aqueous-soluble MA-BSA that was initially polymerized via photo-initiated free radical polymerization to afford a 3D printed construct. (c) The polymerized protein network was then cured by first irradiating with 400 nm light to induce further polymerization of any unreacted components, and then thermally cured (120 °C) for 3 h to afford (d) a denatured protein matrix which improved the mechanical properties of the printed construct.

3.3 Results and Discussion

Radical photopolymerization of acryloyl and methacryloyl groups is a common reaction scheme employed in the development of resins for vat photopolymerization.[4,31–37] The polymerization occurs rapidly, and the incorporation of multiple (meth)acryloyl groups per molecule decreases the time to reach the crossover point. We note that during the 3D printing step,

we did not seek to fully cure the structure as it was printed. Instead, the printed construct was sufficiently cross-linked to hold its form, and a post-print curing step (*h*□ and thermal) was employed to polymerize unreacted methacrylamide groups, denature the protein, and further improve the mechanical properties of the material.

Commercially available BSA was converted into MA-BSA by reaction with methacrylic anhydride in an aqueous buffer. Based on a TNBS assay, we determined that > 90% of the available lysines were converted into methacrylamide derivatives. We hypothesized that MA-BSA would make an excellent cross-linker and resin component based on the presence of multiple (ca. 27-31) methacrylamides present on the protein surface.[38] The MA-BSA was soluble in aqueous solutions at concentrations up to 40 wt%.

Circular dichroism (CD) spectroscopy was employed to assess whether the protein underwent significant changes to its secondary structure upon methacrylation. The CD spectra for the functionalized and unfunctionalized BSA were deconvoluted using BeStSel to estimate each protein's secondary structure. The BeStSel program produced similar values for both native and methacrylated BSA (**Table B.1**), which suggests that there was not a significant change in the overall secondary structure of the BSA after methacrylation.

The viscosity and the rate of photo-curing of MA-BSA formulations (**Table B.1**) were evaluated via rheometry and optimized for vat photopolymerization. Resins that have a high viscosity (> 10 Pa·s)[39,40] are slow to self-level and exert greater capillary forces that hamper vat photopolymerization. MA-BSA formulations over the range of 10–40 wt% in aqueous solution were investigated (**Figure 3.2a)**. Formulations up to 30 wt% MA-BSA maintained a low viscosity up to 0.035 Pa·s, with a more significant increase in the viscosity for 35 wt% and 40 wt% MA-BSA (1.56 Pa·s and 29.4 Pa·s, respectively). Based on these results, we formulated resins with 30

wt% and 35 wt% MA-BSA with the goal of maximizing protein content while maintaining a viscosity below 10 Pa·s.

The dwell time and intensity of the laser (405 nm) on the Form 2 printer are not adjustable, and thus, the photo-curing rate of the resin formulation must be optimized for the printer. Photo-rheometry was used to investigate the cure rates of the MA-BSA formulations by observing the storage and loss moduli, G' and G" respectively, over time (**Figure B.4**). For viscoelastic materials, G' represents the gel-like or elastic behavior and G" represents the sol-like or viscous behavior. Upon irradiation with 405 nm light, the liquid resin (G' < G") begins to cure and goes through a modulus crossover point (G' = G") to form a gel (G' > G"). Ruthenium tris(bipyridyl) chloride ($Ru(bpy)_3Cl$) and sodium persulfate (SPS) were used as the photo-initiating system for their excellent solubility in water and high molar extinction coefficient at 405 nm.[10,12] We observed that formulations comprising MA-BSA (30 wt%), $Ru(bpy)_3Cl$ (0.075 wt%) and SPS (0.24 wt%) did not cure at a rate appropriate for SLA printing (**Figure B.5**). In this case, nearly 30 s passed before G' began to increase, meaning little or no photo-curing occurred within the first 30 s of irradiation. This amount of time is not ideal for any type of SLA printing because it could require over 30 s of irradiation to cure each layer, which would result in exceedingly long print times. The slow cure rate may be attributed to the large size of BSA (~66.5 *k*Da) and limited number of methacrylamides available to form a cross-linked network. Based on these experiments, we hypothesized that the addition of a second reactive monomer could increase the cure rate of the resins. Thus, poly(ethylene glycol) diacrylate (PEG-DA, M_n 700 Da) or poly(ethylene glycol) methyl ether acrylate (PEG-A, M_n 480 Da) were included as additives in the formulations.

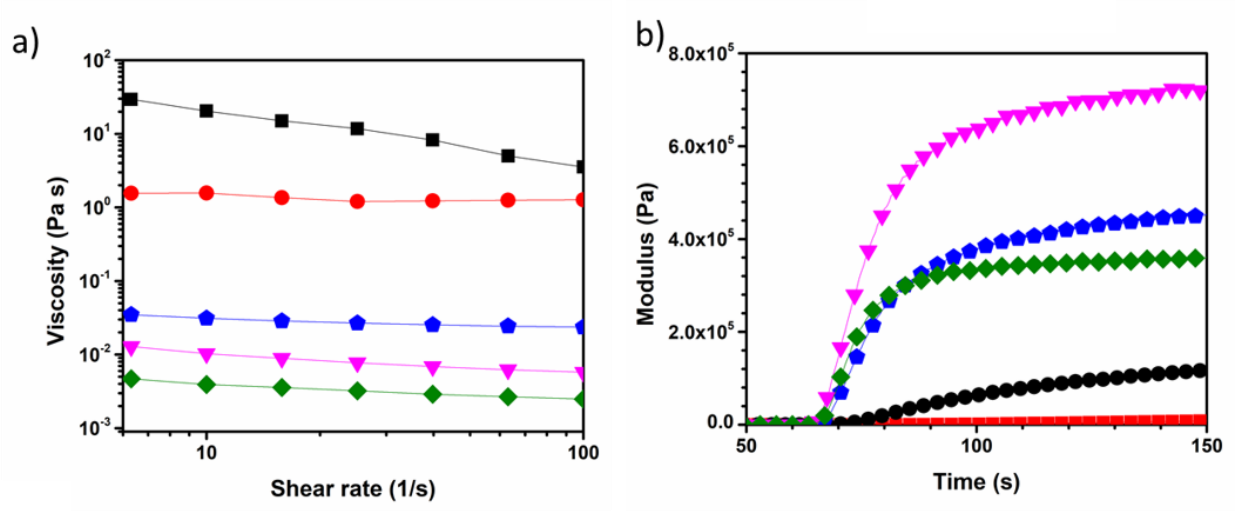

Figure 3. 2 Rheometry of MA-BSA formulations to determine viscosity and rate of photo-curing. (a) Viscosity versus shear rate data for 10–40 wt% MA-BSA formulations; 40 wt% MA-BSA (black squares), 35 wt% MA-BSA (red circles), 30 wt% MA-BSA (blue pentagons), 20 wt% MA-BSA (pink triangles), 10 wt% MA-BSA (green diamonds). (b) Photo-rheometry of 30 wt% MA-BSA resin with various amounts of co-monomer. The light source (400 nm) was turned on after 60 s; no co-monomer (red squares), 1 wt% PEG-DA (black circles), 5 wt% PEG-DA (blue pentagons), 10 wt% PEG-DA (pink triangles), 10 wt% PEG-A (green diamonds).

The time required to reach the crossover point ($G' = G''$) and the cure rate (based on the change in G' upon irradiation with 400 nm light) were used to assess the formulations for suitability in vat photopolymerization.[41,42] We first evaluated the time to reach the crossover point because it has been previously reported that the macromer conversion at the interface between layers should be slightly higher than the crossover point to ensure chemical bonding between layers.[43] Additionally, a successful SLA resin should surpass its crossover point quickly. The 30 wt% MA-BSA formulation without any additives required 18 s of irradiation to reach its crossover point. The addition of a co-monomer into the formulation decreased the required irradiation time to 5.5 s, 4.0 s, and 2.2 s for 1 wt%, 5 wt%, 10 wt% PEG-DA, respectively. The mono-functional co-monomer,

PEG-A, also decreased the time to reach crossover point to 3.2 s. The cure rate based on the increase in G' over time was assessed for each of the formulations over the first 30 s of irradiation (**Table B.1**). The storage modulus of the formulation without any co-monomer increased at a rate of 0.006 *k*Pa/s while the incorporation of monomer increased the cure rate by orders of magnitude (three orders of magnitude for 1 wt% and four orders of magnitude of Pa/s for both 5 and 10 wt% added co-monomer). Importantly, the addition of co-monomer does not alter the viscosity, and the resin remains well within the working range for SLA printing (**Figure B.6**).

All of the formulations were then evaluated using a Form 2 printer. The 30 wt% MA-BSA formulations with the inclusion of 5–10 wt% additive (**Table B.1**, entries 3-5) were the best candidates as resins, which was consistent with our rheometrical experiments. The resin formulation with 1 wt% co-monomer (**Table B.1**, entry 1), which had a slow cure rate (1.61 kPa/s), printed the initial 10–20 layers before the printed part delaminated from the build plate. Delamination occurred because the resin did not cure quickly enough to crosslink the layers together, for the given irradiation dose. The formulations with 35 wt% MA-BSA were also unacceptable as resins because they were too viscous. Based on these results, the successful formulations met two requirements: (i) a resin viscosity that was < 3.4 Pa·s, and (ii) a cure rate that was ≥ 13.5 *k*Pa/s.

Table 3. 1 Rheometrical data for MA-BSA resin formulations.

Entry	wt % MA-BSA	Comonomer (wt%)	Printable	Viscosity (Pa s)	Crossover point (s)	G' rate of change[a] (kPa/s)
1	30	--	No	0.035	18	0.006
2	30	PEG-DA (1)	No	0.020	5.5	1.61
3	30	PEG-DA (5)	Yes	0.061	4.0	14.0
4	30	PEG-DA (10)	Yes	0.267	2.2	24.2
5	30	PEG-A (10)	Yes	0.072	3.2	13.5
6	35	PEG-DA (5)	No	8.2	4.5	19.1
7	35	PEG-DA (10)	No	3.4	4.8	50.1

[a] Based on the first 30 s of irradiation.

The resolution of each print is governed by both the printer (laser spot size and laser accuracy) and the curing kinetics of the resin. We designed a CAD file for a test structure with an array of fins (100–1000 µm), as well as an array of square holes with widths that ranged from 400–2000 µm. This test structure (**Figure 3.3**) was used to evaluate the resolution limit of the formulation with the highest printable MA-BSA content (**Table 3.1**, entry 4). The smallest fin printed was 243 µm and the smallest square hole resolved was 700 µm. In comparison, the smallest feature fin and hole for a commercially available acrylate resin was 173 µm and 400 µm, respectively. In general, the printed constructs were consistent with the CAD model, and on average, the MA-BSA printed structure deviated higher (67.5 µm) than the dimensions designed in the CAD model. The commercially available resin exhibited a similar behavior but with a smaller deviation from the CAD model (8.9 µm).

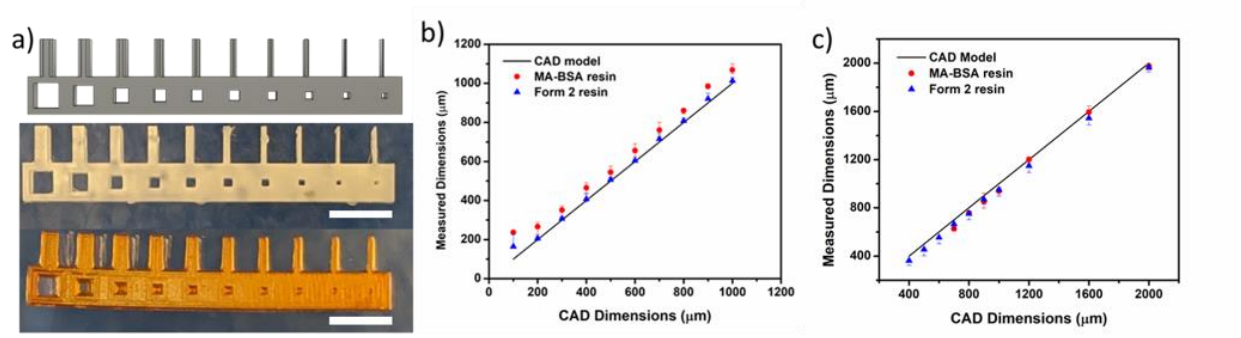

Figure 3. 3 A test structure comprised of lines/spaces.
Varying line widths from (100 μm to 1000 μm) and square holes with dimensions from (400 μm to 2000 μm) were designed and printed using the Form 2 printer. (a) Comparison of the original CAD, printed commercial resin, and formulation with 30 wt% MA-BSA and 10 wt% PEG-DA (top to bottom, scale bar 5 mm). Plots showing the measured feature sizes for the printed (b) lines and (c) square holes versus the CAD.

The as-printed structures of the MA-BSA formulation were hydrogels with a water content of ca. 60 wt%. These structures were subjected to a post-print curing step to induce further cross-linking within the material. The printed hydrogel samples were first irradiated with 400 nm light for 1.5 h to further polymerize any unreacted meth(acrylate)s. Then, the samples were dehydrated and thermally cured at 120 °C for 180 min. During this step, the BSA was also expected to denature, which would increase the physical associations between protein chains via hydrophobic and hydrogen bonding interactions.[44–47] The printed and cured samples afforded bioplastics that could be re-hydrated to re-form the hydrogel. Swelling studies were performed to determine the amount of water the printed constructs absorbed (swelling ratio, q) and the gel fraction for the material (based on percent mass loss) for each formulation after printing (**Table B.2**). The thermally cured samples exhibited lower swelling ratios and decreased mass loss relative to the non-cured samples. This difference could be attributed to the denaturation of BSA during the

thermal curing step, which would lead to an increase in intermolecular interactions between protein chains. As a result, there are more physical associations present within the re-hydrated hydrogel matrix and the swelling ratio decreased.

We also observed that the difunctional monomer, PEG-DA, afforded samples with a lower swelling ratio (2.64) and mass loss after swelling (3.3%) than the monofunctional monomer, PEG-A (3.32 and 9.9%, respectively). Additionally, the concentration of PEG-DA was inversely related to the swelling ratio as 5 wt% PEG-DA absorbed 81% more water than 10 wt% PEG-DA. Thus, the reswelling behavior of the MA-BSA hydrogels can be controlled by altering the cross-linking density of the matrix.

The same formulation that was used to print the resolution test structures (**Table 3.1**, entry 4) was also used to print lattice geometries. These examples demonstrate the successful printing of complex geometries with good resolution (250 μm struts) (**Figure 3.4**). The SEM images of the printed lattices also showed that 50 μm layer heights were clearly visible when angled structures were formed from offset stacked layers (**Figure 3.4c**).

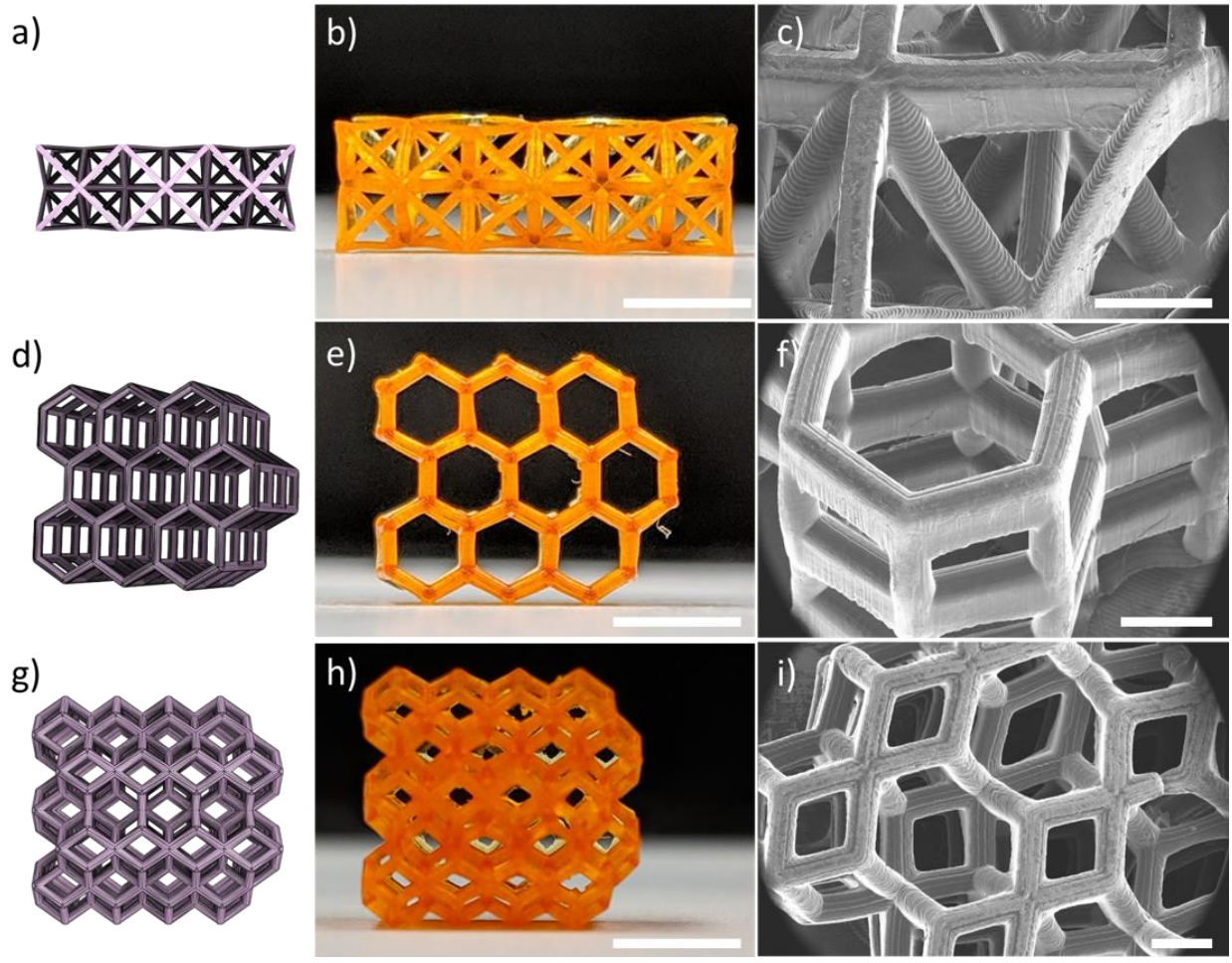

Figure 3. 4 Lattice designs were 3D printed using the 30 wt% MA-BSA and 10 wt% PEG-DA formulation.

The CAD images are shown in (a), (d), and (g); optical images are shown in (b), (e), and (h) where the scale bars represent 5 mm; representative SEM images are shown in (c), (f), and (i) where the scale bars represent 1 mm. The samples shown are the dehydrated constructs after the thermal cure.

Uniaxial compression tests were performed to characterize the mechanical properties of cured hydrogels and the corresponding dried bioplastics. The compressive stress-strain curves are plotted in **Figure 3.5a–d** and the corresponding data are in **Table B.4** and **B.5**, where we compared the

monofunctional PEG-A versus difunctional PEG-DA as the additive. As expected, the samples with 10 wt% PEG-A had a lower compressive modulus than samples with 10 wt% PEG-DA (3.3 MPa and 6.3 MPa, respectively). This is attributed to the linear chain architecture afforded by PEG-A versus the highly crosslinked network chain architecture that arose from PEG-DA. Samples that were thermally cured exhibited markedly different stress-strain curves compared to un-cured samples. For the hydrated samples (hydrogels), the thermal treatment increased the compressive strength by over 500%, 175%, and 200% for 5 wt% PEG-DA, 10 wt% PEG-DA and 10 wt% PEG-A, respectively. This increase in compressive strength could be the result of the formation of increased noncovalent interactions between the protein chains, forming a dual-crosslinked network. Secondary structural motifs such as intermolecular β-sheets have previously been reported for BSA upon thermal denaturation above 70 °C.[48] The presence of additional intermolecular physical cross-linking was corroborated by the decreased swelling ratio of the thermally cured samples (**Table B.2**). Biologically sourced hydrogels printed via SLA are typically quite soft with compressive moduli ranging from 70–120 kPa and compressive strengths up to 910 kPa.[9,12] MA-BSA hydrogels have higher compressive moduli and strengths, up to 6.26 and 4.27 MPa, respectively, due to the high concentration of MA-BSA and the formation of additional crosslinks upon denaturation. Thus, our system expands the range of mechanical properties of hydrogels fabricated via vat photopolymerization.

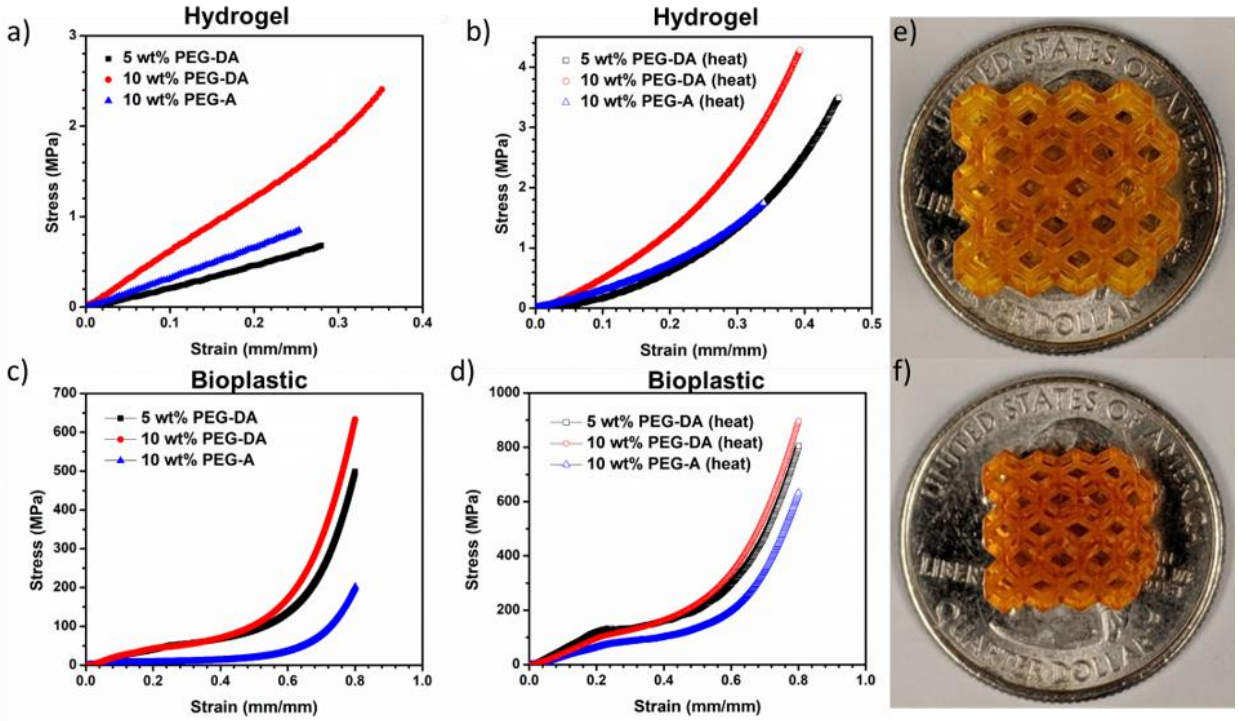

Figure 3. 5 Representative compressive stress vs. strain curves and printed structures. (a) the 'as printed' hydrogel after equilibrium swelling in water, (b) the thermally cured hydrogel after equilibrium swelling, (c) the 'as printed' sample in the dehydrated state, and (d) the thermally cured sample in the dehydrated state. Photographs of a representative printed lattice are shown in the sample in the (e) swollen hydrogel state and (f) dehydrated state.

Similar to the hydrogels, the bioplastics (**Figure 3.5c**) with PEG-A additive exhibited a lower modulus than the bioplastics with PEG-DA (73 MPa and 473 MPa, respectively). The thermally cured and dehydrated samples (**Figure 3.5d**) also had a much higher modulus than the uncured samples (**Figure 3.5c**). For example, the 10 wt% PEG-A bioplastic had a compressive modulus of 73 MPa without the thermal cure and increased to 382 MPa with the thermal cure. Surprisingly, the thermally cured 5 wt% PEG-DA bioplastic had the highest modulus of all formulations, 638 MPa. We attribute this to the greater proportion of MA-BSA present relative to the total polymer

content. The higher concentration of MA-BSA increased the number of inter-protein non-covalent interactions that could occur.

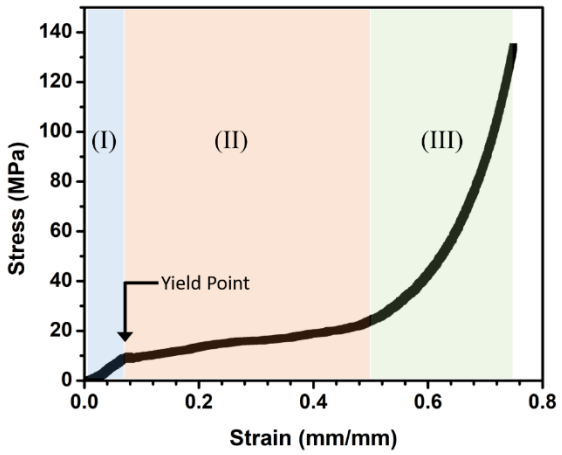

Figure 3. 6 Compressive stress vs strain curve for a cast dehydrated sample of 30 wt% MA-BSA. Three distinct regions were observed and are highlighted: (I) linear elastic region, (II) plateau region, and (III) strain-stiffening region.

Interestingly, the bioplastics that were tested in their dehydrated state did not fail by brittle fracture. Instead, they exhibited plastic deformation and flattened into a disk under compressive load. **Figure 3.6** shows a representative compressive stress versus strain curve for a dehydrated sample of 30 wt% MA-BSA and highlights three distinct regions in the graph. Beyond the linear elastic region, there is a distinct yield point, beyond which plastic deformation occurs. We attribute this behavior to the high molecular weight of the BSA, which can become irreversibly stretched as the load is increased.

Using a fluorescent live/dead assay, the biocompatibility of the MA-BSA formulations with 3T3 fibroblasts was assessed after a 21-day culture period (**Figure 3.7**). Overall cell viability was good (> 95%), with some hydrogel samples outperforming even conventional tissue-culture poly(styrene). The greatest viability was observed on the 1 wt% PEG-DA hydrogels. While the

viability decreased as a function of increasing PEG-DA content, this difference from the 1 wt% formulation was not statistically significant (**Figure 3.7b**). The slight decrease in viability is likely due to a decrease in cell adhesion as PEG-DA concentration in the hydrogels increases. This phenomenon has been observed in prior studies and with a variety of cell types. For example, Mazzoccoli et al. reported that human breast cancer cells had an average initial cell viability of 79 ± 7.9% in hydrogels containing 20 wt % PEG-DA, and that this viability plummeted to an average of 36 ± 7.0% in 40 wt % PEG-DA gels.[49] Similarly, Nuttelman et al. reported that human mesenchymal stem cells (hMSCs) cultured on 10 wt % PEG-DA hydrogels that were not functionalized with RGD binding groups exhibited poor viability (approximately 15%), while hMSCs cultured on PEGDA-RGD hydrogels exhibited significantly improved viability (approximately 75%).[50] In our study, cell viabilities were generally quite high relative to these reported values for plain PEG-DA, and this might be due to the presence of BSA in our composite hydrogels, which has been shown to promote the activity of matrix proteins such as fibronectin and thus improve cell adhesion.[51,52] It should be noted that even with the observed decrease in viability in our study, cell viability levels were still on par with that of fibroblasts that were cultured on standard tissue culture plates. Interestingly, it also appeared that as PEG-DA content increased, cultured fibroblasts displayed a tendency to form 3D aggregates that formed on top of a layer of adherent cells.

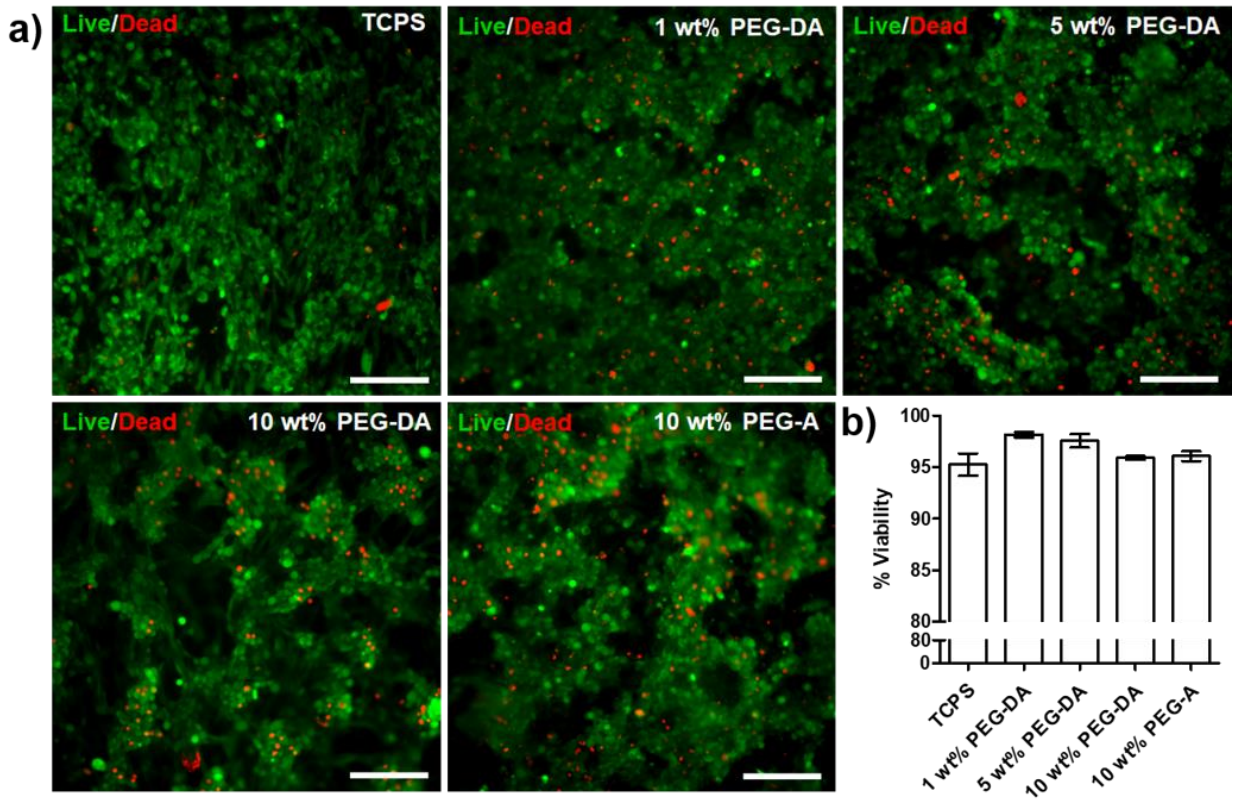

Figure 3. 7 MA-BSA hydrogels are biocompatible with fibroblasts.
(a) Representative live/dead staining of fibroblasts on tissue culture polystyrene (TCPS) and on composite hydrogels with varying PEG-DA and PEG-A content. Scale bars: 200 μm. (b) A high percentage of cells remained viable on hydrogels over a 21-day culture period and viability was comparable to that of TCPS controls.

Finally, the biodegradability of the printed constructs was confirmed by subjecting the printed resin to a protease. The enzymatic degradability of a cross-linked and cured MA-BSA sample (in the absence of any co-monomer) was confirmed by incubating the sample at 37 °C with proteinase K (2 mg/mL). The sample that was cured only with 400 nm irradiation was digested within 2 h, whereas the sample that was irradiated and thermally cured was completely digested within 16 h (**Figure B.7**). However, the formulations comprised of MA-BSA and PEG-DA as a co-monomer showed a slower rate of enzymatic degradation. After 1 week of incubation at 37 °C, the irradiated

and thermally cured sample degraded and lost 22.0% of its mass (**Table B.3)**. Thus, the addition of the co-monomer significantly reduced the ability of the enzyme to completely degrade the structure. We are currently investigating other cross-linkers that can further enhance or control the degradability of the matrix.

3.4 CONCLUSION

In conclusion, we developed a protein-based resin for SLA printing biodegradable hydrogels and bioplastics using a commercial 3D printer. MA-BSA is a versatile platform to create resins on account of its high solubility in water and its low intrinsic viscosity. A two-step procedure was utilized which involved first, patterning the resin using a Form 2 printer, and second thermally curing the printed construct to denature the protein, thus producing a robust 3D structure. The resin was optimized for printability with the inclusion of PEG-DA or PEG-A as a co-monomer. The resin viscosity and rate of photo-curing were critical parameters that determined the printability of the resin. The formulations that exhibited the best printability had viscosities that were < 3.4 Pa·s and a cure rate that was ≥ 13.5 kPa/s. The MA-BSA resin formulations performed comparably to a commercially available acrylic resin for the Form 2 printer, with 'as printed' dimensions as small as 230 µm. Upon thermal curing and dehydration, the printed constructs isotropically decreased in size to resolve features down to 170 µm. The printed and thermally cured constructs had excellent mechanical properties for both the re-hydrated hydrogel and the dehydrated bioplastic (compressive strength of 4.27 MPa at break and 97 MPa at 20% strain, respectively). To the best of our knowledge, this is the first time that a protein's folded and unfolded conformations have been utilized as a switch that facilitates its 3D printing and subsequent physical cross-linking. We expect this strategy to be useful in any type of vat photopolymerization process including, digital light projection (DLP) and continuous layer interface printing (CLIP). These protein-based

constructs could be well-suited for load bearing applications in tissue engineering and in medical devices.

3.5 EXPERIMENTAL

3.5.1 *Materials*

All materials were purchased from Sigma Aldrich unless otherwise stated. Methacrylic anhydride (94%), Tris(2,2′-bipyridyl)dichlororuthenium(II) hexahydrate ($Ru(bpy)_3Cl$) (99.95%), poly(ethylene glycol) diacrylate (M_n 700 Da), poly(ethylene glycol) methyl ether acrylate (M_n 480 Da) and sodium persulfate (SPS) were used as received. Ultra-pure and ultra-low fatty acid content BSA was purchased from Nova Biologics. Formlabs Standard Clear Resin (FLGPCL04) was purchased from Formlabs.

3.5.2 *Methacrylation of BSA*

A procedure for methacrylation of gelatin was modified and used to methacrylate BSA.[26] In short, BSA (20 g, 0.3 mmol) and $NaHCO_3$ / Na_2CO_3 buffer (200 mL, 0.25 M, pH 9.0) were added to a 1000 mL round-bottom flask equipped with a magnetic stir bar. The mixture was stirred in an ice bath until the BSA dissolved completely. Then, methacrylic anhydride (4 mL, 27 mmol, ~2.5 eq. per lysine residue) was added dropwise to the BSA solution over 10 min. The reaction mixture was stirred in an ice bath for 1 h. The crude product was diluted and dialyzed against deionized (DI) water for 48 h. After lyophilization, the product was isolated as a white powder of MA-BSA (18.3 g, 91.5 % yield). The percent functionalization of the available lysines of BSA with methacryloyl functionalities was determined using a 2,4,6-trinitrobenzene sulfonate (TNBS) assay.[27] The TNBS assay is a method used to quantify primary amino groups by *N*-

trinitrophenylation of primary amines, which have high absorption at 335 nm. BSA and MA-BSA were dissolved in carbonate-bicarbonate buffer at a concentration of 20 µg/mL. A 0.01% (w/v) solution of TNBS (0.25 mL) was added to 0.5 mL of each protein solution. The samples were incubated at 37 °C for 2 h. To quench the reaction, 0.25 mL of 10% SDS and 0.125 mL of 1 N HCl were added to each sample. The absorption of each solution was measured at 335 nm with a UV/VIS spectrophotometer (Agilent 8453, **Figure B.1**). The absorbance of the MA-BSA was compared to the absorbance of native BSA and the percent functionalization was then calculated as follows:

$$\%\ functionalization = \frac{Abs_{BSA} - Abs_{MABSA}}{Abs_{BSA}}\ x\ 100$$

3.5.3 *Characterization of secondary structure*

Circular dichroism (CD) spectroscopy (Jasco J-720 spectropolarimeter) was used to evaluate the structure of BSA in solution after methacrylation. The experiments were performed at 25 °C in 1 mm quartz cuvettes. The wavelength of the CD spectrum was measured from 190 to 270 nm, with a step resolution of 0.2 nm, a scanning rate of 100 nm/min, a 1 s response time, and 2.0 nm bandwidth. The spectra displayed for native BSA and MA-BSA were an average of 8 spectra (**Figure B.2**). Solvent-corrected CD spectra were analyzed using the BeSTSel web server (http://bestsel.elte.hu) to estimate the secondary structure.[28,29]

3.5.4 *Preparation of MA-BSA based resin for vat photopolymerization*

All resin formulations were prepared in amber bottles and covered in aluminum foil to prevent auto-polymerization. The weight percentages are based on the total composition of the resin, including the aqueous solvent. As a representative example, we describe here the preparation of the resin with 30 wt% MA-BSA and 5 wt% poly(ethylene glycol) diacrylate (PEG-DA). First, 0.3 g of PEG-DA was dissolved in 3.66 mL of DI water, then 1.8 g of MA-BSA was slowly added to this solution with gentle mixing until dissolved. Next, 0.075 wt% $Ru(bpy)_3Cl$ dissolved in 120 µL of DI water and 0.24 wt% SPS dissolved in 120 µL of DI water were sequentially dissolved into the resin formulation. The final resin formulation was covered in aluminum foil and stored at 4 °C until use. To prepare other formulations, the same procedure was followed, changing only the co-monomer and DI water quantities.

3.5.5 *Fabrication of MA-BSA hydrogels using SLA printing*

A Formlabs Form 2 printer was used to fabricate the hydrogel constructs. The build plate and resin tray were modified to reduce the total volume of resin required to print. The build plate was cut down to 45 mm x 45 mm and a 48 mm x 78 mm x 28 mm border was 3D printed on a Flashforge® Creator Pro, then glued to the resin tray to form a small reservoir within the standard resin tray. 3D constructs were designed with Autodesk® Fusion 360 or downloaded from Thingiverse®. The resin was poured into the reservoir and ice was placed around the outside of the reservoir to prevent the temperature of the resin from increasing during printing. Hydrogel constructs were then printed in the Form 2's Open Mode with a layer height of 50 µm. Upon completion of the print, samples were removed from the build plate, rinsed in DI water to remove any uncured resin, and post cured in a custom photo-curing chamber (Quans, 400 nm, 1 mW/cm^2) for 90 min. Some samples were

further thermally cured. These samples were air-dried after the photo-curing step, then placed in a 120 °C oven for 180 min.

3.5.6 *Swelling experiments*

3D printed cylindrical disks (10 mm diameter x 5 mm height) were used for mass loss and swelling experiments. After printing and post-photo curing, the disks were lyophilized to obtain the initial dry weight ($m_{dry,i}$). Samples were then submerged in an excess of DI water and weighed after 1 day ($m_{swollen}$). The swollen samples were then freeze-dried and weighed again (m_{dry}). The mass loss and swelling ratio (q) were calculated as follows:

$$\%\, mass\ loss = \left(\frac{m_{dry,i} - m_{dry}}{m_{dry,i}}\right) \times\ 100\%$$

$$q = \frac{m_{swollen}}{m_{dry}}$$

3.5.7 *Rheometry*

Rheometry was performed on a TA Instruments Discovery Hybrid Rheometer-2. Viscosity versus shear rate experiments were performed at a shear rate increasing from 1-100 s^{-1} using a 40 mm cone and plate geometry with a cone angle of 1.019°, a solvent trap, and a gap height of 26 µm. Due to surface tension effects, only the range from 6-100 Pa·s was reported.[30] To conduct photo-rheometry experiments, the rheometer was outfitted with a collimated light source (λ = 400 nm, 10 mW cm^{-2}, Thorlabs) that was turned on 60 seconds after the start of the experiment. Using a 20 mm parallel plate and a gap height of 1000 µm, the storage and loss moduli were monitored for a total of 150 seconds at 1% strain and 6.28 rad/s.

3.5.8 *Uniaxial compression testing*

Compression testing was performed using an Instron 5585H load frame with a 2 *k*N and 50 *k*N load cell for hydrated and dehydrated samples, respectively. Cylindrical compression samples (10 mm diameter x 5mm height) were 3D printed as described above. Samples were tested both in their dehydrated state and at equilibrium swelling with DI water. Thermally treated samples were air dried after photo-curing, placed in a 120 °C oven for 180 min, then tested either in their dehydrated state or at equilibrium swelling. All tests were conducted at room temperature (22 °C) using a crosshead rate of 1.3 mm/min until specimen failure or 80% strain. Prior to testing, the hydrated samples were removed from the DI water and blotted dry with a Kim wipe. Then, the dimensions of each specimen were measured with a digital caliper. At least 5 specimens of each formulation were tested. The modulus, compressive strength, and toughness were determined from the resulting stress-strain curve. The toughness was determined by calculating the area under the stress-strain curves using Matlab. The compressive modulus was determined from the slope of the elastic region of the stress-strain curve.

3.5.9 *Scanning electron microscopy*

Scanning electron microscopy (SEM) samples were air dried after printing and imaged using an Apreo-S SEM operated at 2.0 *k*V.

3.5.10 *Print resolution and accuracy*

The accuracy and resolution of the MA-BSA resin was compared with the commercial Form 2 resin by printing test structures with various sized features. The test structure was designed to have hollow squares that increase in size from 400 μm to 2000 μm and posts that range from 100

μm to 1000 μm. The dimensions of the printed features were measured using ImageJ and compared to the CAD dimensions (**Figure 3.3 and B.9**).

3.5.11 *Cell culture and biocompatibility assessment*

Hydrogel films 1 mm thick and 5 mm in diameter were inserted into wells of a poly(styrene) 96-well culture plate. NIH/3T3 murine fibroblasts (ATCC, VA, USA) were then seeded onto these films at a density of 1 x 10^5 cells/cm^2 and cultured in high-glucose Dulbecco's Modified Eagle Medium (DMEM) (Invitrogen, MA, USA) supplemented with 10% fetal bovine serum and 1% penicillin-streptomycin (Invitrogen). Cultures were maintained for 21 days before cells were stained with a live/dead viability kit (Invitrogen) following the protocol provided by the manufacturer. Stained samples were removed and placed into new wells with fresh medium at the time of imaging to ensure that we were not imaging cells that had adhered to the bottom of the wells. No other seeding densities were tested, and no images were taken prior to 21 days. The samples were imaged using a widefield fluorescence microscope (A1R, Nikon Instruments, NY, USA) at 20X magnification. Live cells appeared green (calcein-AM excitation/emission: 488/515 nm), while dead cells appeared red (ethidium homodimer-1 excitation/emission: 570/602 nm). Analysis of the images was conducted using ImageJ image processing software (National Institutes of Health, MD, USA).

3.5.12 *Enzymatic degradation of printed constructs*

For the *in vitro* degradation study, hexagonal lattice structures were printed using formulation 4 (**Table 3.1**) and degraded in a solution of proteinase K. The lattice structures were initially weighed, then incubated at 37 °C in either Tris-$CaCl_2$ buffer (pH 8 0.1 M, GoldBio) with a final proteinase K concentration of 2 mg/mL, or the Tris-$CaCl_2$ buffer alone as a control. Every 24

hours, the lattices were removed from solution, blotted dry with a Kim wipe, weighed, then placed into a fresh solution of enzyme or buffer. Optical images were taken at different time points.

3.6 ACKNOWLEDGEMENTS

"Reprinted (adapted) with permission from: Smith, P; Narupai, B; Tsui, J; Millik, S; Shafranek, R; Kim, D; Nelson, A. "Additive Manufacturing of Bovine Serum Albumin-Based Hydrogels and Bioplastics" Biomacromolecules 2020, 21, 484-492 https://doi.org/10.1021/acs.biomac.9b01236. Copyright 2020, American Chemical Society."

This research was supported by the UW Royalty Research Fund.

3.7 REFERENCES

1. Gao, W.; Zhang, Y.; Ramanujan, D.; Ramani, K.; Chen, Y.; Williams, C. B.; Wang, C. C. L.; Shin, Y. C.; Zhang, S.; Zavattieri, P. D. Computer-Aided Design The Status , Challenges , and Future of Additive Manufacturing In. *Comput. Des.* **2015**, *69*, 65–89. DOI: 10.1016/j.cad.2015.04.001.
2. Shafranek, R. T.; Millik, S. C.; Smith, P. T.; Lee, C.; Boydston, A. J.; Nelson, A. Stimuli-Responsive Materials in Additive Manufacturing. Prog. Polym. Sci. 2019, 93, 36–67. DOI: 10.1016/j.progpolymsci.2019.03.002.
3. Appuhamillage, G. A.; Chartrain, N.; Meenakshisundaram, V.; Feller, K. D.; Williams, C. B.; Long, T. E. 110th Anniversary: Vat Photopolymerization-Based Additive Manufacturing: Current Trends and Future Directions in Materials Design. *Ind. Eng. Chem. Res.* **2019**, *58*, 15109–15118. DOI: 10.1021/acs.iecr.9b02679.
4. Bagheri, A.; Jin, J. Photopolymerization in 3D Printing. *ACS Appl. Polym. Mater*. **2019**, *1*, 593–611. DOI: 10.1021/acsapm.8b00165.
5. Wilts, E. M.; Pekkanen, A. M.; White, B. T.; Meenakshisundaram, V.; Aduba, D. C.; Williams, C. B.; Long, T. E. Vat Photopolymerization of Charged Monomers: 3D Printing with Supramolecular Interactions. *Polym. Chem.* **2019**, *10*, 1442–1451. DOI: 10.1039/c8py01792a.
6. Ngo, T. D.; Kashani, A.; Imbalzano, G.; Nguyen, K. T. Q.; Hui, D. Additive Manufacturing (3D Printing): A Review of Materials, Methods, Applications and Challenges. *Compos. Part B Eng.* **2018**, *143*, 172–196. DOI: 10.1016/j.compositesb.2018.02.012.
7. Ligon, S. C.; Liska, R.; Stampfl, J.; Gurr, M.; Mulhaupt, R. Polymers for 3D Printing and Customized Additive Manufacturing. *Chem. Rev.* **2017,** *117*, 10212-10290. DOI: 10.1021/acs.chemrev.7b00074.
8. Ding, R.; Du, Y.; Goncalves, R.; Francis, L.; Reineke, T. Sustainable near UV-Curable Acrylates Based on Natural Phenolics for Stereolithography 3D Printing. *Polym. Chem.* **2019**,

10, 1067. DOI: 10.1039/c8py01652f.
9. Kim, S. H.; Yeon, Y. K.; Lee, J. M.; Chao, J. R.; Lee, Y. J.; Seo, Y. B.; Sultan, T.; Lee, O. J.; Lee, J. S.; Yoon, S.; Hong, I.; Khang, G.; Lee, S.; Yoo, J. Park, C. Precisely Printable and Biocompatible Silk Fibroin Bioink for Digital Light Processing 3D Printing. *Nat. Commun.* **2018**, *9*, 1620. DOI: 10.1038/s41467-018-03759-y.
10. Lim, K. S.; Schon, B. S.; Mekhileri, N. V.; Brown, G. C. J.; Chia, C. M.; Prabakar, S.; Hooper, G. J.; Woodfield, T. B. F. New Visible-Light Photoinitiating System for Improved Print Fidelity in Gelatin-Based Bioinks. *ACS Biomater. Sci. Eng.* **2016**, *2* , 1752–1762. DOI: 10.1021/acsbiomaterials.6b00149.
11. Poldervaart, M. T.; Goversen, B.; Ruijter, M. De; Abbadessa, A.; Melchels, P. W.; Cumhur, F. O.; Dhert, W.; Vermonden, T.; Alblas, J. 3D Bioprinting of Methacrylated Hyaluronic Acid (MeHA) Hydrogel with Intrinsic Osteogenicity. *PLoS One* **2017**, *12*, e0177628. DOI: 10.1371/journal.pone.0177628.
12. Lim, K.; Levato, R.; Costa, P.; Castilho, M.; Alcala-Orozco, C.; van Dorenmalen, K.; Melchels, F.; Gawlitta, D.; Hooper, G.; Malda, J.; Woodfield, T. Bio-Resin for High Resolution Lithography-Based Biofabrication of Complex Cell-Laden Constructs. *Biofabrication* **2018**, *10*, 034101. DOI: 10.1088/1758-5090/aac00c.
13. Dilla, R. A.; Motta, C. M. M.; Snyder, S. R.; Wilson, J. A.; Wesdemiotis, C.; Becker, M. L. Synthesis and 3D Printing of PEG-Poly(Propylene Fumarate) Diblock and Triblock Copolymer Hydrogels. *ACS Macro Lett.* **2018**, *7*, 1254–1260. DOI: 10.1021/acsmacrolett.8b00720.
14. Childers, E. P.; Wang, M. O.; Becker, M. L.; Fisher, J. P.; Dean, D. 3D Printing of Resorbable Poly (Propylene Fumarate) Tissue Engineering Scaffolds. *Mater. Res. Soc.* **2015**, *40*, 119–126. DOI: 10.1557/mrs.2015.2.
15. Choi, J.; Wicker, R.; Lee, S.; Choi, K.; Ha, C.; Chung, I. Fabrication of 3D Biocompatible / Biodegradable Micro-Scaffolds Using Dynamic Mask Projection Microstereolithography. *J. Mater. Process. Technol.* **2009**, *209*, 5494–5503. DOI: 10.1016/j.jmatprotec.2009.05.004.
16. Seck, T. M.; Melchels, F. P. W.; Feijen, J.; Grijpma, D. W. Designed Biodegradable Hydrogel Structures Prepared by Stereolithography Using Poly (Ethylene Glycol)/ Poly (D , L -Lactide) -Based Resins. *J. Control. Release* **2010**, *148*, 34–41. DOI: 10.1016/j.jconrel.2010.07.111.
17. Hiemenz, P. C.; Lodge, T. *Polymer Chemistry*, 2nd ed.; CRC Press: Boca Raton, 2007.
18. Hinczewski, C.; Corbel, S.; Chartier, T. Ceramic Suspensions Suitable for Stereolithogiaphy. *J. Eur. Ceram. Soc.* **1998**, *18*, 583–590. DOI: 10.1016/S0955-2219(97)00186-6.
19. Sutton, J. T.; Rajan, K.; Harper, D. P.; Chmely, S. C. Lignin-Containing Photoactive Resins for 3D Printing by Stereolithography. *ACS Appl. Mater. Interfaces* **2018**, *10*, 36456–36463. DOI: 10.1021/acsami.8b13031.
20. Luo, Y.; Le Fer, G.; Dean, D.; Becker, M. L. 3D Printing of Poly(Propylene Fumarate) Oligomers: Evaluation of Resin Viscosity, Printing Characteristics and Mechanical Properties. *Biomacromoles* **2019**, *20*, 1699-1708. DOI: 10.1021/acs.biomac.9b00076.
21. Seiler, M. Hyperbranched Polymers : Phase Behavior and New Applications in the Field of Chemical Engineering. *Fluid Phase Equilib.* **2006**, *241*, 155–174. DOI: 10.1016/j.fluid.2005.12.042.
22. Voit, B. I.; Lederer, A. Hyperbranched and Highly Branched Polymer Architectures s Synthetic Strategies and Major Characterization Aspects. *Chem. Rev.* **2009**, *109*, 5924–5973. DOI: 10.1021/cr900068q
23. Reed, R. G.; Feldhoff, R. C.; Clute, O.; Peters, T. Fragments of Bovine Serum Albumin

Produced by Limited Proteolysis. Conformation and Ligand Binding. *Biochemistry* **1975**, *14*, 4578–4583. DOI: 10.1021/bi00692a004.
24. Ueki, T.; Hiragi, Y.; Kataoka, M.; Inoko, Y.; Amemiya, Y.; Izumi, Y.; Tagawa, H.; Muroga, Y. Aggregation of Bovine Serum Albumin Upon Cleavage of Its Disulfide Bonds, Studied by the Time-Resolved Small-Angle X-Ray Scattering Technique with Synchrotron Radiation. *Biophys. Chem. 23*, 115–124. DOI: 10.1016/0301-4622(85)80069-7.
25. Gauvin, R.; Chen, Y.; Woo, J.; Soman, P.; Zorlutuna, P.; Nichol, J. W.; Bae, H.; Chen, S.; Khademhosseini, A. Microfabrication of Complex Porous Tissue Engineering Scaffolds Using 3D Projection Stereolithography. *Biomaterials* **2012**, *33*, 3824–3834. DOI: 10.1016/j.biomaterials.2012.01.048.
26. Shirahama, H.; Lee, B. H.; Tan, L. P.; Cho, N. Precise Tuning of Facile One-Pot Gelatin Methacryloyl (GelMA) Synthesis. *Sci. Rep.* **2016**, *6*, 31036. DOI: 10.1038/srep31036.
27. Adamczyk, M.; Buko, A.; Chen, Y.; Fishpaugh, J. R.; Gebler, J. C.; Johnson, D. D. Characterization of Protein — Hapten Conjugates . 1 . Matrix-Assisted Laser Desorption Ionization Mass Spectrometry of Immuno BSA — Hapten Conjugates and Comparison with Other. *Bioconjug. Chem.* **1994**, *5*, 631–635. DOI: 10.1021/bc00030a019.
28. Micsonai, A.; Wien, F.; Kernya, L.; Lee, Y.; Goto, Y.; Réfrégiers, M.; Kardos, J. Accurate Secondary Structure Prediction and Fold Recognition for Circular Dichroism Spectroscopy. *Proc. Natl. Acad. Sci. U. S. A.* **2015**, 3095–3103. DOI: 10.1073/pnas.1500851112.
29. Micsonai, A.; Wien, F.; Bulyaki, E.; Kun, J.; Eva, M.; Lee, Y.; Goto, Y.; Matthieu, R.; Kardos, J. BeStSel : A Web Server for Accurate Protein Secondary Structure Prediction and Fold Recognition from the Circular Dichroism Spectra Andr As. *Nucleic Acids Res.* **2018**, *46*, 315–322. DOI: 10.1093/nar/gky497.
30. Ewoldt, R. H.; Johnston, M. T.; Caretta, L. M. *Complex Fluids in Biological Systems*; Spagnolie, S., Ed.; **2015**. DOI: 10.1007/978-1-4939-2065-5_6.
31. Schwartz, J. J.; Boydston, A. J. Multimaterial Actinic Spatial Control 3D and 4D Printing. *Nat. Commun.* **2019**, *10*, 791. DOI: 10.1038/s41467-019-08639-7.
32. Bhattacharjee, N.; Parra-cabrera, C.; Kim, Y. T.; Kuo, A. P.; Folch, A. Desktop-Stereolithography 3D-Printing of a Poly (Dimethylsiloxane) -Based Material with Sylgard-184 Properties. *Adv. Mater.* **2018**, *30*, 1800001. DOI: 10.1002/adma.201800001.
33. Dolinski, N. D.; Page, Z. A.; Callaway, E. B.; Eisenreich, F.; Garcia, R. V; Chavez, R.; Bothman, D. P.; Hecht, S.; Zok, F. W.; Hawker, C. J. Solution Mask Liquid Lithography (SMaLL) for One-Step , Multimaterial 3D Printing. *Adv. Mater.* **2018**, *30*, 1800364. DOI: 10.1002/adma.201800364.
34. Hegde, M.; Meenakshisundaram, V.; Chartrain, N.; Sekhar, S.; Tafti, D.; Williams, C. B.; Long, T. E. 3D Printing All-Aromatic Polyimides Using Mask-Projection Stereolithography : Processing the Nonprocessable. *Adv. Mater.* **2017**, 29, 1701240. DOI: 10.1002/adma.201701240.
35. Palaganas, N. B.; Mangadlao, J. D.; Leon, A. C. C. De; Palaganas, J. O.; Pangilinan, K. D.; Lee, Y. J.; Advincula, R. C. 3D Printing of Photocurable Cellulose Nanocrystal Composite for Fabrication of Complex Architectures via Stereolithography. *ACS Appl. Mater. Interfaces* **2017**, *9*, 34314–34324. DOI: 10.1021/acsami.7b09223.
36. de Beer, M. P. De; Laan, H. L. Van Der; Cole, M. A.; Whelan, R. J.; Burns, M. A.; Scott, T. F. Rapid , Continuous Additive Manufacturing by Volumetric Polymerization Inhibition Patterning. *Sci. Adv.* **2019**, *5*, eaau8723. DOI: 10.1126/sciadv.aau8723.
37. Zhu, W.; Tringale, K. R.; Woller, S. A.; You, S.; Johnson, S.; Shen, H.; Schimelman, J.;

Whitney, M.; Steinauer, J.; Xu, W.; Yaksh, T.; Nguyen, Q.; Chen, S. Rapid Continuous 3D Printing of Customizable Peripheral Nerve Guidance Conduits. *Mater. Today* **2018**, *21*, 951–959. DOI: 10.1016/j.mattod.2018.04.001.
38. Torres, O. B.; Jalah, R.; Rice, K. C.; Li, F.; Antoline, J. F. G.; Iyer, M.; Jacobson, A.; Boutaghou, M.; Alving, C.; Matyas, G. Characterization and Optimization of Heroin Hapten-BSA Conjugates : Method Development for the Synthesis of Reproducible Hapten-Based Vaccines. *Anal. Bioanal. Chem.* **2014**, *406*, 5927–5937. DOI: 10.1007/s00216-014-8035-x.
39. Mondschein, R.; Kanitkar, A.; Williams, C. B., Verbridge, S. S.; Long, T. E. Polymer Structure-Property Requirements for Stereolithographic 3Dprinting of Soft Tissue Engineering Scaffolds. *Biomaterials* **2017**, *140*, 170–188. DOI: 10.1016/j.biomaterials.2017.06.005.
40. Schüller-Ravoo, S.; Teixeira, S. M.; Feijen, J.; Grijpma, D. W.; Poot, A. A. Flexible and Elastic Scaffolds for Cartilage Tissue Engineering Prepared by Stereolithography Using Poly(Trimethylene Carbonate)-Based Resins. *Macromol. Biosci.* **2013**, *13*, 1711–1719. DOI: 10.1002/mabi.201300399.
41. Mezger, T. G. *The Rheology Handbook*, 4th ed. Vincentz Network. **2014**.
42. ASTM Standard D4473, 2008 (2016), "Dynamic Mechanical Properties: Cure Behavior," ASTM International, West Conshohocken, PA, 2003 DOI 10.1520/D4473-08R16, Www.Astm.Org. **2016**.
43. Melchels, F. P. W.; Feijen, J.; Grijpma, D. W. A Review on Stereolithography and Its Applications in Biomedical Engineering. *Biomaterials* **2010**, *31*, 6121–6130. DOI: 10.1016/j.biomaterials.2010.04.050.
44. Gosal, W. S.; Ross-murphy, S. B. Globular Protein Gelation. *Curr. Opin. Colloid Interface Sci.* **2000**, *5*, 188–194. DOI: 10.1016/S1359-0294(00)00057-1.
45. Chen, J.; Ma, X.; Dong, Q.; Song, D.; Hargrove, D.; Vora, S.; Ma, A.; Lu, X.; Lei, Y. Self-Healing of Thermally-Induced, Biocompatible and Biodegradable Protein Hydrogel. *RSC Adv.* **2016**, *6*, 56183–56192. DOI: 10.1039/c6ra11239k.
46. Clark, A. H.; Kavanagh, G. M.; Ross-murphy, S. B. Globular Protein Gelation-Theory and Experiment. *Food Hydrocoll.* **2001**, *15*, 383-400. DOI: 10.1016/S0268-005X(01)00042-X.
47. Baler, K.; Michael, R.; Szleifer, I.; Ameer, G. A. Albumin Hydrogels Formed by Electrostatically Triggered Self- Assembly and Their Drug Delivery Capability. *Biomacromolecules* **2014**, *15*, 3625–3633. DOI: 10.1021/bm500883h.
48. Murayama, K.; Tomida, M. Heat-Induced Secondary Structure and Conformation Change of Bovine Serum Albumin Investigated by Fourier Transform Infrared Spectroscopy. *Biochemistry* **2004**, *43*, 11526–11532. DOI: 10.1021/bi0489154.
49. Mazzoccoli, J. P.; Feke, D. L.; Baskaran, H.; Pintauro, P. N. Mechanical and Cell Viability Properties of Crosslinked Low- and High-Molecular Weight Poly (Ethylene Glycol) Diacrylate Blends. *J. Biomed. Mater. Res. Part A* **2009**, *93A*, 558–566. DOI: 10.1002/jbm.a.32563.
50. Nuttelman, C. R.; Tripodi, M. C.; Anseth, K. S. Synthetic Hydrogel Niches That Promote HMSC Viability. *Matrix Biol.* **2005**, *24*, 208–218. DOI: 10.1016/j.matbio.2005.03.004.
51. Zhu, L.; Jiang, J.; Zhu, B.; Xu, Y. Immobilization of Bovine Serum Albumin onto Porous Polyethylene Membranes Using Strongly Attached Polydopamine as a Spacer. *Colloids Surf. B: Biointerfaces* **2011**, *86*, 111–118. DOI: 10.1016/j.colsurfb.2011.03.027.
52. Koblinski, J. E.; Wu, M.; Demeler, B.; Jacob, K.; Kleinman, H. K. Matrix Cell Adhesion Activation by Non-Adhesion Proteins. *J. Cell Sci.* **2005**, *118*, 2965–2974. DOI: 10.1242/jcs.02411.

Chapter 4. METHACRYLATED BSA (MABSA) AND TANNIC ACID COMPOSITE MATERIALS FOR 3D PRINTING TOUGH AND MECHANICALLY FUNCTIONAL PARTS

4.1 ABSTRACT

Protein-based materials continue to show promise as potential alternatives to petroleum-based materials. 3D printing of protein-based materials is expected to further extend their application to new frontiers. However, existing 3D printable protein-based materials are generally limited by their poor range of mechanical properties and difficult processing. Herein, we develop a three-step additive manufacturing workflow to fabricate tough protein-based composite hydrogels and bioplastics with a range of mechanical properties. First, methacrylated bovine serum albumin (MABSA)-based aqueous resins were 3D printed via stereolithography (SLA). Next, the materials were treated with tannic acid (TA) to introduce additional noncovalent interactions within the network to improve mechanical properties via a means of energy dissipation. In the last step, a denaturing 120 °C thermal cure served to further enhance mechanical properties via formation of intermolecular β-sheets and other noncovalent interactions. The combination of TA treatment and thermal cure virtually eliminated rehydration of the materials, enabling application as bioplastics. Compression and tensile studies of 3D printed constructs demonstrated a range of ultimate strengths, elastic moduli and toughnesses that could be modulated by adjusting resin composition and post-print treatment protocol. 3D printed hydrogels enzymatically degraded up to 85% after

30 days in pepsin solution. To highlight the diverse mechanical functionality achievable with these materials, a bioplastic screw was 3D printed and successfully driven into wood without damage to the screw. Finally, the hydrogel material could be sutured, and the suture could be placed under mechanical load without signs of failure.

4.2 INTRODUCTION

The growing use of plastics and rapid accumulation of plastic waste calls for the development of alternative materials that are promptly degradable and environmentally benign.[1–3] Proteins represent a class of biopolymers with remarkable structural and functional diversity. Utilizing proteins for commercial materials applications can reduce our reliance on petroleum-based materials, as protein feedstocks can be obtained in high volumes from microbial, plant, and animal sources.[4–6] Silk fibroin, collagen, gelatin, and bovine serum albumin (BSA) are examples of proteins and protein derivatives that have thus far been investigated for materials applications. These materials have ranged from commodity materials to specialized biomedical materials. Protein-based materials can generally be processed via solvent casting, melt extrusion, and injection molding,[7] however, their application is often restricted by poor processability into 3D form factors and poor mechanical performance.[8]

Vat photopolymerization[9,10] 3D printing techniques such as stereolithography (SLA), digital light processing (DLP), continuous liquid interface production (CLIP),[11] and high-area rapid printing (HARP)[12] have emerged as promising techniques that offer high quality parts at increasingly fast production rates.[13] The list of 3D printable elastomers, plastics, and composites reported in the literature continues to grow; however, most of these materials are not biodegradable, and only a few are based on biopolymers.[14–18] The design of photocurable resins for vat photopolymerization requires photo-crosslinkable molecules with a low intrinsic viscosities

and fast photocuring rates. In general, a low resin viscosity (0.25 Pa·s to 10 Pa·s)[9,19,20] is necessary to facilitate resin reflow and minimize the undesirable stresses exerted on the printed object during the printing process.

Generally, design of new oligomers and polymers for vat photopolymerization is limited[21–23] by the viscosity of the final resin formulation. Increasing polymer concentration in the resin increases viscosity, as does increasing the molecular weights of the polymeric components, as predicted by Mark-Houwink equation.[24] An alternative design strategy is to employ synthetic polymers with cyclic, branched, or dendritic architectures, or cross-linked unimolecular particles. These architectures are characterized by low intrinsic viscosities relative to that of a linear polymer counterpart.[25–28] Interestingly, the majority of photocurable protein derivatives that have thus far been reported are based on structural proteins (e.g., gelatin and silk fibroin),[17,18] which form fibrous assemblies. Use of these anisotropic structures is counterproductive in vat photopolymerization processes, as this substantially increases the resin viscosity, which can limit processability.

BSA is a globular protein that is well suited for vat photopolymerization 3D printing. At around neutral pH, BSA is highly aqueous soluble (up to 50 wt %) largely due to its high surface charge. Additionally, BSA has a low intrinsic viscosity, which is related to its compact structure. Together, the high solubility and low intrinsic viscosity of BSA facilitate high BSA loading into resins as well as facile processing of BSA-based resins. Methacrylated BSA (MABSA) was synthesized by functionalizing available surface lysines of BSA. This photo-crosslinkable derivative of BSA was used to prepare resins for vat photopolymerization 3D printing using a commercially available Form 2 SLA 3D printer. While a mechanically stiff (6 MPa) hydrogel was previously reported,[29] the applicability of this material for a broader array of load-bearing

applications was limited by its swelling in water, which reduced its mechanical strength.[30,31] Additionally, while the printed constructs primarily consisted of cross-linked MABSA, the presence of some cross-linked poly(ethylene glycol) diacrylate (PEGDA) in the network precluded complete degradation of the material. However, without the PEGDA present as a co-monomer in the resin, the photocuring rate was insufficient for SLA 3D printing.

Tannic acid (TA) is a plant-sourced polyphenol that can be used as an additive to enhance the mechanical properties of synthetic and biopolymer hydrogels.[30,32–40] TA can introduce secondary crosslinks within polymeric networks through hydrogen bonding and hydrophobic interactions[41–43] to enhance the elastic modulus, strength, and toughness of a hydrogel. Additionally, the noncovalent interactions with TA can reduce the extent of swelling of a polymer network and provide sacrificial bonds as an energy dissipation mechanism that improves mechanical toughness.

Herein, we present a process for fabricating biodegradable 3D constructs from a MABSA-TA composite material, which can be used either as a tough hydrogel or dehydrated bioplastic. We developed resin formulations for SLA 3D printing that comprised MABSA and water-soluble acrylate monomers. The mechanical properties of these as-printed hydrogel constructs could be enhanced with the incorporation of TA into the crosslinked MABSA network. MABSA-TA composite hydrogels had greater toughness than as-printed counterparts; this was afforded by the incorporation of the secondary noncovalent crosslinks introduced by TA. In a subsequent step, MABSA-TA composites were thermally treated at 120 °C to unfold α-helical regions and concomitantly form β-sheet structures,[44,45] thereby enhancing mechanical properties. We refer to thermally denatured MABSA-TA (dMABSA-TA) composites as bioplastics. The presence of TA in these bioplastics enhanced mechanical properties and contributed to preventing rehydration of

these materials when immersed in water. The improvements in ultimate strength, elastic modulus, and toughness for these protein-based 3D printed materials enabled 3D printed constructs that were mechanically functional, such as a screw and suturable constructs.

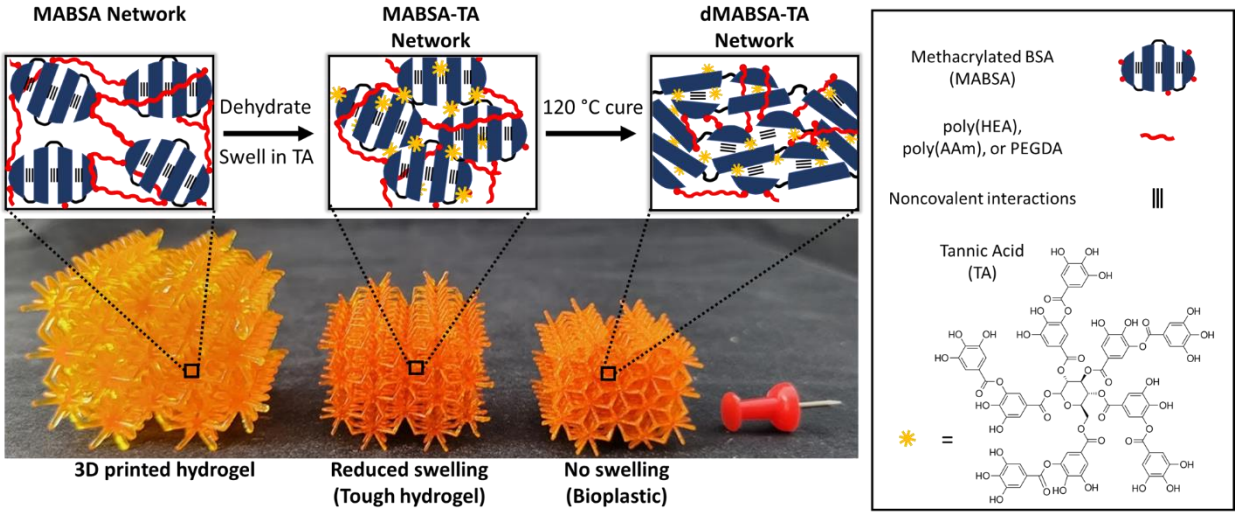

Figure 4. 1 SLA 3D printed MABSA lattice structure. Swelling in water of the as-printed hydrogels was controlled by incubation in TA solution. This TA treatment formed a tough MABSA-TA hydrogel. An additional 120 °C thermal cure denatured the MABSA and virtually eliminated rehydration, forming a dMABSA-TA bioplastic.

4.3 Results and Discussion

Formulation and printability of MABSA-based resins. The MABSA-based resin formulations for SLA 3D printing reported previously[29] afford printed constructs that only partially degraded in the presence of protease and became mechanically weaker upon swelling in water. We hypothesized that the presence of PEGDA as a non-degradable reactive co-monomer (10 wt% of the resin) in these formulations limited the ability of protease to digest the protein

network, as the construct only degraded 22% in a concentrated solution of proteinase K. While the enzyme could degrade protein that was accessible, the presence of the PEGDA cross-linked network physically prevented further access (Table C10). In this work, we show that replacing PEGDA with monofunctional co-monomers that can only form linear chains affords 3D matrices that can be fully degraded, and the addition of TA as an additive to the printed constructs gives hydrogels and bioplastics that can retain their toughness in the presence of water.

We investigated three co-monomers as additives to the MABSA-based resin formulation: AAm, HEA, and PEGDA. All of the resin formulations investigated comprised 30 wt% MABSA, with 0.075 wt% $Ru(bpy)_3Cl_2$ and 0.24 wt% SPS as the photoinitiating system. The minimum quantity of co-monomer additive required to produce a printable resin was determined by printing cylinders using a Form 2 printer with 1–10 wt% of co-monomer. We observed that resin formulations with < 3 wt% AAm, < 2 wt% HEA, or < 5 wt% PEGDA showed insufficient photocuring rates, which resulted in delamination between layers and failed prints (Figure C3). At equal or greater values than these respective concentrations of co-monomer, we consistently obtained successful prints. These minimum concentrations of co-monomer (3 wt% AAm, 2 wt% HEA, and 5 wt% PEGDA) were used in all subsequent experiments.

MABSA-TA interactions. For each of the formulations, we investigated post-print processing of the printed constructs with TA to increase toughness of the materials. The as-printed constructs were immersed in a solution of 300 mg/mL TA for 72 h to infuse TA into the polymer matrix to afford MABSA-TA composite hydrogels. We hypothesized that the incorporation of noncovalent interactions (primarily hydrogen bonding) between MABSA and TA would improve the toughness of these materials by providing a mechanism for energy dissipation. FTIR spectra of the MABSA-TA network hydrogel showed that the TA carbonyl vibration increased from 1700

to 1721 cm^{-1}, confirming the formation of hydrogen bonds between TA and the printed MABSA structures (Figure C4). Gravimetric analysis of the samples showed that the masses of the dehydrated TA composites were higher than those before TA infusion. We determined that the MABSA-TA composite hydrogels contained up to 25 wt% TA relative to the total dry mass (Table C1).

Effect of post-print treatments on mechanical properties. The mechanical properties of the cured materials (ultimate strength, toughness, and elastic modulus) were studied in compression using a load frame. Among the non-treated hydrogels, MABSA-AAm had the highest Young's modulus (2.02 MPa), which was ~ 3 times higher than MABSA-HEA (0.64 MPa) and MABSA-PEGDA (0.68 MPa), respectively (Figure 4.3d). Similarly, MABSA-AAm demonstrated the highest ultimate strength and toughness (Figure 4.3e,f). These results are likely due to the additional hydrogen bonding interactions between the acrylamide groups and MABSA. The TA treatment afforded higher ultimate strength and toughness for all formulations. When compared to the non-treated samples, the ultimate strength increased 27-fold for MABSA-HEA-TA, 3.4-fold for MABSA-AAm-TA, and 15-fold for MABSA-PEGDA-TA. These improvements are attributed to energy dissipation mechanisms associated with the disruption of hydrogen bonding and other noncovalent interactions.[39,47–49] This phenomenon also decreased the water uptake, which can also improve the mechanical properties of hydrogels. Finally, the samples that were thermally cured at 120 °C after the TA treatment exhibited the greatest improvements in mechanical properties. The ultimate strength increased to 7.1 MPa for dMABSA-HEA-TA, 3.2 MPa for dMABSA-AAm-TA, and 3.8 MPa for dMABSA-PEGDA-TA. These increases in mechanical strength were also accompanied by significant reductions in water uptake. Thus, the post-print TA

treatment followed by thermal cure transforms the as-printed hydrogels into bioplastic materials (which show minimal rehydration in water).

The combined TA-treated and 120 °C cured samples exhibited excellent mechanical properties. The TA reinforces the protein-composite matrix via hydrogen-bonding interactions. Additionally, the thermal denaturation of the MABSA results in increased hydrogen-bonding interactions between neighboring protein chains. To demonstrate the high mechanical strength, a screw was 3D printed and treated with TA followed by a 120 °C thermal cure. The screw was mechanically functional and was successfully driven into a piece of wood without any visible structural damage to the screw (Figure 4.3h).

Biodegradation. All of the resin compositions afforded biodegradable materials with degradation rates that depended upon the material composition and post-print processing conditions. The biodegradability of these materials was investigated over the course of 30 d in pepsin solution (pH 1.5–2.0). Without any post-print treatment, the samples degraded 46.0%, 61.2%, and 59.9% for MABSA-HEA, MABSA-AAm, and MABSA-PEGDA, respectively. Regardless of co-monomer used, the samples with TA treatment lost the most mass, 75.3% for MABSA-HEA-TA, 67.5% for MABSA-AAm-TA, and 85.0% for MABSA-PEGDA-TA. This increase in degradation could be the result of disruption of TA-protein interactions under low pH, leading to release of TA from the construct.[50] Additionally, polyphenols have been shown to enhance the enzymatic activity of pepsin.[51] Samples that were treated with TA and 120 °C exhibited the lowest degradation rates. This is likely due to the low water uptake, which could limit pepsin transport into the material, thus limiting degradation.

Suturing. To further demonstrate the excellent mechanical functionality of these MABSA-based hydrogels, we explored the response of the materials to suturing. The MABSA-based hydrogels without post-print treatments were brittle and exhibited crack propagation throughout the material upon suture insertion, as shown in Figure 4.5a. Interestingly, after TA treatment, a 3 mm thick sample exhibited markedly reduced crack propagation (Figure 4.5b) and could support 500 g loaded on a single loop of suture material (Figure 4.5c).

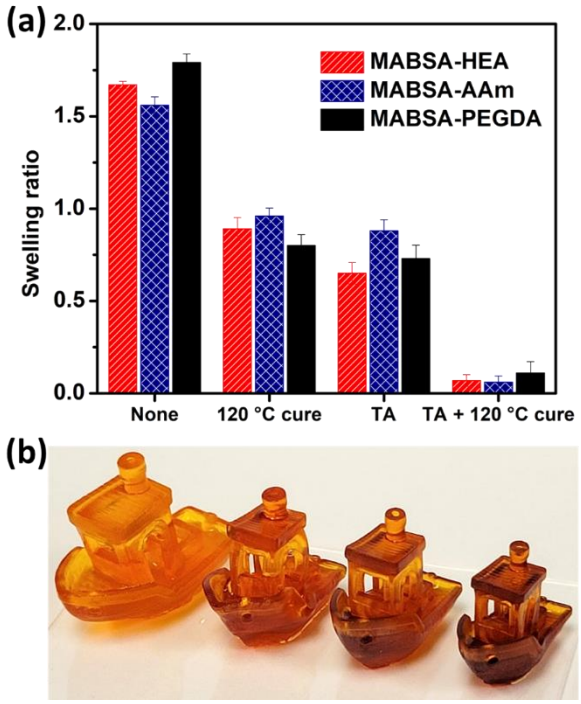

Figure 4. 2 (a) Swelling ratio of 3D printed MABSA-based formulations after each post-print treatment including no treatment, 120 °C thermal cure, TA treatment, and TA treatment and 120 °C thermal cure; (b) Image of printed MABSA-HEA at equilibrium swelling in DI water after each post-print treatment: none, 120 °C thermal cure, TA treatment, and TA treatment and thermal cure (from left to right).

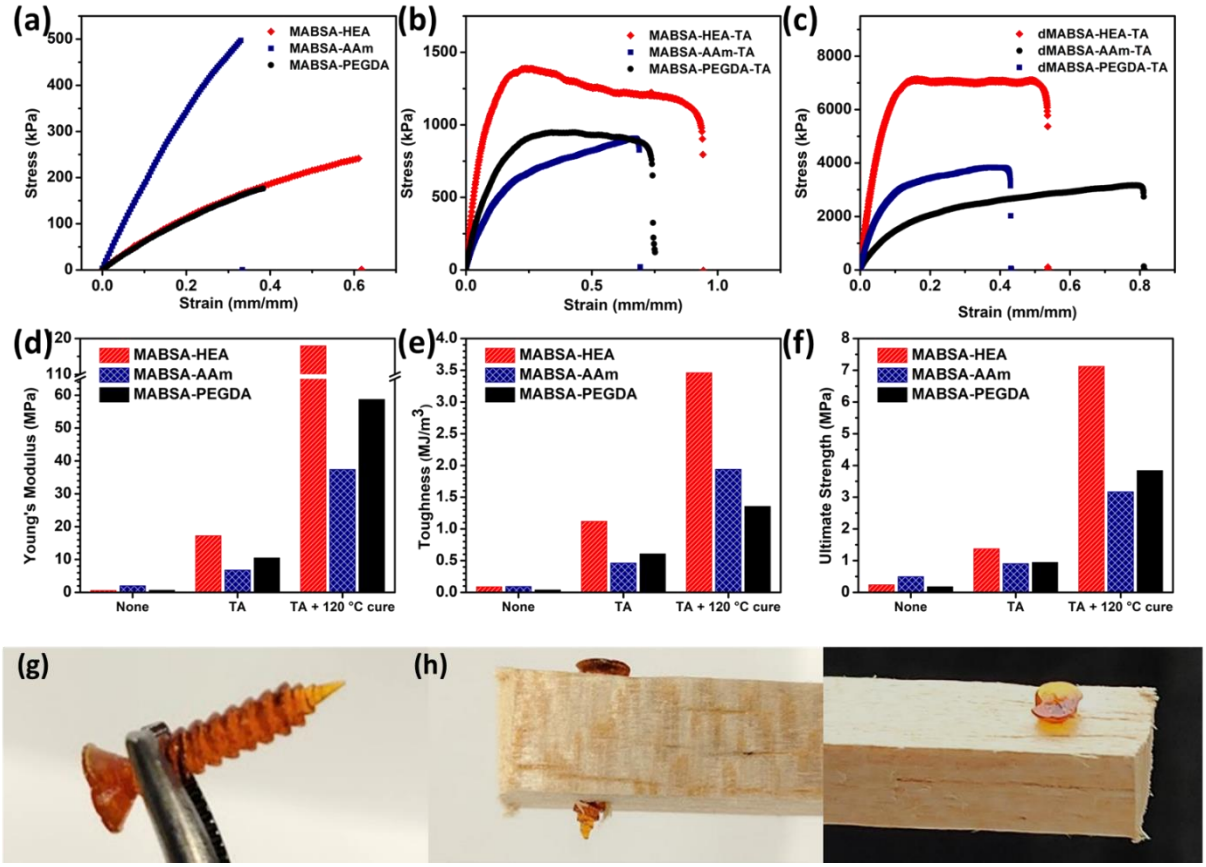

Figure 4. 3 Tensile stress-strain curves of all formulations at equilibrium swelling (a) with no post-print treatment, (b) after TA treatment, (c) after TA treatment and 120 °C thermal cure. (d) Young's modulus, (e) toughness, and (f) Ultimate strength of each formulation with no post-print treatment, 120 °C thermal cure, TA treatment, and both TA treatment and 120 °C thermal cure. (g) 3D printed bioplastic screw after TA treatment and 120 °C thermal cure. (h) Bioplastic screw driven through wood.

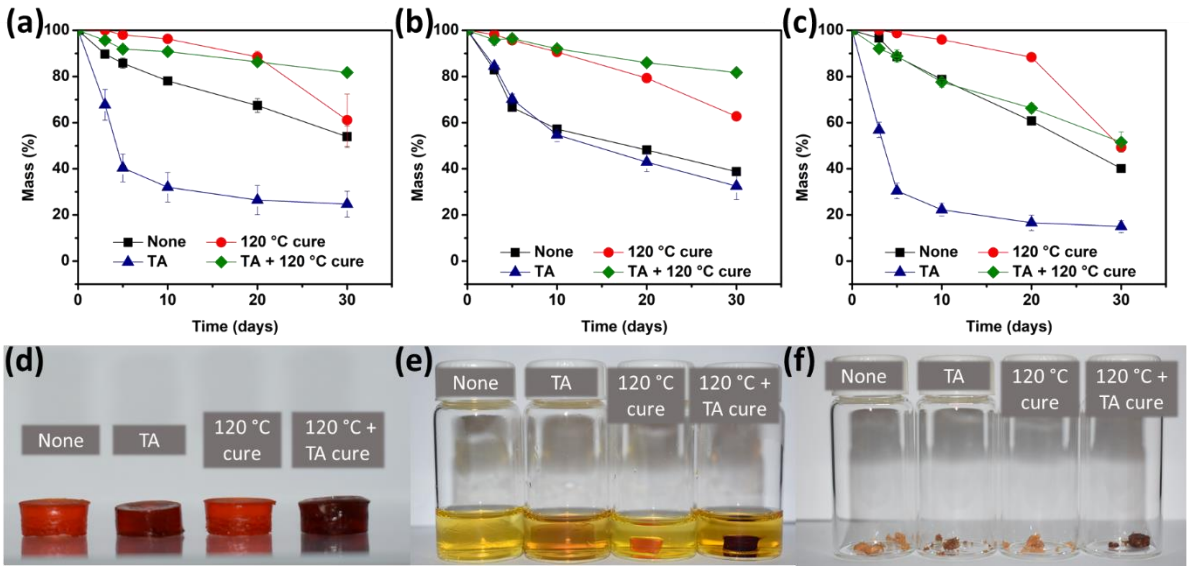

Figure 4. 4 Degradation of printed constructs over 30 d in pepsin solution (a) MABSA-HEA, (b) MABSA-AAm, (c) MABSA-PEGDA. Images of MABSA-HEA, MABSA-HEA-TA, dMABSA-HEA, and dMABSA-HEA-TA at (d) day 0 prior to incubation in pepsin solution, (e) after 5 d incubation in pepsin solution, (f) after 30 d incubation in pepsin solution.

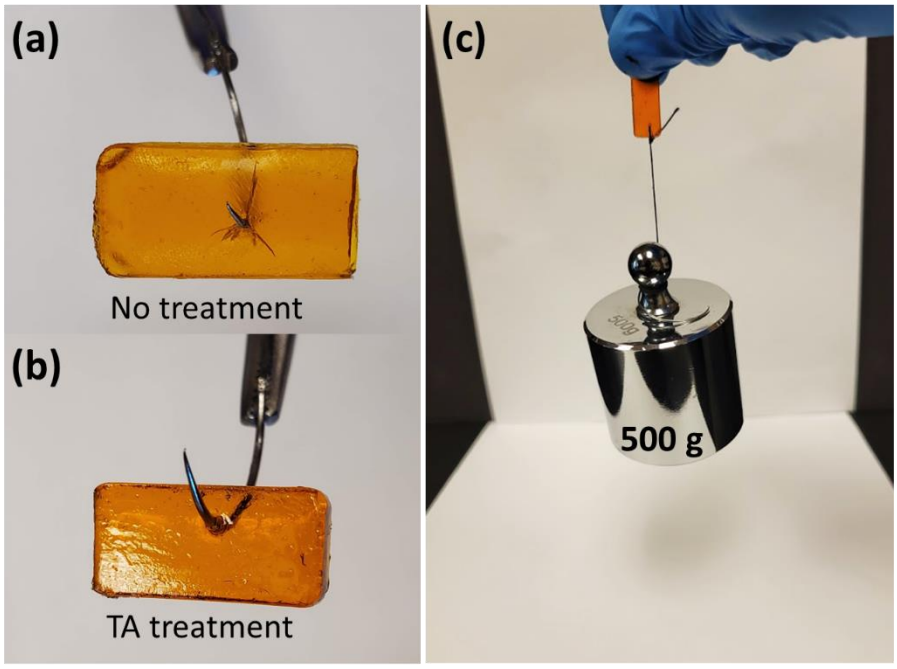

Figure 4. 5 3D printed hydrogel upon insertion of a suture needle (a) with no post-print treatment; MABSA-HEA network and (b) after TA treatment; MABSA-HEA-TA network. (c) MABSA-HEA-TA network hydrogel supporting 500 g weight via a single suture.

4.4 CONCLUSIONS

In summary, we demonstrated a three-step additive manufacturing process to fabricate tough, protein-based hydrogels and bioplastics. In the first step, MABSA was 3D printed via SLA. Then, the printed constructs were treated with TA to introduce additional energy dissipation mechanisms, such as hydrogen bonding, to form tough hydrogels. In the final step, bioplastics were formed by thermally denaturing the protein to form intermolecular β-sheets, thus reducing the rehydration of the printed construct. The TA-treated hydrogels degraded up to 85% after a 30 day incubation in pepsin solution. The broad range of mechanical properties and ability to support a suture enables opportunities to generate biomaterials for applications such as biomedical devices.

4.5 EXPERIMENTAL

4.5.1 *Materials*

All materials were purchased from Sigma Aldrich unless otherwise stated. Methacrylic anhydride (94%), Tris(2,2′-bipyridyl)dichlororuthenium(II) hexahydrate ($Ru(bpy)_3Cl_2$) (99.95%), poly(ethylene glycol) diacrylate (M_n 700 Da), poly(ethylene glycol) methyl ether acrylate (M_n 480 Da), tannic acid, 2-hydroxyethyl acrylate, acrylamide, and sodium persulfate (SPS) were used as received. Ultra-pure and ultra-low fatty acid content BSA was purchased from Nova Biologics.

4.5.2 *Methacrylation of BSA*

A previously published method for methacrylation of BSA was used.[29] In short, BSA (20 g, 0.3 mmol) and $NaHCO_3$ / Na_2CO_3 buffer (200 mL, 0.25 M, pH 9.0) were added to a 1000 mL round-bottom flask equipped with a magnetic stir bar. The mixture was stirred at 2–8 °C until the BSA dissolved completely. Then, methacrylic anhydride (4 mL, 27 mmol, ~2.5 eq. per lysine residue) was added dropwise to the BSA solution over 10 min. The reaction mixture was stirred at 2–8 °C for 2 h. The crude product was diluted two-fold with deionized (DI) water and then dialyzed against DI water for 48 h at 2–8 °C. After dialysis, the product was lyophilized (18.3 g obtained, 91.5% yield). The percent functionalization of the available lysines of BSA with methacryloyl functionalities was determined using a 2,4,6-trinitrobenzene sulfonate (TNBS) assay. For the TNBS assay, BSA and MABSA were dissolved in $NaHCO_3$ / Na_2CO_3 buffer at a concentration of 20 µg/mL. A 0.01% (w/v) solution of TNBS (0.25 mL) was added to 0.5 mL of each protein solution. The samples were incubated at 37 °C for 2 h. To quench the reaction, 0.25 mL of 10%

SDS and 0.125 mL of 1 M HCl were added to each sample. The absorbance of each solution was measured at 335 nm with a UV/Vis spectrophotometer (Agilent 8453). The percent functionalization was calculated from the measured absorbance values as follows:

$$\%\ functionalization = \frac{Abs_{BSA} - Abs_{MABSA}}{Abs_{BSA}}\ x\ 100$$

4.5.3 *Preparation of MABSA-based resin for vat photopolymerization*

All resin formulations were prepared in amber bottles and covered with aluminum foil to prevent auto-polymerization. Three resin formulations were used in this study, each with 30 wt% MABSA and the minimum amount of co-monomer that afforded a printable resin: 5 wt% for poly(ethylene glycol) diacrylate (PEGDA), 3 wt% for acrylamide (AAm), and 2 wt% for 2-hydroxyethyl acrylate (HEA). The weight percentages are based on the total composition of the resin, including DI water as the solvent. As a representative example, we describe here the preparation 6 g of the resin with 30 wt% MABSA and 5 wt% PEGDA. First, 0.3 g of PEGDA was dissolved in 3.66 mL of DI water; then, 1.8 g of MABSA was slowly added to this solution with gentle mixing until dissolved. Finally, 0.075 wt% $Ru(bpy)_3Cl_2$ was dissolved in 120 µL of DI water, and 0.24 wt% SPS was dissolved in 120 µL of DI water; these solutions were sequentially added to the resin formulation with gentle mixing. The final resin formulation was covered with aluminum foil and stored at 4 °C until use. To prepare the other formulations, similar procedures were followed, changing only the co-monomer and DI water quantity.

4.5.4 *SLA 3D printing of MABSA-based hydrogels*

A Formlabs Form 2 printer with a modified build platform and resin tank was used to fabricate the hydrogel constructs (cite paper). Hydrogel constructs were printed in the Form 2's Open Mode, with a layer height of 100 µm. Upon completion of the print, samples were removed from the build platform, rinsed in DI water to remove uncured resin, and post-cured in a custom photocuring chamber (Quans, 400 nm, 1 mW/cm^2) for 90 min. Some samples were further treated with TA, thermally cured at 120 °C, or treated with both TA and heating.

4.5.5 *Post-print treatments*

4.5.5.1 Tannic acid treatment

TA solutions were prepared by dissolving TA in deionized water at a concentration of 300 mg/mL, with pure DI water included as a control. For the TA treatment, 3D printed MABSA hydrogel constructs were photocured, dehydrated, then immersed in TA solution for 72 h, to produce tough TA-MABSA hydrogel constructs. Free TA was removed by equilibration in DI water. Some samples were then thermally cured at 120 °C to produce virtually non-rehydratable bioplastics.

4.5.5.2 Thermal cure

3D printed MABSA hydrogels with or without TA treatment were photocured, dehydrated then placed in a 120 °C oven for 180 min.

4.5.6 *Measurement of TA content*

3D printed MABSA hydrogel disks (10 mm diameter × 5 mm height) were equilibrated in DI water for 24 h to remove unreacted MABSA and co-monomer. Then, the disks were vacuum dried and weighed (m_i). After immersing the disks in 300 mg/mL TA solution for 72 hours, unbound TA was removed by equilibration in DI water for 24 hours. Finally, the disks were vacuum dried and weighed (m_f). The TA content was calculated as follows:

$$TA\ content = \left(\frac{m_f - m_i}{m_i}\right) \times\ 100\%$$

4.5.7 *Swelling experiments*

3D printed cylindrical disks (10 mm diameter × 5 mm height) were subjected to post-print treatments (either 120 °C thermal cure, TA treatment, 120 °C thermal cure and TA treatment, or no treatment). Disks were then vacuum dried and measured in height and diameter to determine volume (V_i). The disks were then equilibrated in DI water for 24 hours and measured in diameter and height to determine volume (V_f). The swelling ratio was calculated as follows:

$$Swelling\ ratio = \left(\frac{V_f - V_i}{V_i}\right)$$

4.5.8 *Uniaxial compression testing*

Compression tests were performed using an Instron 5585H load frame with a 2 kN load cell. Cylindrical compression test specimens (10 mm diameter × 5 mm height) were 3D printed as described above. Specimens were tested at equilibrium swelling with DI water. All tests were conducted at room temperature (22 °C) using a crosshead rate of 1.3 mm/min until specimen failure or 80% strain. Prior to testing, the hydrated specimens were removed from DI water, blotted dry with a Kimwipe, and the dimensions of the specimens were measured using a digital caliper. At least 5 specimens of each formulation (MABSA-AAm, MABSA-HEA, and MABSA-PEGDA) and post-print treatment (120 °C thermal cure, TA treatment, 120 °C thermal cure and TA treatment, or no treatment) were tested. Compressive modulus and strength were calculated from the resulting stress-strain curves.

4.5.9 *Uniaxial tensile testing*

Tensile mechanical measurements were performed using a TestResources 100 series Universal Test Machine with a 1 kN load cell. ASTM D638 type V specimens were printed and post-print treated as described above. Specimens were tested at equilibrium swelling with DI water. All tests were conducted at room temperature (22 °C) using a crosshead rate of 5 mm/min until specimen failure. Prior to testing, the hydrated specimens were removed from DI water, blotted dry with a Kimwipe, and the dimensions of the specimens were measured using a digital caliper. At least 5 specimens of each formulation (MABSA-AAm, MABSA-HEA, and MABSA-PEGDA) and post-print treatment (120 °C thermal cure, TA treatment, 120 °C thermal cure and TA treatment, or no treatment) were tested. Tensile modulus, tensile strength, and tensile toughness values were calculated from the resulting stress-strain curves. Toughness was calculated as the area under the

stress-strain curve; this was done using a MATLAB program. Compressive modulus was determined from the slope of the elastic region of the stress-strain curve.

4.5.10 *Biodegradation*

The biodegradation profiles of 3D printed constructs were monitored using a pepsin solution to hydrolyze the protein. Biodegradation assays were performed at 37 °C in a shaking incubator at 221 rpm. The incubation medium was prepared by dissolving pepsin (> 2500 U/mg) at 3.2 g/L in 0.1 M HCl (pH 1.5–2.0). DI water and a solution of 0.1 M HCl (pH 1.5–2.0) were used as controls. 4 mL of incubation medium was added to each test structure. Dry mass data were collected on days 3, 5, 10, 20 and 30. Dry mass for each sample was measured after drying the sample under vacuum. The percentage of remaining dry mass was calculated as follows:

$$\%\ \text{remaining dry mass} = \frac{(Dry\ mass\ after\ biodegradation)}{Initial\ dry\ mass} \times 100$$

4.6 REFERENCES

[1] D. K. Schneiderman, M. A. Hillmyer, *Macromolecules* **2017**, *50*, 3733.
[2] R. Geyer, J. R. Jambeck, K. L. Law, *Sci. Adv.* **2017**, *3*, 25.
[3] R. M. O'dea, J. A. Willie, T. H. Epps, *ACS Macro Lett.* **2020**, *9*, 476.
[4] E. Sanchez-Rexach, T. G. Johnston, C. Jehanno, H. Sardon, A. Nelson, *Chem. Mater.* **2020**, *32*, 7105.
[5] S. Pirsa, K. A. Sharifi, *J. Chem. Lett.* **2020**, *1*, 47.
[6] S. A. A. Mohamed, M. El-Sakhawy, M. A. M. El-Sakhawy, *Carbohydr. Polym.* **2020**, *238*, 116178.
[7] V. M. Hernandez-Izquierdo, J. M. Krochta, *J. Food Sci.* **2008**, *73*, R30.
[8] S. Kapoor, S. C. Kundu, *Acta Biomater.* **2016**, *31*, 17.

[9] A. Bagheri, J. Jin, *ACS Appl. Polym. Mater.* **2019**, *1*, 593.
[10] G. A. Appuhamillage, N. Chartrain, V. Meenakshisundaram, K. D. Feller, C. B. Williams, T. E. Long, *Ind. Eng. Chem. Res.* **2019**, *58*, 15109.
[11] J. R. Tumbleston, D. Shirvanyants, N. Ermoshkin, R. Janusziewicz, A. R. Johnson, D. Kelly, K. Chen, R. Pinschmidt, J. P. Rolland, A. Ermoshkin, E. T. Samulski, J. M. DeSimone, *Science (80-.).* **2015**, *347*, 1349.
[12] D. A. Walker, J. L. Hedrick, C. A. Mirkin, *Science (80-.).* **2019**, *366*, 360.
[13] D. M. Zuev, A. K. Nguyen, V. I. Putlyaev, R. J. Narayan, *Bioprinting* **2020**, *20*, e00090.
[14] M. T. Poldervaart, B. Goversen, M. De Ruijter, A. Abbadessa, F. P. W. Melchels, F. C. Öner, W. J. A. Dhert, T. Vermonden, J. Alblas, *PLoS One* **2017**, *12*, 1.
[15] K. S. Lim, B. S. Schon, N. V. Mekhileri, G. C. J. Brown, C. M. Chia, S. Prabakar, G. J. Hooper, T. B. F. Woodfield, *ACS Biomater. Sci. Eng.* **2016**, *2*, 1752.
[16] R. Ding, Y. Du, R. B. Goncalves, L. F. Francis, T. M. Reineke, *Polym. Chem.* **2019**, *10*, 1067.
[17] S. H. Kim, Y. K. Yeon, J. M. Lee, J. R. Chao, Y. J. Lee, Y. B. Seo, M. T. Sultan, O. J. Lee, J. S. Lee, S. Il Yoon, I. S. Hong, G. Khang, S. J. Lee, J. J. Yoo, C. H. Park, *Nat. Commun.* **2018**, *9*, 1620.
[18] M. D. Castilho, J. Malda, R. Levato, C. R. Alcala-Orozco, F. P. W. Melchels, D. Gawlitta, G. J. Hooper, T. B. F. Woodfield, P. F. Costa, K. S. Lim, K. M. A. van Dorenmalen, *Biofabrication* **2018**, *10*, 034101.
[19] S. Schüller-Ravoo, S. M. Teixeira, J. Feijen, D. W. Grijpma, A. A. Poot, *Macromol. Biosci.* **2013**, *13*, 1711.
[20] L. Elomaa, S. Teixeira, R. Hakala, H. Korhonen, D. W. Grijpma, J. V. Seppälä, *Acta Biomater.* **2011**, *7*, 3850.
[21] C. Hinczewski, S. Corbel, T. Chartier, *J. Eur. Ceram. Soc.* **1998**, *18*, 583.
[22] J. T. Sutton, K. Rajan, D. P. Harper, S. C. Chmely, *ACS Appl. Mater. Interfaces* **2018**, *10*, 36456.
[23] Y. Luo, G. Le Fer, D. Dean, M. L. Becker, *Biomacromolecules* **2019**, *20*, 1699.
[24] P. C. Hiemenz, T. Lodge, *Polymer Chemistry*, CRC Press, **2007**.
[25] M. Seiler, *Fluid Phase Equilib.* **2006**, *241*, 155.
[26] B. I. Voit, A. Lederer, *Chem. Rev.* **2009**, *109*, 5924.
[27] G. Le Fer, Y. Luo, M. L. Becker, *Polym. Chem.* **2019**, *10*, 4655.
[28] T. E. L. Ryan J. Mondschein, Akanksha Kanitkar, Christopher B. Williamsb,Scott S. Verbridge, *Biomaterials* **2017**, *140*, 170.
[29] P. T. Smith, B. Narupai, J. H. Tsui, S. C. Millik, R. T. Shafranek, D.-H. Kim, A. Nelson, *Biomacromolecules* **2020**, *21*, DOI 10.1021/acs.biomac.9b01236.
[30] T. Nonoyama, J. P. Gong, *Annu. Rev. Chem. Biomol. Eng.* **2021**, *12*, 393.
[31] N. Johari, L. Moroni, A. Samadikuchaksaraei, *Eur. Polym. J.* **2020**, *134*, 109842.
[32] X. Zhao, X. Chen, H. Yuk, S. Lin, X. Liu, G. Parada, *Chem. Rev.* **2021**, *121*, 4309.
[33] C. W. Peak, J. J. Wilker, G. Schmidt, *Colloid Polym. Sci.* **2013**, *291*, 2031.
[34] X. Zhou, C. Li, L. Zhu, X. Zhou, *Chem. Commun.* **2020**, *56*, 13731.
[35] C. Zhang, Z. Liu, Z. Shi, T. Li, H. Xu, X. Ma, J. Yin, M. Tian, *Polym. Chem.* **2017**, *8*, 1824.
[36] W. Sun, B. Xue, Q. Fan, R. Tao, C. Wang, X. Wang, Y. Li, M. Qin, W. Wang, B. Chen, Y. Cao, *Sci. Adv.* **2020**, *6*, DOI 10.1126/sciadv.aaz9531.
[37] S. Y. Zheng, H. Ding, J. Qian, J. Yin, Z. L. Wu, Y. Song, Q. Zheng, *Macromolecules*

2016, *49*, 9637.
[38] M. Nakahata, Y. Takashima, A. Harada, *Macromol. Rapid Commun.* **2016**, *37*, 86.
[39] M. A. Gonzalez, J. R. Simon, A. Ghoorchian, Z. Scholl, S. Lin, M. Rubinstein, P. Marszalek, A. Chilkoti, G. P. López, X. Zhao, *Adv. Mater.* **2017**, *29*, 1.
[40] X. Zhao, *Soft Matter* **2014**, *10*, 672.
[41] S. Quideau, D. Deffieux, C. Douat-Casassus, L. Pouységu, *Angew. Chemie - Int. Ed.* **2011**, *50*, 586.
[42] Y. Chen, A. E. Hagerman, *J. Agric. Food Chem.* **2004**, *52*, 4008.
[43] M. Labieniec, T. Gabryelak, *J. Photochem. Photobiol. B Biol.* **2006**, *82*, 72.
[44] R. Lu, W. W. Li, A. Katzir, Y. Raichlin, H. Q. Yu, B. Mizaikoff, *Analyst* **2015**, *140*, 765.
[45] G. Shanmugam, P. L. Polavarapu, *Biophys. Chem.* **2004**, *111*, 73.
[46] E. Sanchez-Rexach, P. T. Smith, A. Gomez-Lopez, M. Fernandez, A. L. Cortajarena, H. Sardon, A. Nelson, *ACS Appl. Mater. Interfaces* **2021**, *13*, 19193.
[47] J. Fang, A. Mehlich, N. Koga, J. Huang, R. Koga, X. Gao, C. Hu, C. Jin, M. Rief, J. Kast, D. Baker, H. Li, *Nat. Commun.* **2013**, *4*, DOI 10.1038/ncomms3974.
[48] L. Zhao, X. Zhang, Q. Luo, C. Hou, J. Xu, J. Liu, *Biomacromolecules* **2020**, *21*, 4212.
[49] M. A. Da Silva, S. Lenton, M. Hughes, D. J. Brockwell, L. Dougan, *Biomacromolecules* **2017**, *18*, 636.
[50] R. Osawa, T. Walsh, *J. Agric. Food Chem* **1993**, *41*, 704.
[51] D. Tagliazucchi, E. Verzelloni, A. Conte, *J. Agric. Food Chem.* **2005**, *53*, 8706.

APPENDIX A

Appendix A accompanies Chapter 2

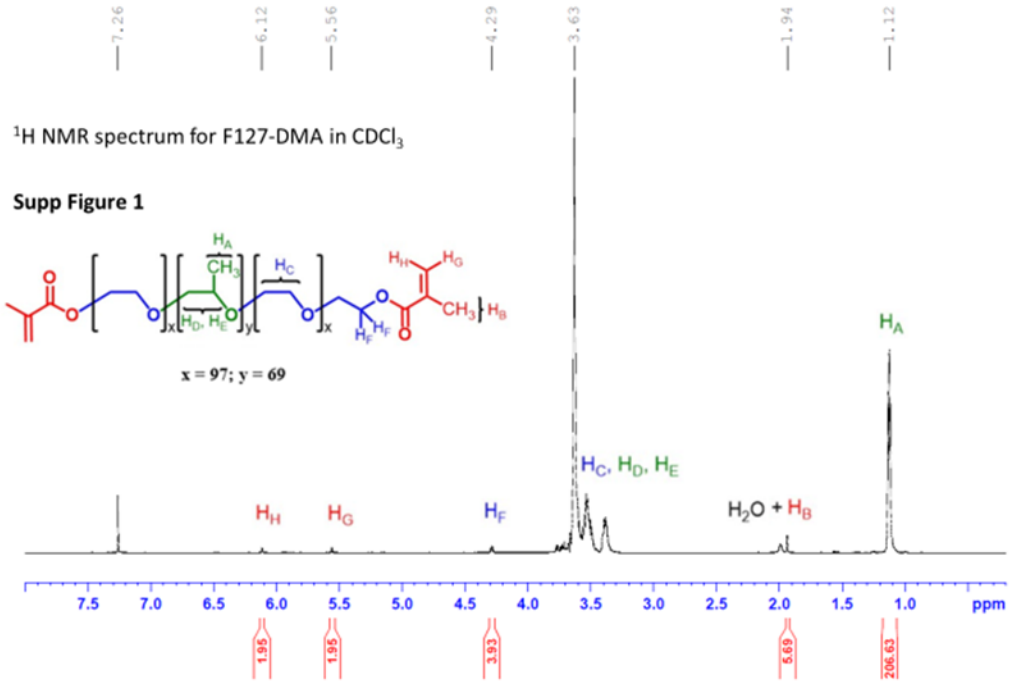

Figure A. 1 ^{1}H NMR spectrum of F127-DMA in $CDCl_3$.

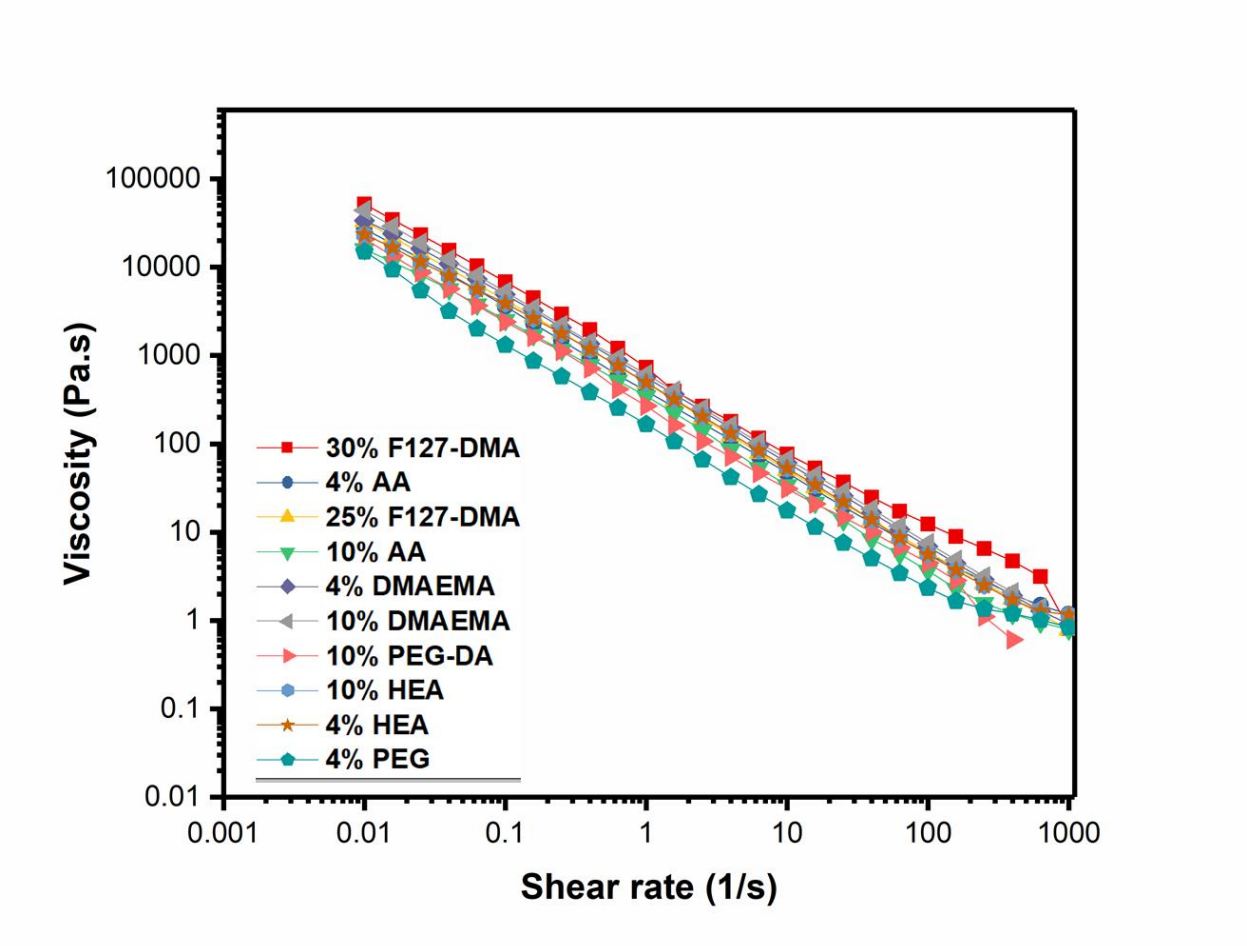

Figure A. 2 Viscosity vs. shear rate plot of hydrogel ink formulations performed at 21 °C.

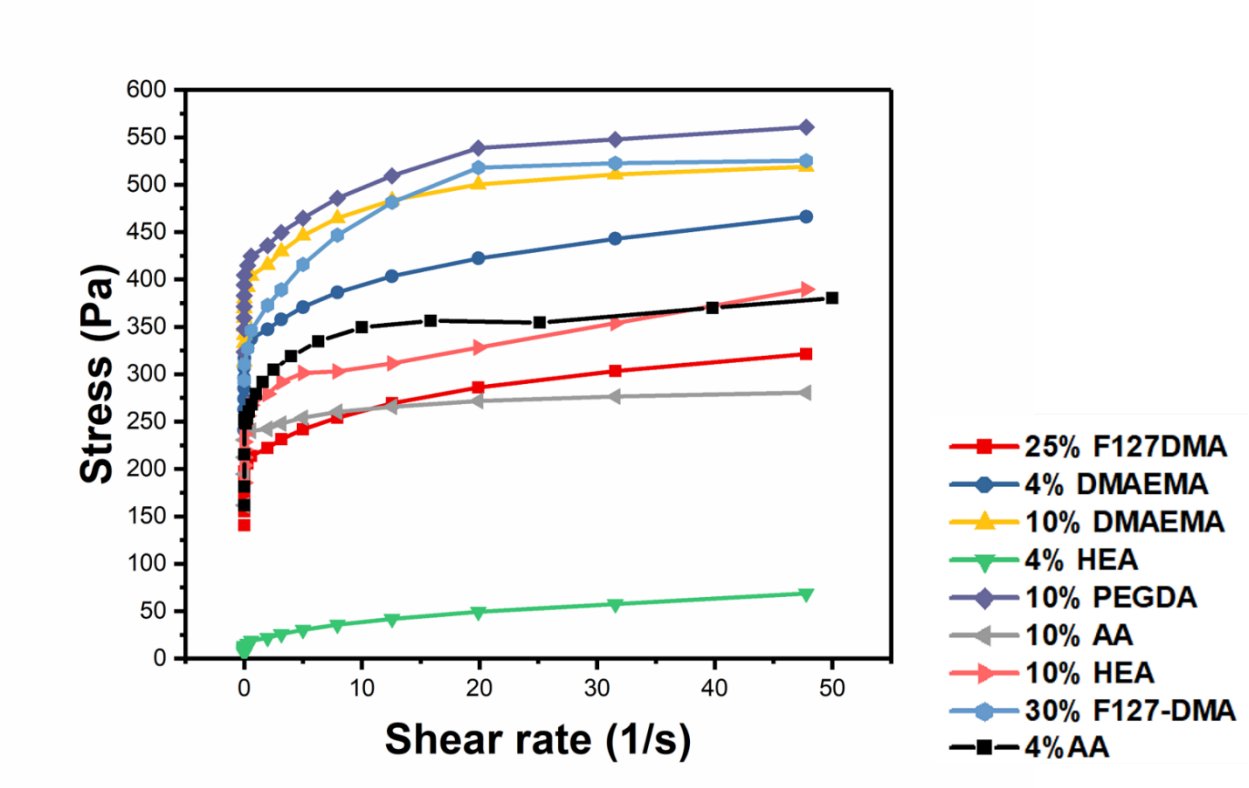

Figure A. 3 Stress versus shear rate plots of hydrogel formulations under increasing shear rates from 0 to 50 S^{-1}, performed at 21 °C.

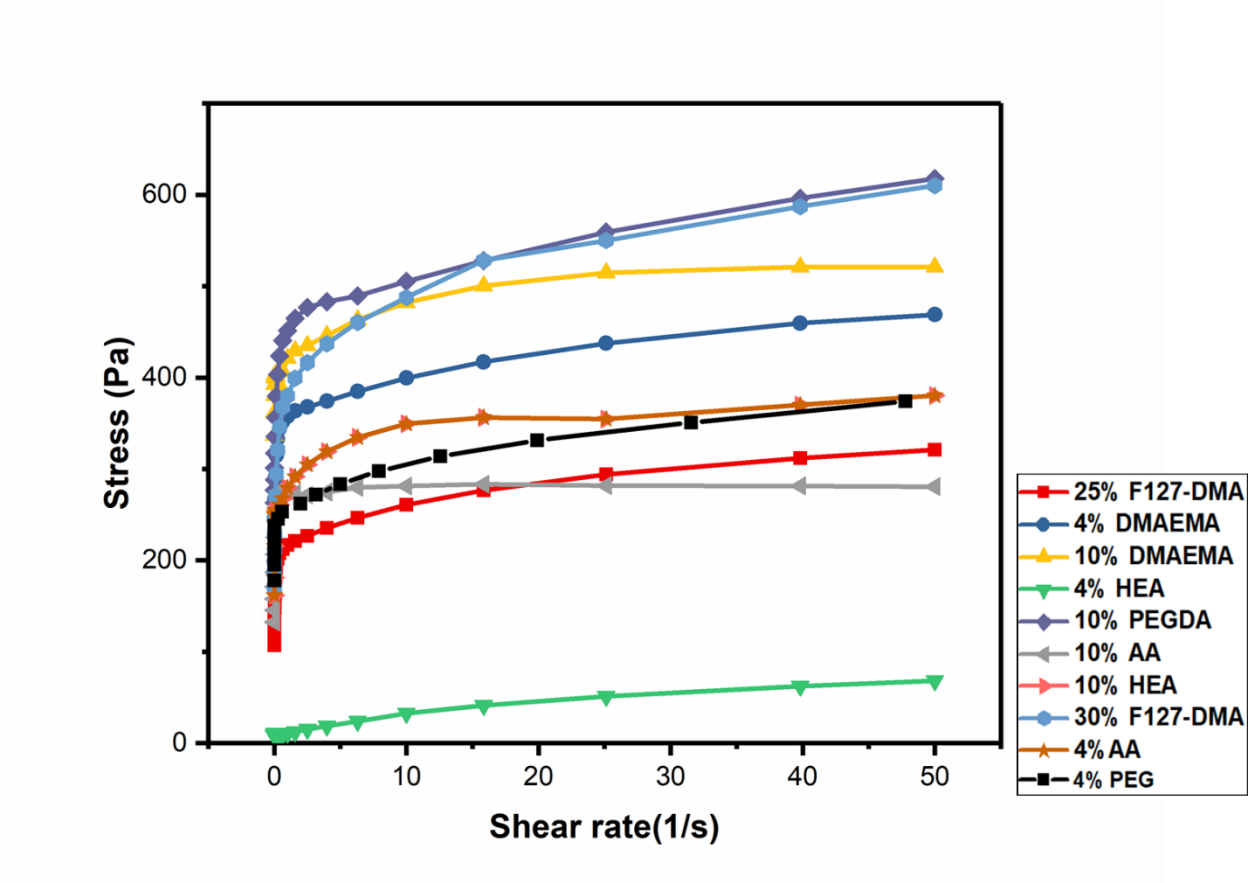

Figure A. 4 Stress versus shear rate plots of hydrogel formulations under decreasing shear rates from 50 to 0 S^{-1}, performed at 21 °C.

Herschel-Bulkley Fit of 30% F127-DMA:

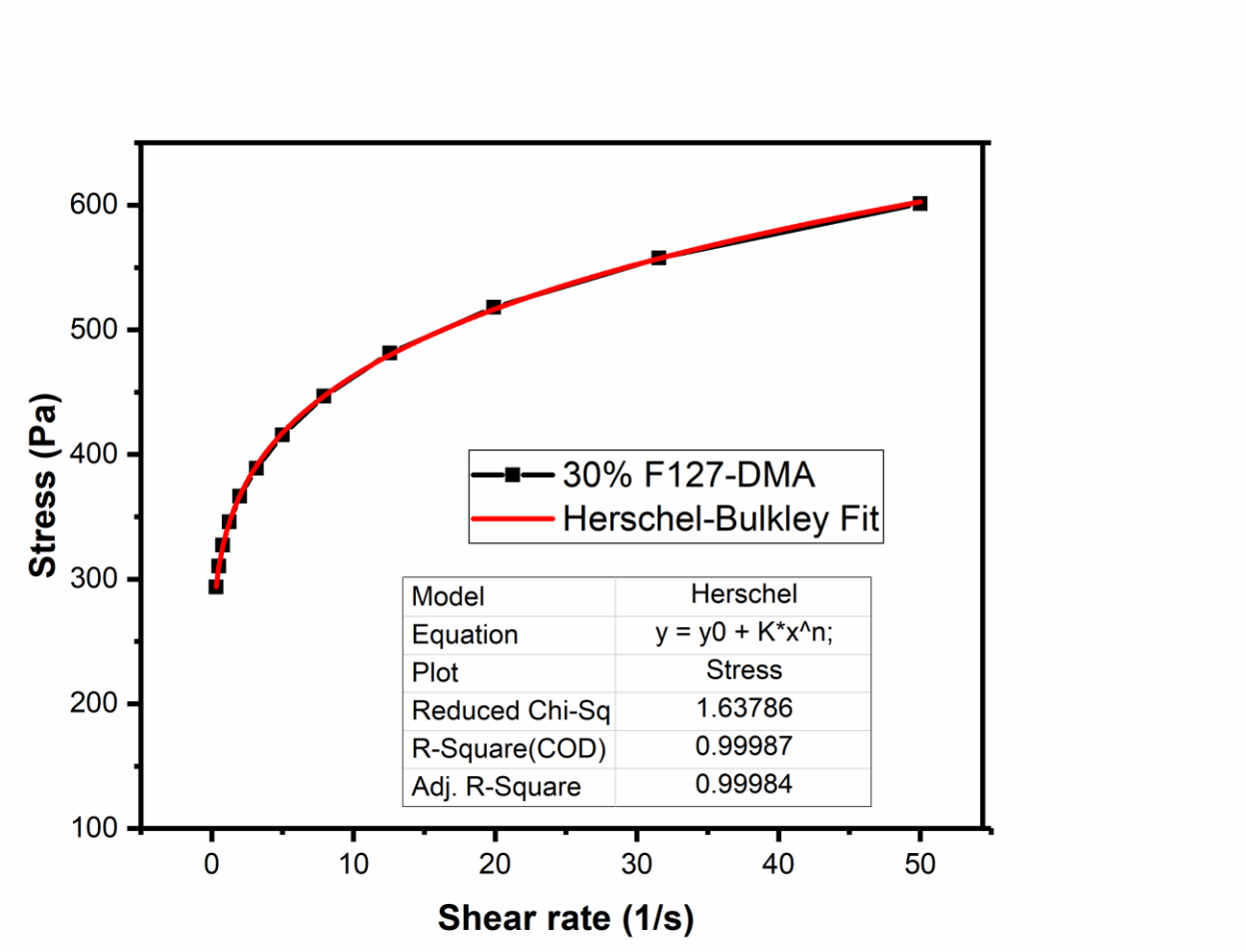

Figure A. 5 Herschel-Bulkley fit of 30 wt % F127-DMA.

Calculation of Viscosity of Hydrogel Inks:

Based on previous work by Chua *et.al*[39]. when the reference shear rate (γ_0) = 1 s^{-1}, the viscosity for Pluronic hydrogels could be determined by using the Power law equation for shear thinning fluids given by:

$$\eta = \eta_0 \dot{\gamma}^{n-1} \qquad (1)$$

Where η and η_0 are the apparent and zero-shear viscosities and $\dot{\gamma}$ is the shear rate. Thus equation (1) can be changed into a logarithmic expression:

$$\text{Log } \eta = (\text{n-1}) \text{ Log } \dot{\gamma} \quad + \text{Log } \eta_o$$

A log-log plot of viscosity versus shear rate for each formulation would enable us to calculate its dynamic viscosity (supplementary information). The value of *n*, the Power Law index appearing in the expression, from the above equation enabled us to calculate the viscosities of the materials using the equation

$$\dot{\gamma} = \frac{(3n+1)*}{4n} 2V/_{D} \qquad (2)$$

Where V is the print speed and D is the nozzle diameter. Thus for 25 % F127-DMA, n= 0.0673, Putting that in equation (2) gives the shear rate as 467 s^{-1}, which corresponds to a viscosity value of 1.486 Pa.S. All the hydrogel ink viscosities were determined this way.

Diffusion tests

For each formulation, three tensile specimens were prepared then cut in half. The resulting six specimens were then subjected to one of two conditions; dried under vacuum immediately after preparation (non-swollen) or immersed in water until reaching equilibrium swelling then dried under vacuum (swollen). The non-swollen samples were massed, dried under vacuum for 48 hours, then massed again. The masses of the swollen samples were recorded prior to swelling, followed by immersion in a large excess of deionized water for 96 hours at 21°C. During the 96-hour immersion, the water was replaced with fresh deionized water every 12 hours. After four days of immersion, the equilibrium swelling masses were recorded, then the specimens were dried under vacuum for 48 hours.

The final dried mass of each specimen was subtracted from its initial mass, then divided by its initial mass to determine the % mass loss after drying. The % mass loss of the swollen samples was compared to the % mass loss of the non- swollen samples to prove that the polymerized additives are covalently bound to the hydrogel network. The swelling ratios are represented as (swollen mass – dried mass) / dried mass.

For the controls, formulations with 4 wt % and 10 wt % poly(acrylic acid) (PAA) were tested. All of the PAA was able to diffuse out of the crosslinked F127-DMA network, as the PAA was not covalently bound to the F127-DMA.

Additive (wt%)	Swelling Ratio	% Water in Formulation	% Mass Loss (non-swollen)	% Mass Loss (swollen)
--	6.14 ± 0.04	75	70.50 ± 0.7	73.24 ± 1.3
AA (4)	4.91 ± 0.01	71	67.78 ± 1.0	70.98 ± 0.2
HEA (4)	6.55 ± 0.02	71	68.10 ± 0.8	69.23 ± 0.2
DMAEMA (4)	10.28 ± 0.04	71	71.52 ± 0.3	74.54 ± 0.2
PEG-DA (4)	5.13 ± 0.01	71	64.58 ± 1.3	68.31 ± 0.2
PAA (4)	4.95 ± 0.04	71	68.90 ± 1.0	73.00 ± 0.3
AA (10)	3.00 ± 0.00	65	59.90 ± 0.4	61.45 ± 2.1
HEA (10)	5.92 ± 0.01	65	56.67 ± 2.0	58.49 ± 1.4
DMAEMA (10)	9.79 ± 0.06	65	62.19 ± 0.3	65.57 ± 3.2
PEG-DA (10)	3.59 ± 0.02	65	62.46 ± 1.1	62.61 ± 1.0
PAA (10)	4.57 ± 0.01	65	61.62 ± 0.2	70.97 ± 0.2

Table A. 1 Summary of swelling ratio and diffusion tests of 25wt% F127-DMA formulations in deionized water. N = 3

Polymer (wt %)	Additive (wt %)	Wt % of water (wt %)	Photo-initiator (wt%)
F127-DMA (25)	--	75	0.1
F127-DMA (30)	--	70	0.1
F127-DMA (25)	AA (4)	71	0.1
F127-DMA (25)	AA (10)	65	0.1
F127-DMA (25)	HEA (4)	71	0.1
F127-DMA (25)	HEA (10)	65	0.1
F127-DMA (25)	DMAEMA (4)	71	0.1
F127-DMA (25)	DMAEMA (10)	65	0.1
F127-DMA (25)	PEG-DA (4)	71	0.1
F127-DMA (25)	PEG-DA (6)	69	0.1
F127-DMA (25)	PEG-DA (10)	65	0.1

Table A. 2 Summary of the hydrogel ink compositions used in this study.

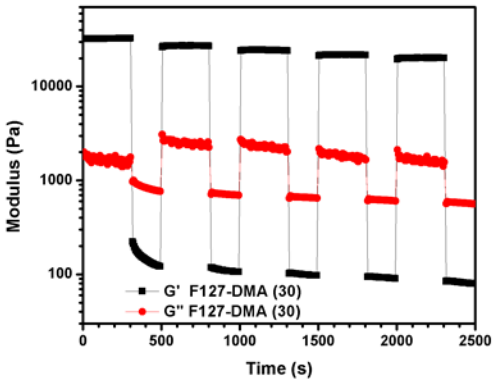
G' F127-DMA (30)
G'' F127-DMA (30)
Modulus (Pa)
Time (s)

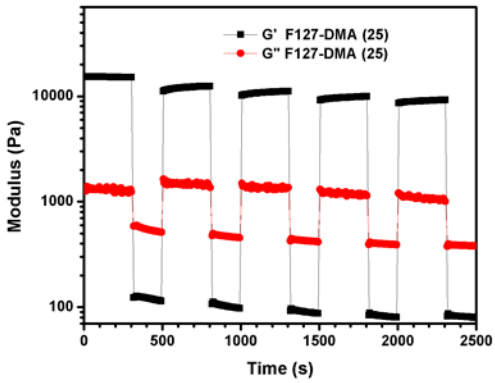
G' F127-DMA (25)
G'' F127-DMA (25)
Modulus (Pa)
Time (s)

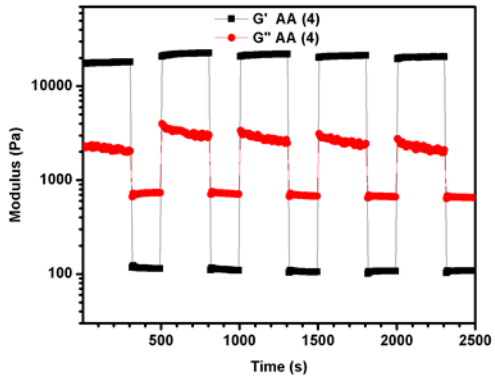
G' AA (4)
G'' AA (4)
Modulus (Pa)
Time (s)

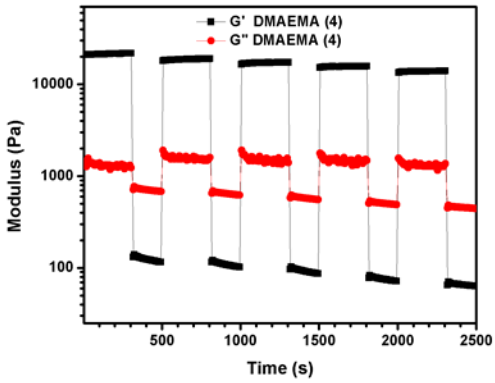
G' DMAEMA (4)
G'' DMAEMA (4)
Modulus (Pa)
Time (s)

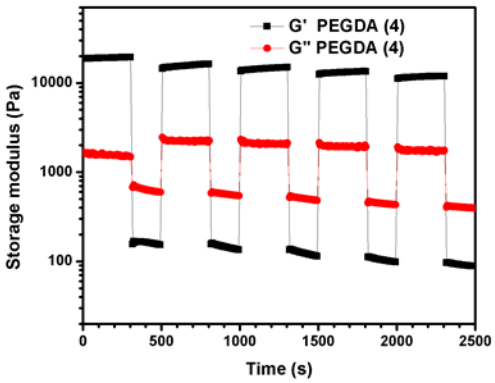
G' PEGDA (4)
G'' PEGDA (4)
Storage modulus (Pa)
Time (s)

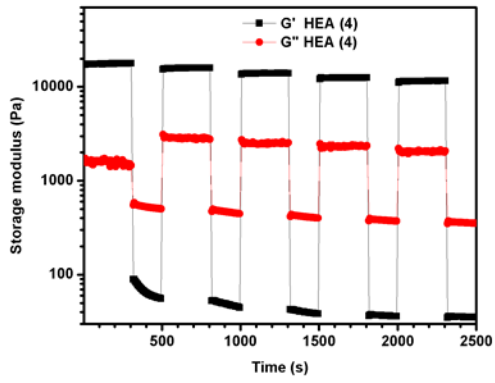
G' HEA (4)
G'' HEA (4)
Storage modulus (Pa)
Time (s)

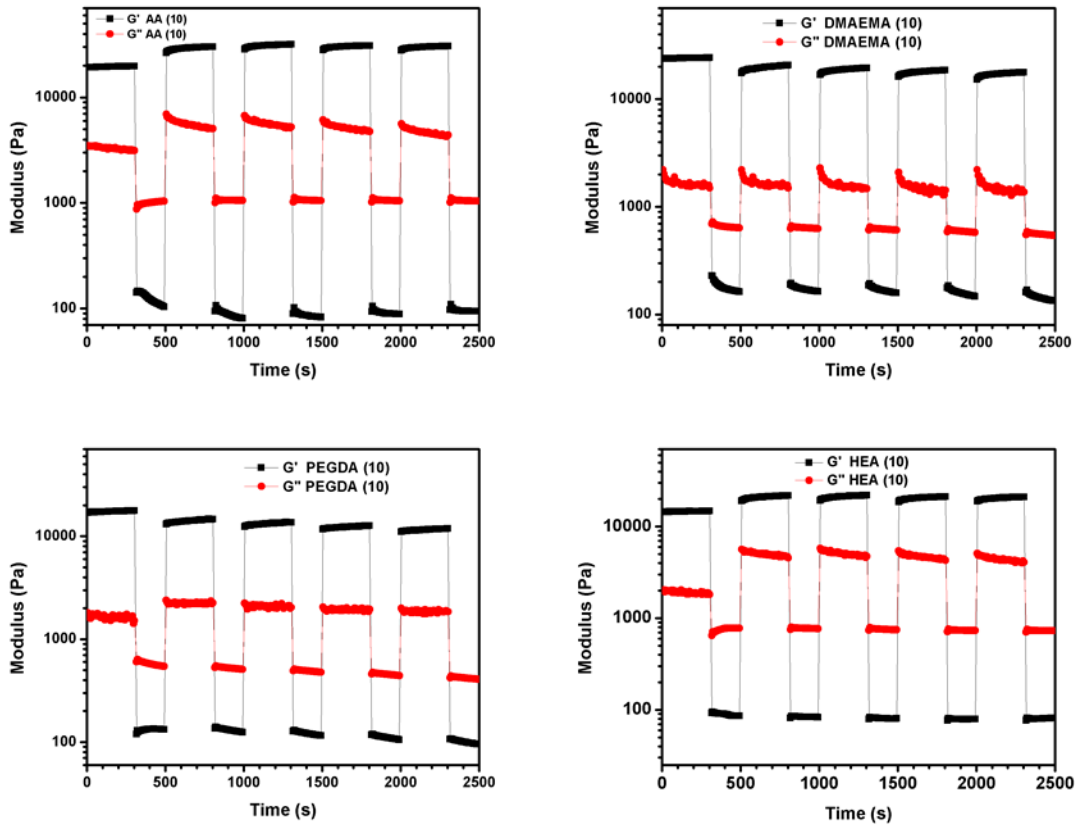

Figure A. 6 Cyclic shear strain experiment for the hydrogel ink formulations.
Cycling between 5 min periods of low strain (1 %) and 3 min periods of high strain (100 %) performed at 25 ° C.

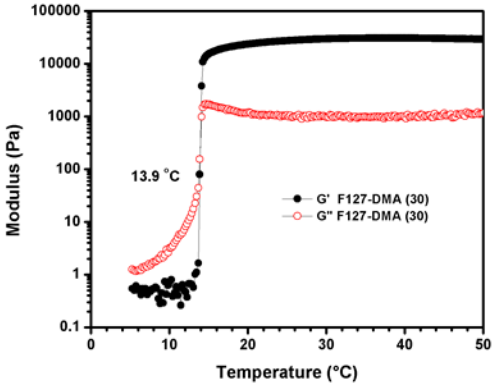
Modulus (Pa)
Temperature (°C)
13.9 °C
G' F127-DMA (30)
G" F127-DMA (30)

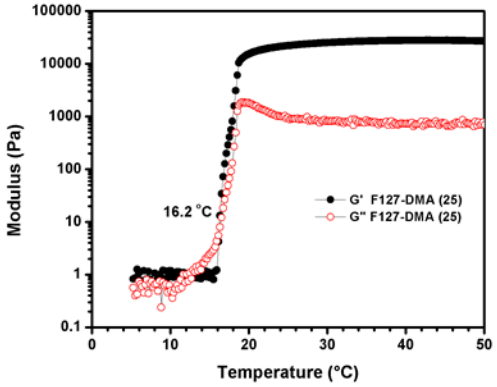
Modulus (Pa)
Temperature (°C)
16.2 °C
G' F127-DMA (25)
G" F127-DMA (25)

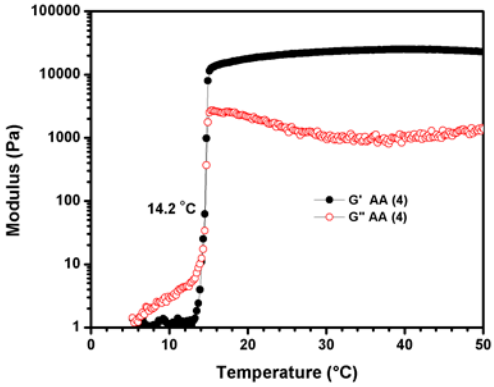
Modulus (Pa)
Temperature (°C)
14.2 °C
G' AA (4)
G" AA (4)

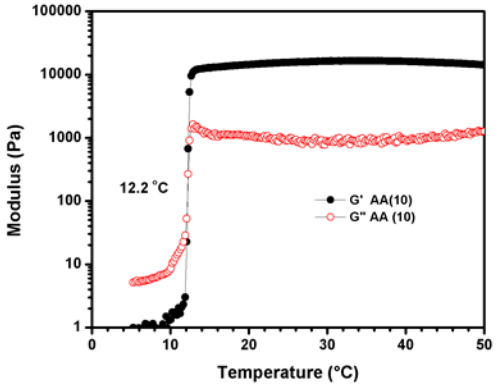
Modulus (Pa)
Temperature (°C)
12.2 °C
G' AA(10)
G" AA (10)

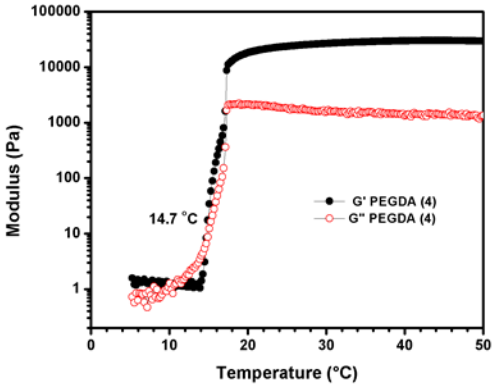
Modulus (Pa)
Temperature (°C)
14.7 °C
G' PEGDA (4)
G" PEGDA (4)

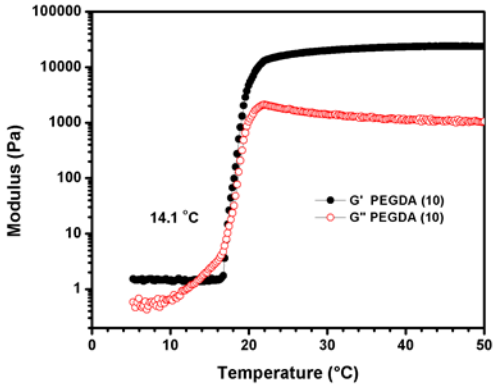
Modulus (Pa)
Temperature (°C)
14.1 °C
G' PEGDA (10)
G" PEGDA (10)

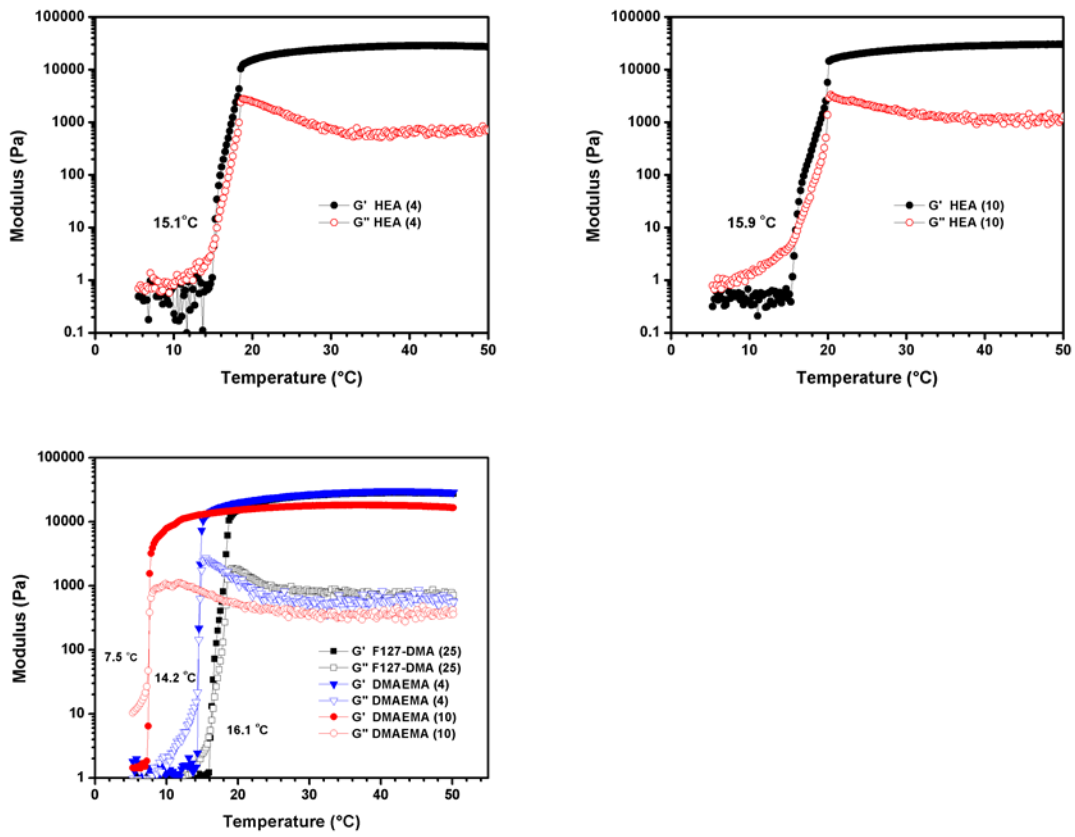

Figure A. 7 Temperature ramp experiments

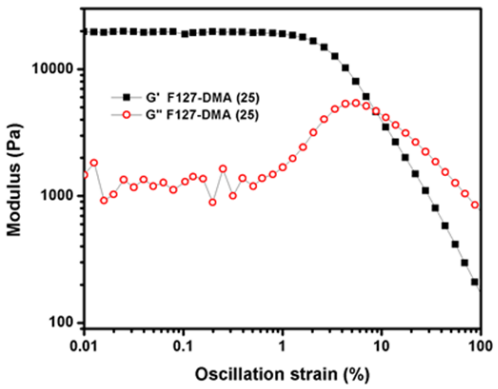
G' F127-DMA (25)
G" F127-DMA (25)
Modulus (Pa)
Oscillation strain (%)

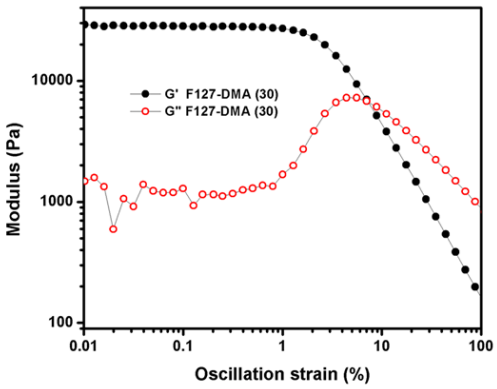
G' F127-DMA (30)
G" F127-DMA (30)
Modulus (Pa)
Oscillation strain (%)

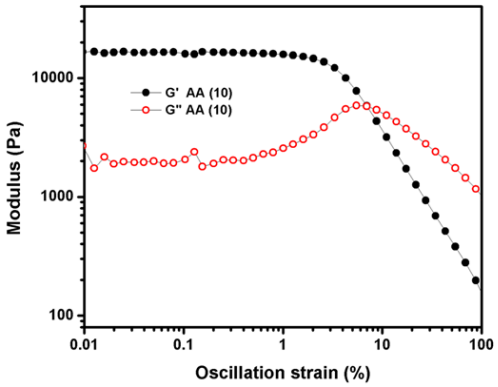
G' AA (10)
G" AA (10)
Modulus (Pa)
Oscillation strain (%)

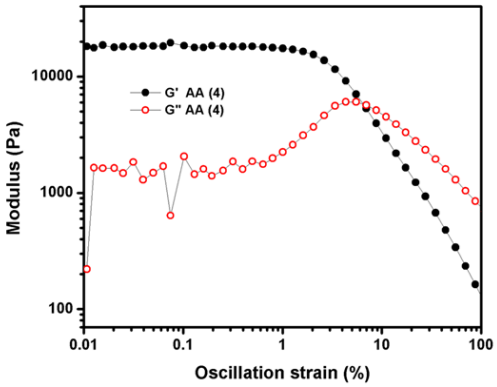
G' AA (4)
G" AA (4)
Modulus (Pa)
Oscillation strain (%)

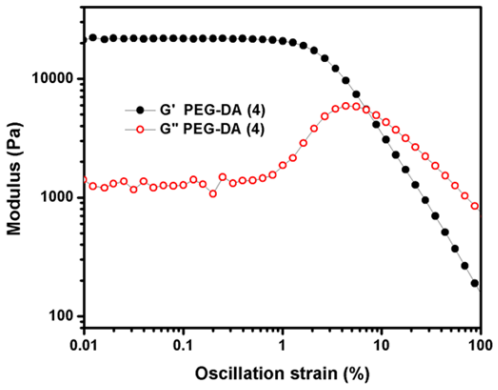
G' PEG-DA (4)
G" PEG-DA (4)
Modulus (Pa)
Oscillation strain (%)

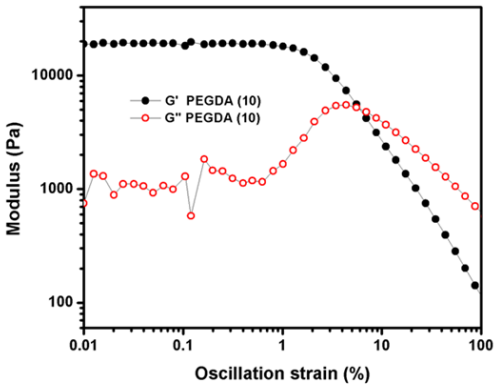
G' PEGDA (10)
G" PEGDA (10)
Modulus (Pa)
Oscillation strain (%)

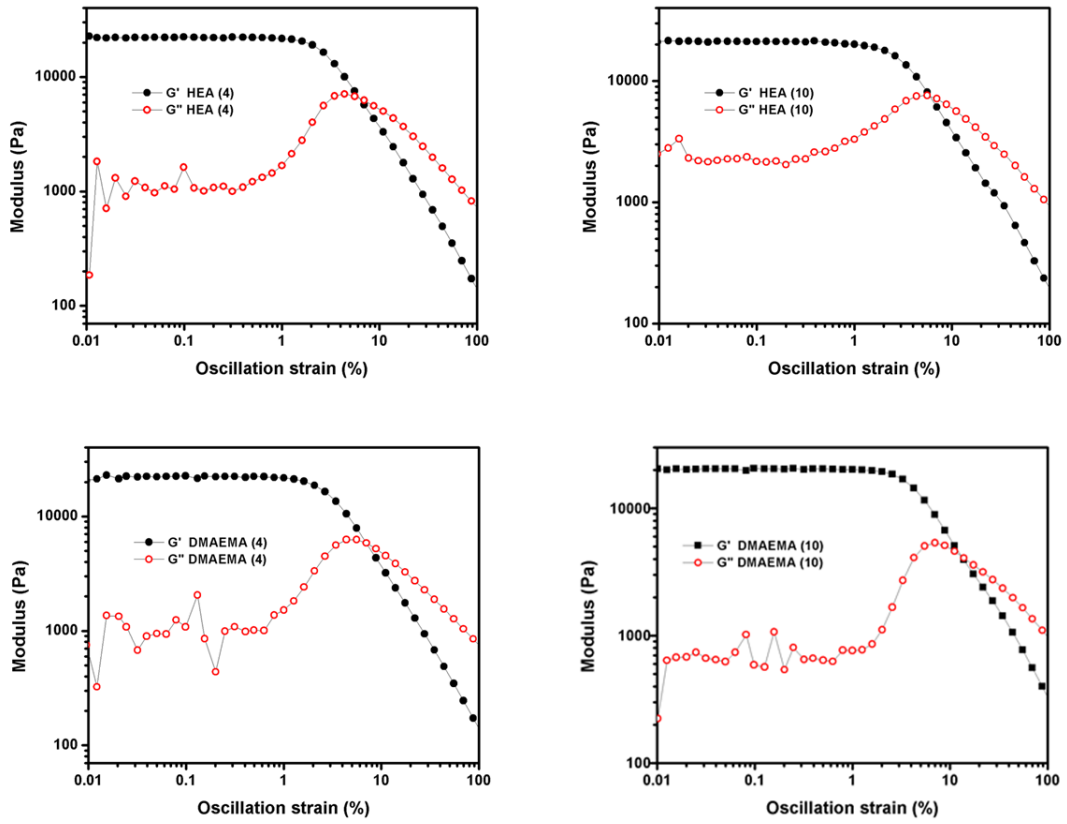

Figure A. 8 Strain sweep experiments from 0-100 % strain performed at 21 ° C and 1.0 Hz.

APPENDIX B

Appendix B accompanies Chapter 3

TNBS Assay

The percent functionalization was calculated using a 2,4,6-trinitrobenzene Sulfonate (TNBS) assay. Primary amines react with TNBS to form a compound that absorbs strongly at 335nm. The setup was as follows, BSA and MA-BSA were each dissolved in CB buffer at a concentration of 20 µg/mL. 0.25 mL of 0.01% (w/v) solution of TNBS was added to 0.5 mL of each protein solution. The samples were incubated at 37 °C for 2 hours. To quench the reaction, 0.25 mL of 10% SDS and 0.125 mL of 1N HCl were added to each sample. The absorbance of each solution was measured at 335nm.

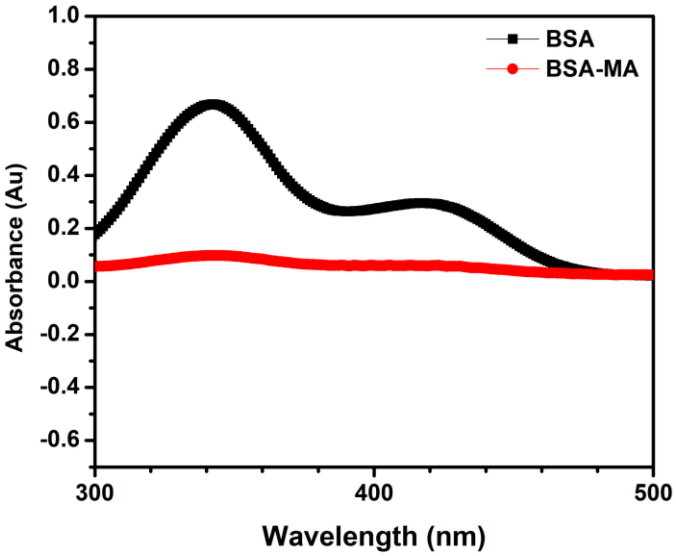

Figure B. 1 UV-vis spectrum of BSA and MA-BSA after incubation with TNBS.

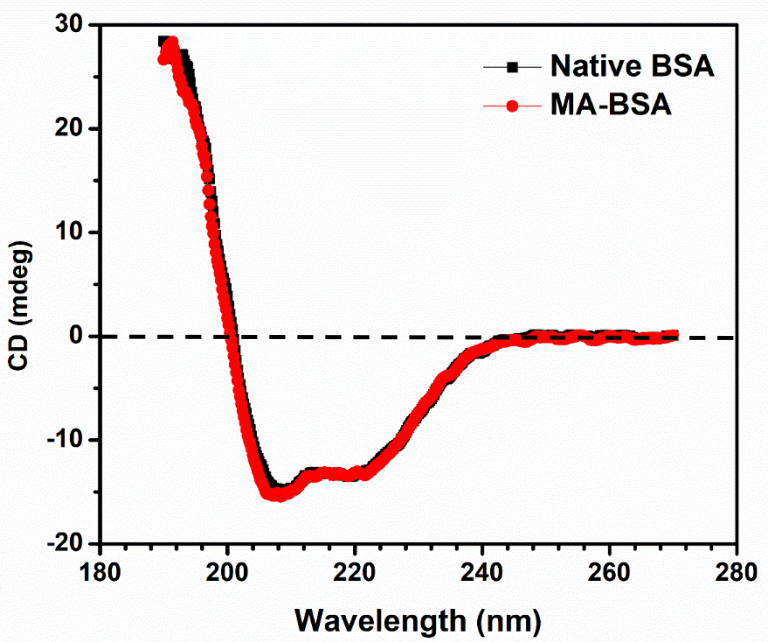

Figure B. 2 CD spectra of native BSA and MA-BSA.

Table B. 1 Secondary structure of native and methacrylated BSA.

Sample	% Helix	% Antiparallel	% Parallel	% Turn	% Others
Native BSA	41.3	17.3	0.0	11.1	30.3
MA-BSA	38.6	16.4	0.0	10.8	34.2

Figure B. 3 Printed compression disk at equilibrium swelling (left) and dehydrated (right). Formulation: 30 wt% MA-BSA with 5 wt% PEG-DA.

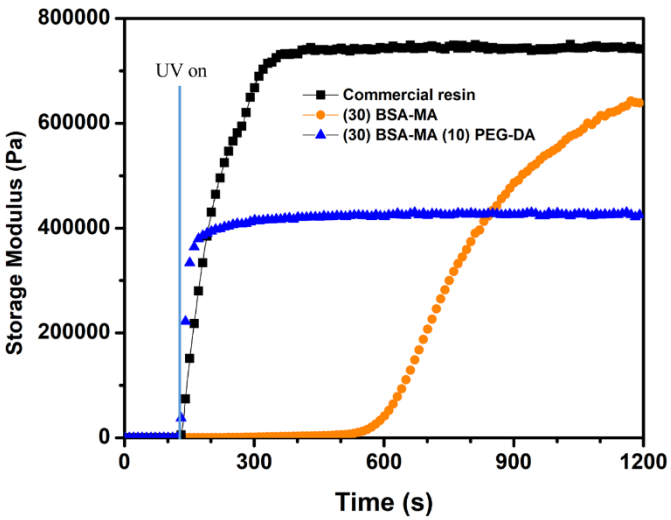

Figure B. 4 Photo-rheology of photo-polymerizable resin formulations.
Commercial resin, 30 wt% MA-BSA, and 30 wt% MA-BSA with 10 wt% PEG-DA. Light source (365 nm) was turned on after 120 s.

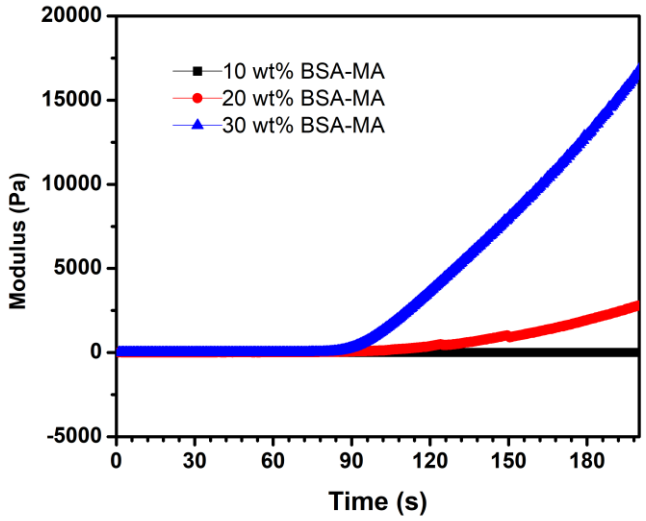

Figure B. 5 Photo-rheology of 10-30 wt% MA-BSA.
Light source (400nm) turned on at 60 s.

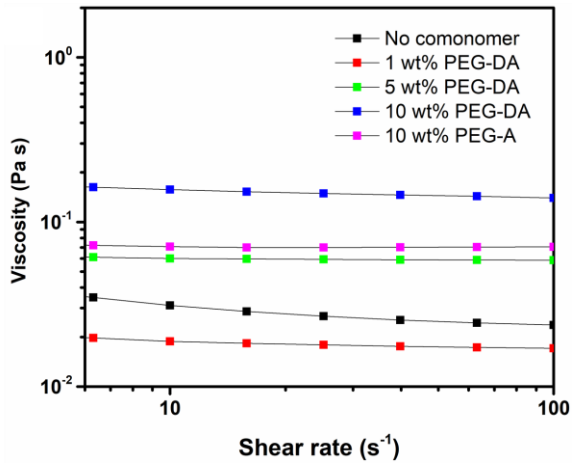

Figure B. 6 Viscosity vs shear rate data for 30 wt% MA-BSA resins with various amounts of comonomer.

Table B. 2 Swelling ratio and % mass loss of various 30 wt% MA-BSA resin formulations, heat-treated and non-heat treated.

Sample	Swelling ratio	% mass loss
5 wt% PEG-DA	3.45	2.8
5 wt% PEG-DA (heat)	2.28	1.2
10 wt% PEG-DA	2.64	3.3
10 wt% PEGDA (heat)	2.21	0.3
10 wt% PEG-A	3.32	9.9
10 wt% PEG-A (heat)	2.64	3.9

Biodegradation

a)

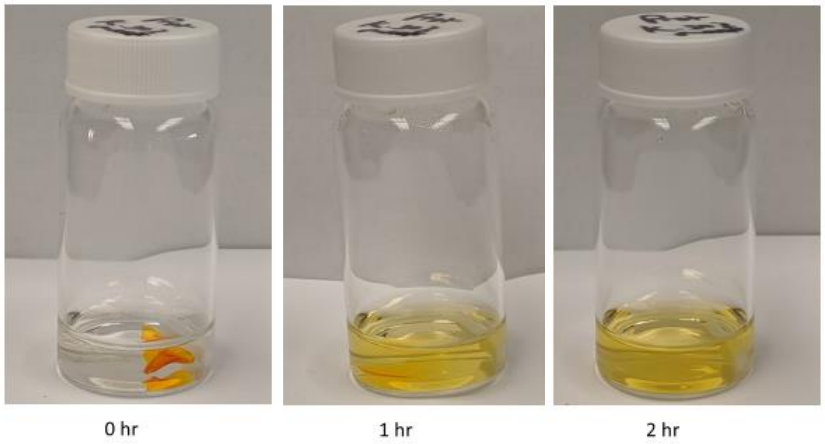

b)

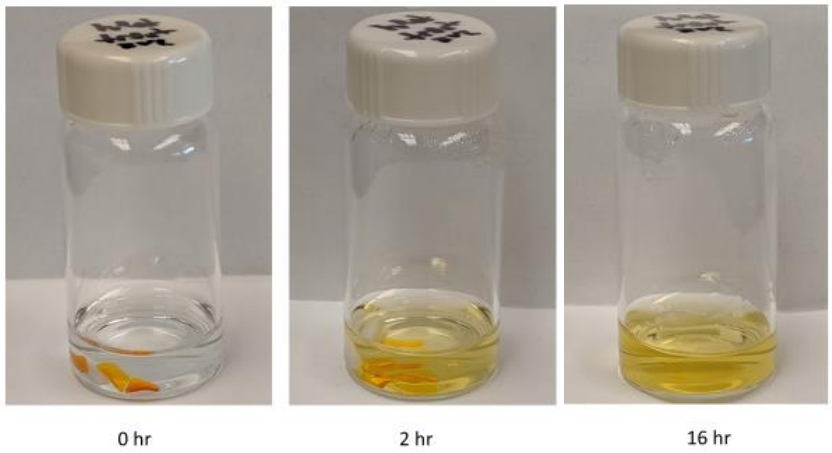

Figure B. 7 (a) 30 wt% MA-BSA and (b) thermal cured 30 wt% MA-BSA digested by proteinase K.

Table B. 3 Change in mass over 1 week of incubation with proteinase K at 37 °C.

Day	Mass Control (g)	% change (control)	Mass Proteinase K (g)	% change (Prot. K)
0	0.2087	-	0.2017	-
1	0.2029	2.8	0.1824	9.6
2	0.2045	2.0	0.1781	11.7
7	0.1993	4.5	0.1573	22.0

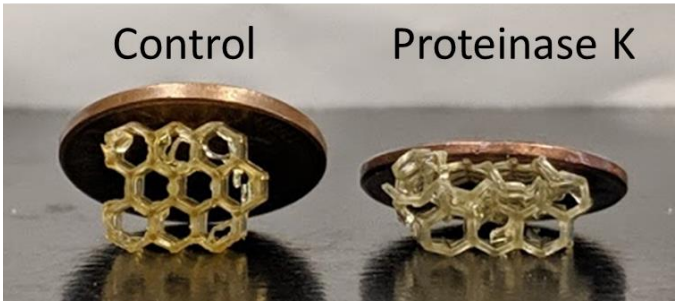

Figure B. 8 Representative image of partially digested hydrogel.
After 1 week of biodegradation, the sample that was incubated with the enzyme (right) is unable to support the weight of a penny, whereas the control (left) was able to support the weight.

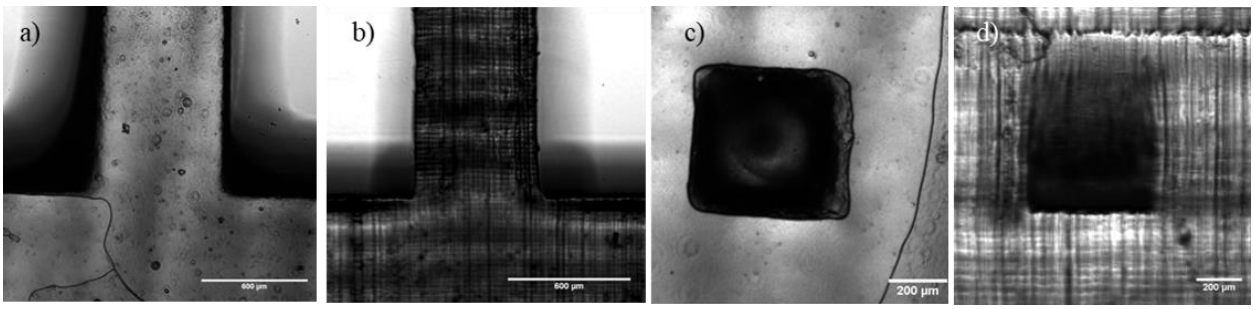

Figure B. 9 Representative optical images of resolution test structures.
Fin (a) and hole (c) printed with the MA-BSA resin. Fin (b) and hole (d) printed with the Form 2 resin.

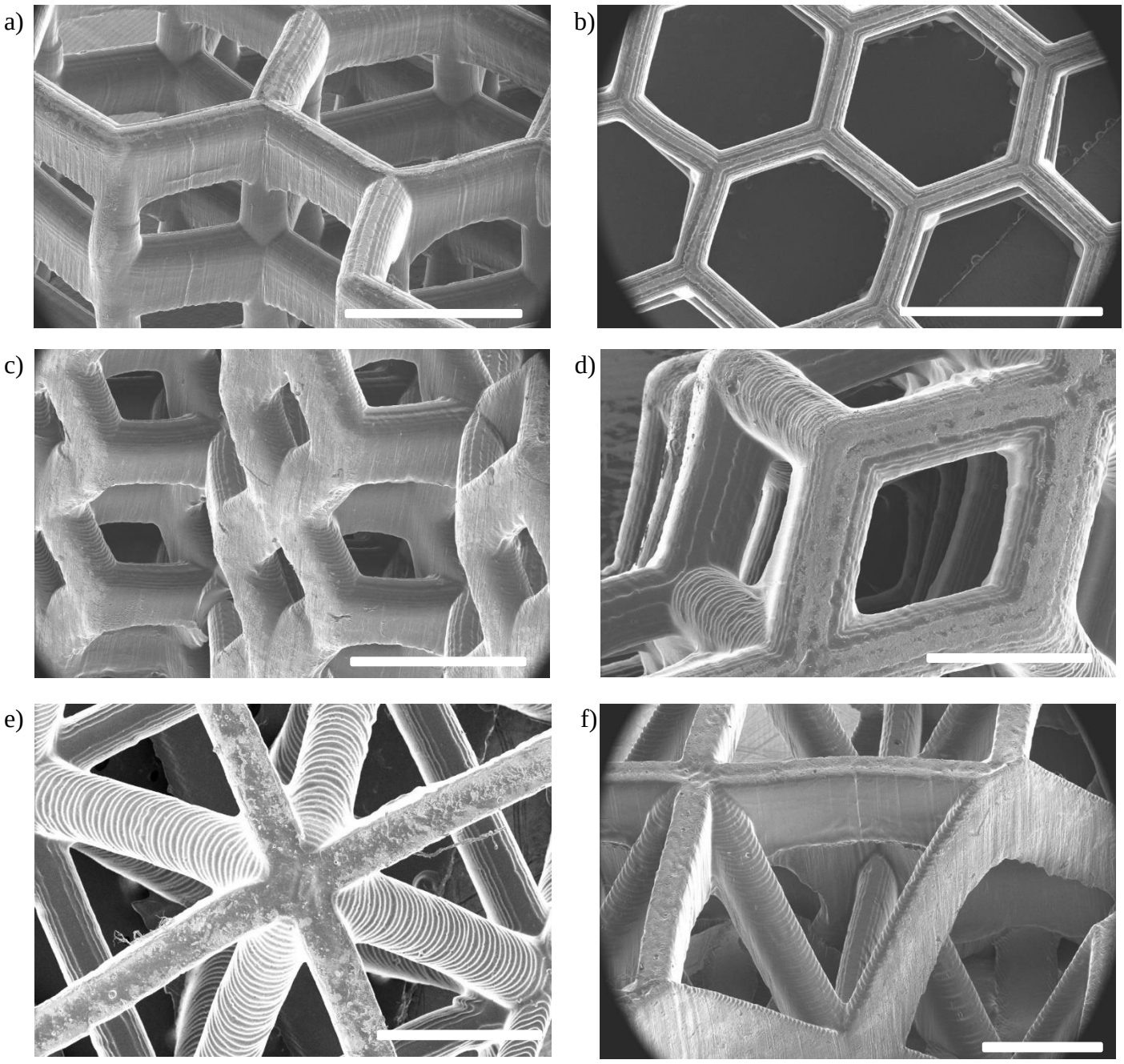

Figure B. 10 SEM images of various lattice structures.

Scale bars: a) 2mm b) 3mm c) 2mm d) 1mm e) 1mm f) 1mm

Table B. 4 Mechanical properties of hydrogel constructs at equilibrium swelling.

Comonomer (wt%)	Thermal cure	Compressive Modulus (MPa)	Compressive Strength (MPa)	ε_{max}	Toughness (MJ/m^3)
PEG-DA (5)	No	2.17	0.68	0.28	0.089
PEG-DA (5)	Yes	2.49	3.49	0.45	0.481
PEG-DA (10)	No	6.26	2.43	0.35	0.391
PEG-DA (10)	Yes	6.06	4.27	0.39	0.596
PEG-A (10)	No	3.27	0.86	0.26	0.106
PEG-A (10)	Yes	3.36	1.75	0.34	0.230

Table B. 5 Mechanical properties of bioplastics printed with various resin formulations.

Comonomer (wt%)	Thermal cure	Compressive Modulus (MPa)	Compressive strength[a] (MPa)	σ_{max} (MPa)	Toughness (MJ/m^3)
PEG-DA (5)	No	284	40	499	79
PEG-DA (5)	Yes	638	120	804	173
PEG-DA (10)	No	296	43	633	101
PEG-DA (10)	Yes	473	97	896	198
PEG-A (10)	No	73	7	203	17
PEG-A (10)	Yes	382	63	635	107

[a] Measured at 20 % deformation.

APPENDIX C

Appendix C accompanies chapter 4.

Table C. 1 Concentration of TA remaining in printed constructs after equilibration in DI water

Formulation	TA concentration (wt%)
2 wt% HEA	25.4
3 wt % AAm	16.6
5 wt% PEG-DA	7.9

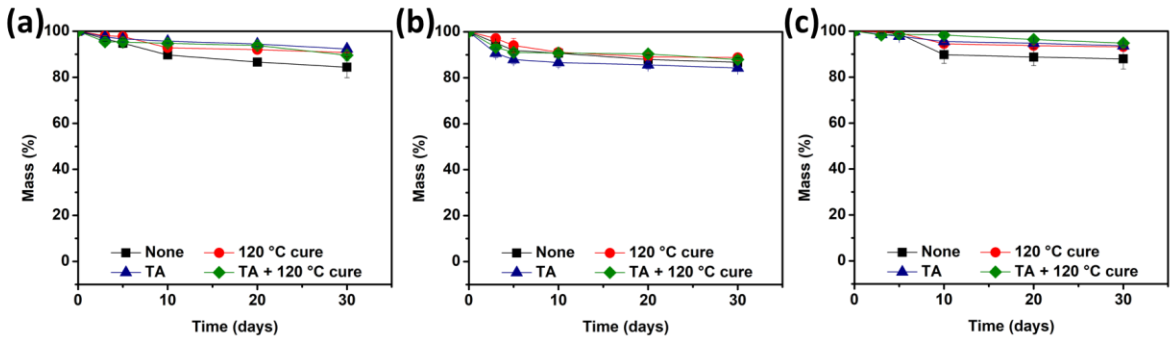

Figure C. 1 Degradation over 30 days in DI water a) HEA, b) AAm, c) PEGDA

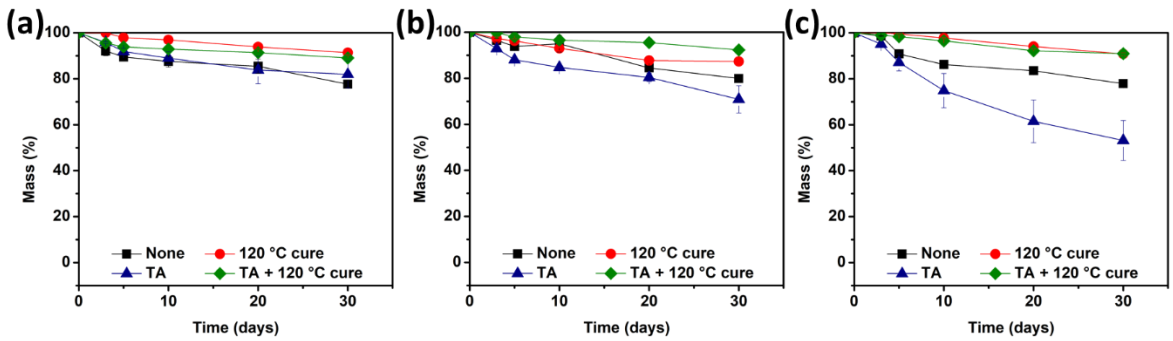

Figure C. 2 Degradation over 30 days in HCl a) HEA, b) AAm, c) PEGDA

Table C. 2 Compression data for MABSA-HEA

Compression	2 wt% HEA			
	E (MPa)	σ (MPa)	ε (mm/mm)	Toughness (MJ/m3)
DI	3.0	0.74	0.28	0.10 ± 0.01
Heat	6.3	6.0	0.49	1.13 ± 0.06
TA	6.6	12.0	0.76	2.07 ± 0.26
TA + heat	48.8	286	0.7	50.20 ± 3.34

Table C. 3 Compression data for MABSA-PEGDA

Compression	5 wt% PEG-DA			
	E (MPa)	σ (MPa)	ε (mm/mm)	Toughness (MJ/m3)
DI	2.2	1.0	0.40	0.16 ± 0.02
Heat	4.5	5.2	0.50	1.14 ± 0.13
TA	4.5	9.7	0.72	1.55 ± 0.26
TA + heat	35.4	173	0.7	31.10 ± 2.50

Table C. 4 Compression data for MABSA-AAm

Compression	3 wt% Aam			
	E (MPa)	σ (MPa)	ε (mm/mm)	Toughness (MJ/m3)
DI	8.1	1.8	0.27	0.23 ± 0.04
Heat	5.5	5.3	0.45	1.04 ± 0.05
TA	5.1	15.4	0.65	3.25 ± 0.14
TA + heat	30.2	215	0.7	39.27 ± 2.09

Table C. 5 Effect of TA concentration on TA incorporation into hydrogel

TA concentration	No heat 24 hours	No heat 72 hours	TA (24 hr) Heat TA
0 mg/mL	2.37	2.32	0.81
50 mg/mL	1.84	1.58	0.45
100 mg/mL	1.30	0.90	0.42
150 mg/mL	1.21	0.73	0.33
200 mg/mL	0.98	0.61	0.33
250 mg/mL	0.93	0.58	0.26
300 mg/mL	0.92	0.58	0.17

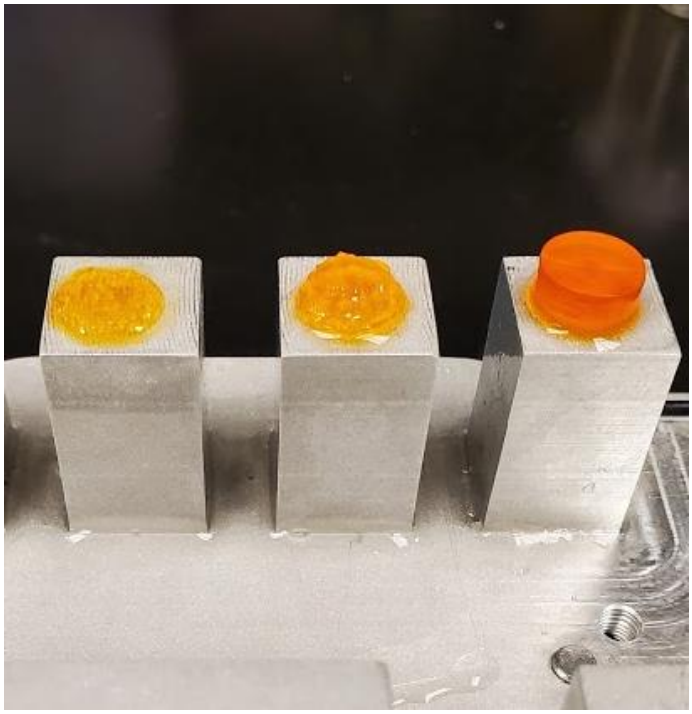

Figure C. 3 Representative image of printability of tested resin formulations. 1 wt% AAm, 2 wt% AAm, and 3 wt% AAm (left to right)

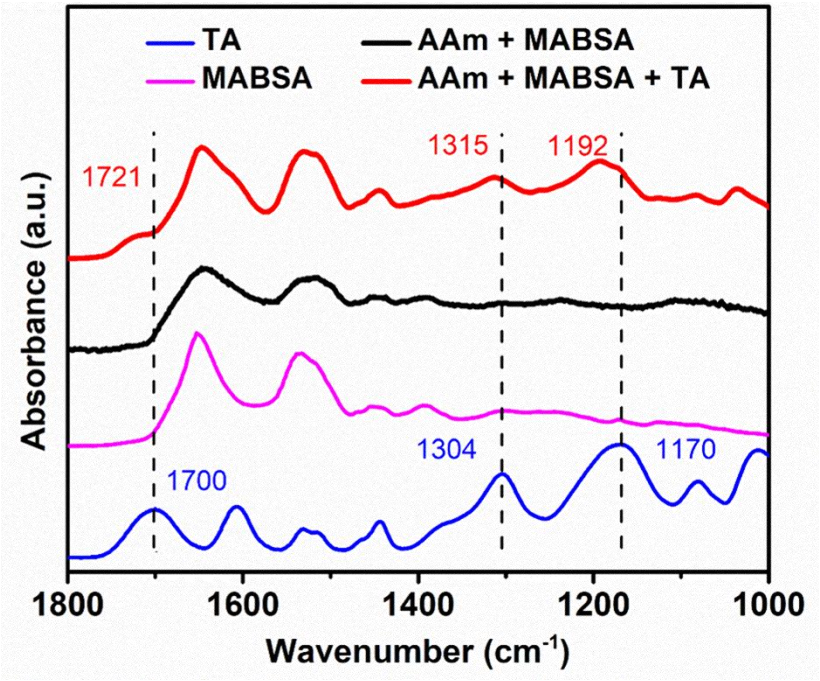

Figure C. 4 ATR-FTIR spectra of TA, MABSA, MABSA-AAm, and MABSA-AAm-TA

Table C. 6 Tensile data for MABSA-HEA

Tensile	**2 wt% HEA**			
	E (MPa)	**σ (MPa)**	**ε (mm/mm)**	**Toughness (kJ/m3)**
None	0.64	0.242	0.61	89.66
TA	17.26	1.38	0.94	1120.80
TA + heat	118.0	7.115	0.54	3461.5

Table C. 7 Tensile data for MABSA-PEGDA

Tensile	**5 wt% PEG-DA**			
	E (MPa)	**σ (MPa)**	**ε (mm/mm)**	**Toughness (kJ/m3)**
None	0.68	0.178	0.39	39.18
TA	10.5	0.948	0.75	608.61
TA + heat	58.7	3.84	0.43	1354.6

Table C. 8 Tensile data for MABSA-AAm

Tensile	**3 wt% AAm**			
	E (MPa)	**σ (MPa)**	**ε (mm/mm)**	**Toughness (kJ/m3)**
None	2.02	0.498	0.33	93.32
TA	6.81	0.909	0.67	464.16
TA + heat	37.4	3.169	0.81	1940.3

Table C. 9 Photorheology of MABSA resin formulations

Formulation	Gel point (s)	G' @ 30 s (kPa)
1 wt% HEA	9.7	73.4
2 wt% HEA	7.6	273.1
2 wt% AAm	6.5	513.5
3 wt% AAm	5.8	420.1
4 wt% PEGDA	11.8	113.2
5 wt% PEGDA	9.5	132.8

Table C. 10 (Data from "Additive manufacturing of bovine serum albumin-based hydrogels and bioplastics")

Day	% mass loss (control)	% mass loss (Proteinase K)
0	-	-
1	2.8	9.6
2	2.0	11.7
7	4.5	22.0

VITA

Education

2021	PhD in Chemistry – University of Washington
	Graduate Research Advisor – Alshakim Nelson
2016	BS with Honors in Chemistry – College of William and Mary
	Undergraduate Research Advisor – David Kranbuehl

Publications

1. **Smith P**, Altin G, Narupai B, Milllik S, Park J, Nelson A, "Additive Manufacturing of Tough, Bovine Serum Albumin-based Hydrogels and Bioplastics" (manuscript in preparation)
2. Sanchez-Rexach E, **Smith P**, Gomez-Lopez A, Fernandez M, Cortajarena A, Sardon H, Nelson A, "3D Printed Bioplastics with Shape-Memory Behavior Based on Native Bovine Serum Albumin" (Accepted: ACS Applied Materials and Interfaces)
3. Narupai B, **Smith P**, Nelson A. "4D Printing of Multi-stimuli Responsive Protein-Based Hydrogels for Shape Transformations (Accepted: Advanced Functional Materials)
4. Johnston, T; Yuan, S; Wagner, J; Yi, X; Saha, A; **Smith, P**; Nelson, A; Alper, H. "Compartmentalized Microbes and Co-cultures in Hydrogels for On-demand Bioproduction and Preservation" *Nat Commun* **2020** *11*, 563
5. **Smith, P**; Narupai, B; Tsui, J; Millik, S; Shafranek, R; Kim, D; Nelson, A. "Additive Manufacturing of Bovine Serum Albumin-Based Hydrogels and Bioplastics" *Biomacromolecules* **2020**, *21*, 484-492
6. Millik, S; Dostie, A; Karis, D; **Smith, P**; McKenna, M; Chan, N; Curtis, C; Nance, E; Theberge, A; Nelson, A. "3D Printed Coaxial Nozzles for the Extrusion of hydrogel Tubes Toward Modeling Vascular Endothelium" *Biofabrication* **2019**, *11*, 045009

7. Shafranek, R; Millik, S; **Smith, P**; Lee, C; Boydston, A; Nelson, A. “Stimuli-responsive Materials in Additive Manufacturing” *Prog. Polym. Sci.* **2019**, *93*, 36-67
8. **Smith, P**; Basu, A; Saha, A; Nelson, A. “Chemical Modification and Printability of Shear-thinning Hydrogel Inks for Direct-write 3D Printing” *Polym.* **2018,** *152*, 42-50
9. Hocker, S; Hudson-Smith, N; **Smith, P**; Komatsu, C; Dickinson, L; Schniepp, H; Kranbuehl, D. “Graphene Oxide Reduces the Hydrolytic Degradation in Polyamide-11” *Polym.* **2017**, *126*, 248-258